INAUGURAL – DISSERTATION

zur
Erlangung der Doktorwürde
der
Naturwissenschaftlich-Mathematischen Gesamtfakultät
der
Ruprecht – Karls – Universität
Heidelberg

vorgelegt von
Juliane Claus
(Dipl. Mathematikerin & M.Sc. Molekulare Biotechnologie)
aus *Halle*

Tag der mündlichen Prüfung:
...

Thema

Modeling of zinc uptake and transport in plant roots

Betreuer:

Herr Dr. Andrés Chavarría Krauser (Universität Heidelberg)

Modeling of zinc uptake and transport in plant roots

Summary

Zinc is an essential micronutrient in green plants, yet toxic at high concentrations. Only specialized hyperaccumulator plants can tolerate high zinc doses and are therefore of special interest for their potential application in phytoremediation and crop development. Zinc ions are taken up from the soil along with water and are transported towards the root's vascular bundle in two parallel ways: cell wall (apoplast) and cytoplasm (symplast). Cross-membrane transport into and out of the cytoplasm is mediated by ZIP and HMA transporter proteins, respectively. The ZIP transporters responsible for zinc uptake are highly regulated to guarantee an optimal internal zinc concentration under varying external conditions.

A dynamical model based on ordinary differential equations is used to study the regulation of ZIP transporters. A data-based model in yeast allows insights into general mechanisms. Simulations of different model variants in plants suggest an activator-inhibitor model as the most likely mechanism, because it provides more robust zinc homeostasis than simpler models without inhibitor. High robustness of the steady state towards external zinc variations, however, leads to instability of the steady state and high-amplitude oscillations. These oscillations form stable periodic solutions and emerge from a supercritical Hopf bifurcation in certain critical values of the external zinc concentration.

To study spatial aspects of the zinc distribution in root tissues, the ZIP regulatory model was coupled to a radial transport model. This model accounts for the structure of the root consisting of symplast and apoplast and includes effects of water flow, diffusion, and cross-membrane transport via transporters. It also incorporates the radial geometry and varying porosity of root tissues. We use existing biological data to estimate parameters and analyze the properties of the model in numerical simulations. Experimental results show a pattern of zinc accumulation close to the center of the root, which disappears at high levels of the efflux transporter HMA. Using our model, we study the roles of ZIP regulation, HMA level and water flow velocity in the creation of this radial pattern. In the steady state, the model reproduces the zinc gradient found in experiments as well as its loss at increased levels of HMA. Surprisingly, water flow velocity is found to be also a key parameter for producing this gradient. These results give insight into the uptake and transport of zinc in roots and suggest improved experimental assays.

Buffering and vacuolar sequestration are known to play important roles in zinc homeostasis. Regulated vacuolar sequestration in yeast again serves as a data-based model for possible mechanisms. In plants, buffering can dampen the oscillations and lead to stability of the steady state. Since experiments do not suggest oscillatory behavior in the cellular zinc concentration, these results indicate the existence of strong zinc buffers.

Modellierung von Zinkaufnahme und Transport in Pflanzenwurzeln

Zusammenfassung

Zink ist ein essentielles Spurenelement für Pflanzen, in hohen Konzentrationen jedoch giftig. Nur spezialisierte sogenannte Hyperakkumulatoren können hohe Zinkmengen tolerieren und werden aufgrund von mögliche Anwendungen in der Phytoremediation oder als funktionelle Nahrungsmittel seit Längerem erforscht. Zinkionen werden in Wasser gelöst aus dem Boden aufgenommen und auf zwei Wege durch die Wurzel zum Leitgewebe transportiert: der Zellwand (Apoplast) und dem Zytoplasma (Symplast). Die Transportproteine ZIP und HMA erlauben den Zinktransport über Zellmembranen. Die für die Aufnahme zuständigen ZIP Transporter sind hoch reguliert, um eine optimale zelluläre Zinkkonzentration unter schwankenden externen Bedingungen zu garantieren.

Ein dynamisches Modell aus gewöhnlichen Differentialgleichungen wird zur Untersuchung der Regulation der ZIP-Transporter verwendet. Das Modell wird in Hefe und Pflanzenwurzeln angewendet. Simulationen verschiedener Modellvarianten deuten darauf hin, dass in Pflanzen ein Aktivator-Inhibitor-Mechanismus wahrscheinlicher ist als einfachere Modelle ohne Inhibitor, denn dieser Mechanismus erlaubt robustere Zinkhomöostase. Hohe Robustheit der stationären Lösung führt jedoch zur Instabilität und der Entstehung von Oszillationen. Diese bilden stabile periodische Lösungen und entwickeln sich aus einer superkritischen Hopfbifurkation in bestimmten kritischen Werten der externen Zinkkonzentration.

Um räumliche Zinkdistributionen im Wurzelgewebe zu verstehen, wurde das ZIP-Regulationsmodell gekoppelt mit einem radialen Transportmodell. Dieses berücksichtigt die Struktur der Wurzel mit Symplast und Apoplast, die radiale Geometrie und wechselnde Porosität und beschreibt die Effekte von Wasserfluss, Diffusion und Membrantransport durch Transportproteine. Biologische Daten werden zur Abschätzung der Parameter verwendet. Experimentelle Ergebnisse zeigen ein Muster mit hoher Zinkakkumulation im Zentrum der Wurzel, welches bei Erhöhung des Effluxtransporters HMA verschwindet. Diese stationären Zustände werden im Modell reproduziert. Erstaunlicherweise scheint der Wasserfluss jedoch auch eine Schlüsselrolle bei der Erzeugung dieses Gradienten zu spielen. Diese Resultate geben Biologen wichtige Erkenntnisse und Vorschläge für verbesserte experimentelle Messungen.

Pufferung und Sequestrierung spielen eine wichtige Rolle in der Zinkhomöostase. Die regulierte Sequestrierung in die Vakuole in Hefe lässt sich mithilfe von Daten gut simulieren und experimentelle Vermutungen bestätigen. In Pflanzenmodell führt simulierte Pufferung zu einer Dämpfung der beobachteten Oszillationen und zur Stabilisierung des Steady States. Da Experimente tatsächlich keine Anzeichen von Oszillationen in der Zinkkonzentration liefern, deuten diese Ergebnisse auf eine starke Pufferung hin.

Acknowledgements

I would like to express my gratitude to Andrés Chavarría Krauser for giving me the opportunity to write this thesis and for the excellent supervision, his ideas, his motivation and his ongoing support and advice. Being the first doctoral student can be blessing or curse–in this case it was a blessing. I hope that many more students will have the chance to benefit from his extraordinary wisdom and enthusiasm.

Moreover, I would like to thank Ansgar Bohmann for his readiness to help in any situation, for the constant support in technical issues and his broad knowlegde often leading to new perspectives and directions of study. I am also thankful to Mariya Ptashnyk for the great time in Dundee and for lots of help and discussions on mathematical aspects.

Last but not least, I thank my family and friends for their sympathy and encouragement, and Jens for always being there.

Contents

List of Figures

Abbreviations

bZIP	basic-region leucine zipper
CDF	cation diffusion facilitator
co	cortex
en	endodermis
ep	epidermis
HMA	heavy metal ATPase
IRT	iron-regulated transporter
MTP	metal tolerance protein
ODE	ordinary differential equation
OPT	oligopeptide transporter
pc	pericycle
PDE	partial differential equation
YSL	yellow-stripe-like
ZAP	zinc-dependent activator protein
ZDRE	zinc deficiency response element
ZIP	ZRT-, IRT-like protein
ZRE	zinc responsive element
ZRT	zinc-regulated transporter

1 Introduction

Zinc is an essential micronutrient in green plants, yet toxic at high concentrations. Only specialized hyperaccumulator plants can tolerate high zinc doses and are therefore of special interest for their potential application in phytoremediation and crop development (Clemens et al., 2002). For this reason, zinc transporters and the mechanisms of its uptake in plants have been studied extensively by experimentalists. To our knowledge, no approaches have been undertaken so far to understand zinc uptake from a modeling point of view.

Besides the importance of zinc by itself, the study of its uptake regulation and transport mechanisms provides useful insights into the general functionality of plant nutrient uptake. In this sense, the models presented here stand as examples for ion uptake in plant roots and can easily be adapted for other nutrients.

Project Description and Objectives

The aim of this interdisciplinary thesis is the development of mathematical models of zinc uptake and transport in plant roots, their analysis and numerical simulation, and the discussion of biological relevance and implications.

The first chapters of this work give an introduction to the biological and mathematical background of the models developed later on. Chapter 2 summarizes the current biological knowledge on zinc nutrition and transport in roots, while Chapter 3 introduces the types of differential equations to be used and gives an overview of the relevant mathematical theorems.

A model for the regulation of zinc uptake transporters of the ZIP family is presented in Chapter 4. This homeostasis model based on ordinary differential equations (ODEs) is developed in a general setting and fitted to experimental data from yeast and plants. Three different model alternatives for plant roots are analyzed for their ability to provide robust and stable zinc homeostasis. The results of this chapter were developed with A. Chavarría Krauser and were published in Claus and Chavarría-Krauser (2012).

In the model identified as the most feasible in Chapter 4 a Hopf bifurcation occurs for certain parameter choices. This Hopf bifurcation is analyzed for stability and global continuation in Chapter 5. The results of this chapter were developed with M. Ptashnyk, A. Bohmann and A. Chavarría Krauser and were published in Claus et al. (2014).

In Chapter 6 the ODE model for the regulation of ZIP transporters is coupled to a spatial transport model based on partial differential equations (PDEs). The model accounts for the internal structure of the root, its radial geometry and varying porosity. Numerical simulations are used to explain the unequal zinc distribution in root tissues found in experiments and to identify key processes leading to this pattern. These results were developed with A. Bohmann and A. Chavarría Krauser and were published in Claus et al. (2013) and Claus and Chavarría-Krauser (2013).

Chapter 7 focuses on the role of buffering and sequestration in zinc homeostasis. A model for vacuolar zinc sequestration in yeast serves as a well-studied example and can be used to discuss the role of “pro-active” expression. Buffering in plant roots is modeled in a simple setting and analyzed for its function in damping oscillations. These latter results were developed with A. Bohmann and A. Chavarría Krauser and were published in Claus and Chavarría-Krauser (2013) and Claus et al. (2014).

2 Biological background

2.1 Plant zinc nutrition

Zinc is a heavy metal and micronutrient that plays an important role in all living organisms and is essential for humans (Maret, 2013) as well as for higher green plants (Sommer and Lipman, 1926). It is part of the functional subunits or cofactor of more than 300 proteins, among them the class of zinc-finger-proteins that are essential as interaction modules between DNA, RNA, proteins and other molecules. In addition, it has been reported to protect plant cells from oxidative stress mediated by reactive oxygen species (Cakmak, 2000) and may act as an intracellular second messenger (Yamasaki et al., 2007).

In spite of its indispensability, zinc becomes toxic in higher doses. Toxicity is far less frequent than deficiency, but likely in plants growing on contaminated soils, e.g. in mining or industrial areas. Most plants react to elevated zinc levels with toxicity syndromes, such as reduced growth and leaf chlorosis (Broadley et al., 2007). Zinc toxicity has also been reported to lead to abnormal depositions in the xylem vessel walls (Robb et al., 1980). Only specialized zinc-hyperaccumulating species are able to tolerate high levels without impairment (Zhao et al., 2000). In order to do so, they possess mechanisms for both the increased uptake of zinc from the soil and its sequestration and detoxification (Macnair et al., 1999). These mechanisms are subject of ongoing research, as they implicate interesting applications in phytoremediation or nutritional enhancement (Chaney et al., 1997).

Avoiding both deficiency and toxicity, plants need to take up their required amounts of zinc. Unlike animals they cannot adapt their nutrition accordingly, but depend on the zinc content of the soil. This content may vary considerably in different locations and under different conditions. How are plants able to adapt to this variety?

2.1.1 Zinc transporters

Charged zinc ions are unable to cross cell membranes freely (Alberts et al., 2002). Instead, they are transported across membrane barriers by specialized

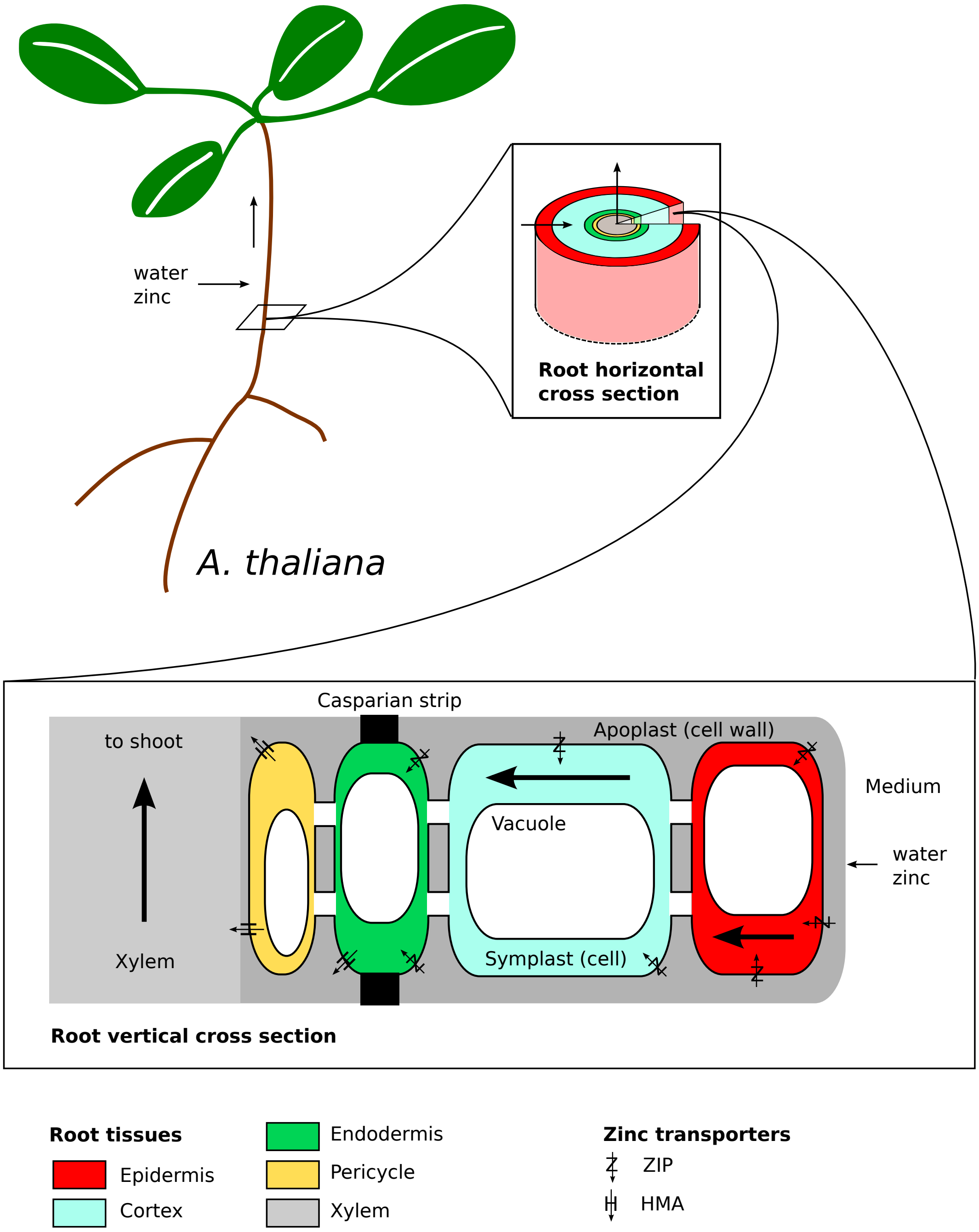

Figure 2.1: Schematical overview of zinc uptake in *A. thaliana*. Each root tissue (epidermis, cortex, endodermis, pericycle) consists of one layer of cells. Water and zinc move from the outer medium towards the central cylinder, where they are taken up into the xylem and go towards the shoot. Zinc transporters ZIP and HMA transport zinc across cell membranes into and out of the cytoplasm, respectively. ZIP is located in epidermis, cortex and endodermis outside the Casparian strip, while HMA is located in endodermis and pericycle inside the Casparian strip.

transporter proteins (Clemens et al., 2002). There are different transporters involved in the transport of zinc in plants. The most well-known families are: ZIP (ZRT-, IRT-like proteins), HMA (heavy metal ATPases), and MTP (metal tolerance protein) or CDF (cation diffusion facilitator). Members of the ZIP family are believed to act as influx carriers, including uptake from the soil (similar to ZRTs in yeast). HMAs accomplish efflux of zinc, e.g. from roots into xylem vessels, while MTPs are involved in sequestration from the cytoplasm into cell compartments, such as the vacuole (Palmer and Guerinot, 2009). Other results suggest the involvement of YSL (yellow-stripe-like) transporters and OPT (oligopeptide transporters) in zinc homeostasis and transport of chelated metal ions (DiDonato et al., 2004; Schaaf et al., 2005).

To provide sufficient zinc uptake without reaching toxicity, the uptake transporters are tightly regulated. In general, this regulatory mechanism has to consist of two parts: sensing of the intracellular zinc concentration and reaction to changes by controlling the amounts of zinc transporters. Sensing of changes in zinc concentrations must be very sensitive, because the actual available zinc concentration within cells is believed to be very small. Zinc ions bind to various intracellular proteins, are chelated and sequestered into specific cellular compartments, such as the vacuole (Clemens, 2001). Therefore, although the total zinc content of cells may be in a millimolar range, the actual concentration of free zinc ions in the cytoplasm is estimated to be much lower. Earlier investigations suggest concentrations in a femtomolar range (Outten and O'Halloran, 2001), while more recent results indicate nanomolar ranges (Vinkenborg et al., 2009; Dittmer et al., 2009). Zinc influx carriers are thought to be regulated by this pool of free zinc ions plus ions that are loosely bound to chelator proteins and are available to bind to other proteins with higher affinity.

From experiments, the main influx transporters of the ZIP family appear to be ZIP1 to ZIP4, ZIP9, and IRT3 (iron-responsive transporter) (Grotz et al., 1998). These transporters are highly expressed under conditions of zinc deficiency, but their expression decreases quickly when zinc is added to the media (Talke et al., 2006). The exact mechanism of this regulation is still unknown. Recent results have shown that at least *ZIP4* in *Arabidopsis thaliana* is regulated by transcription factors of the basic-region leucine zipper (bZIP) family: bZIP19 and bZIP23 (Assunção et al., 2010a). These factors bind to a ZDRE (zinc deficiency response element), which has been found not only in the upstream region of *ZIP4*, but also of *ZIP1*, *ZIP3*, *ZIP9* and *IRT3*. Therefore it is reasonable to assume similar regulation for these ZIP transporters.

Unlike the ZAP1 transcription factor in yeast (see Section 2.2), bZIP19 and bZIP23 transcription factors do not have a zinc binding site (Assunção et al., 2010a). It is unclear how they sense the intracellular zinc status. Existence of further players that bind zinc and act as inhibitors of bZIP19 and bZIP23 have been proposed (Assunção et al., 2010b). Transcription factors of the bZIP family have been studied in other regulatory networks and are known to be regulated post-transcriptionally in various ways (Schütze et al., 2008). Generally, bZIP transcription factors (in particular bZIP19 and bZIP23) are known to dimerize (Jakoby et al., 2002). They are partially redundant (Assunção et al., 2010a) and it is believed that they preferentially form homodimers, but may also constitute heterodimers (Deppmann et al., 2006).

The efflux of zinc from the root to the shoot mainly depends on HMA2 and HMA4 transporters, which are predominantly expressed in the pericycle cells adjacent to the xylem (Sinclair et al., 2007; Hanikenne et al., 2008). Zinc hyperaccumulator species such as Arabidopsis halleri appear to have the same ZIP transporters as nonhyperaccumulators, but different *HMA4* genes. Moreover, studies in different plant species have shown that hyperaccumulators possess multiple copies of *HMA4* in their genome. This results in higher expression levels and more efficient root-to-shoot transport of zinc (Hanikenne et al., 2008; Ó Lochlainn et al., 2011).

2.1.2 Transport across the root

Water and zinc are taken up from the soil by the epidermal root cells that often possess root hairs to increase their surface towards the soil or medium. From the epidermis the substances are transported radially towards the xylem, from where they are distributed to stem and leaves (Clemens et al., 2002). On this way, they pass through several tissues: the epidermis, the cortex, the endodermis, and the pericycle (Hanikenne et al., 2008, Fig. 1). In *Arabidopsis thaliana*, each of these tissues comprises only one layer of cells (Dolan et al., 1993). The cytoplasm of adjacent cells is connected by plasmodesmata, which may be simple channels or have complex geometries (Roberts and Oparka, 2003) and forms a symplastic continuum without membrane barriers.

Besides through the symplast, water and ions are also free to move in the cell wall continuum, the apoplast, which has been found to contribute significantly to root transport processes (Steudle, 1994). The apoplastic flow, however, is interrupted in the endodermis by suberin deposited in the cell wall (Casparian strip). This strip is mostly impermeable to water and ions, although some findings suggest there may also be flow across this barrier (White et al., 2002; Ranathunge et al., 2005). Nevertheless, most water and ions need to pass the cell membrane and enter the symplast before the Casparian strip to be transported further (Yang and Jie, 2005). Because membrane transport is much more selective than apoplastic flow, this barrier is believed to function as a mechanism to control the uptake of nutrients and solutes. While considerable amounts of water can cross the membrane freely, ions are almost completely blocked and their transport across cell membranes relies on the specialized transporter proteins described above. A schematical overview of zinc transport across roots is given in Fig. 2.1.

2.2 Zinc in yeast

The yeast *Saccharomyces cerevisiae* has been widely used as a model organism for various processes. As yeast is a single-cellular organism, experimental measurements are much easier and less prone to artifacts. Especially for zinc uptake, yeast is an interesting model organism, as the membrane transporters belong to the same protein family and are potentially regulated in a similar manner as in plants.

The regulation of zinc uptake in yeast cells has been studied in much detail and found to be a combination of two systems with high and low affinity for zinc ions. A similar distribution of high and low affinity transporters has also been found in wheat (Hacisalihoglu et al., 2001) and is thought to exist in other plants as well (Guerinot, 2000). A schematic overview of the system can be seen in Fig. 2.2. Zinc ions are transported with high affinity by ZRT1 (zinc-responsive transporter) and with low affinity by ZRT2, which both belong to the ZIP (zinc-, iron-permease) family. ZRT1 has been found to be strongly regulated by the intracellular zinc concentration and almost exclusively active under conditions of zinc deficiency (Zhao and Eide, 1996a). ZRT2 has been reported to guarantee a basic zinc uptake level under normal zinc-replete conditions (Zhao and Eide, 1996b) while being repressed under zinc deficiency (Bird et al., 2004).

Further studies have shown that both *ZRT1* and *ZRT2* are activated by the transcription factor ZAP1 (zinc-dependent activator protein) (Zhao et al., 1998), which binds to so-called zinc responsive elements (ZREs) in the promoter regions of the respective genes. Under conditions of elevated zinc concentrations, the activity of ZAP1 is reduced and production of ZRT1 and ZRT2 decreases. Inactivation of ZAP1 occurs most likely by direct binding of free zinc ions, although further signaling molecules may also be involved in this process. By binding to its own promoter region, ZAP1 regulates its transcription introducing a positive feedback mechanism and presumably allowing an even stronger response to zinc-limiting conditions (Eide, 2003). In addition to the transcriptional regulation, ZRT1 is also regulated by a post-translational mechanism (Eide, 2003). While it is a stable membrane protein under zinc deficient conditions, ZRT1 is ubiquinated and subjected to endocytosis for high intracellular zinc levels. The details of this mechanism have been investigated

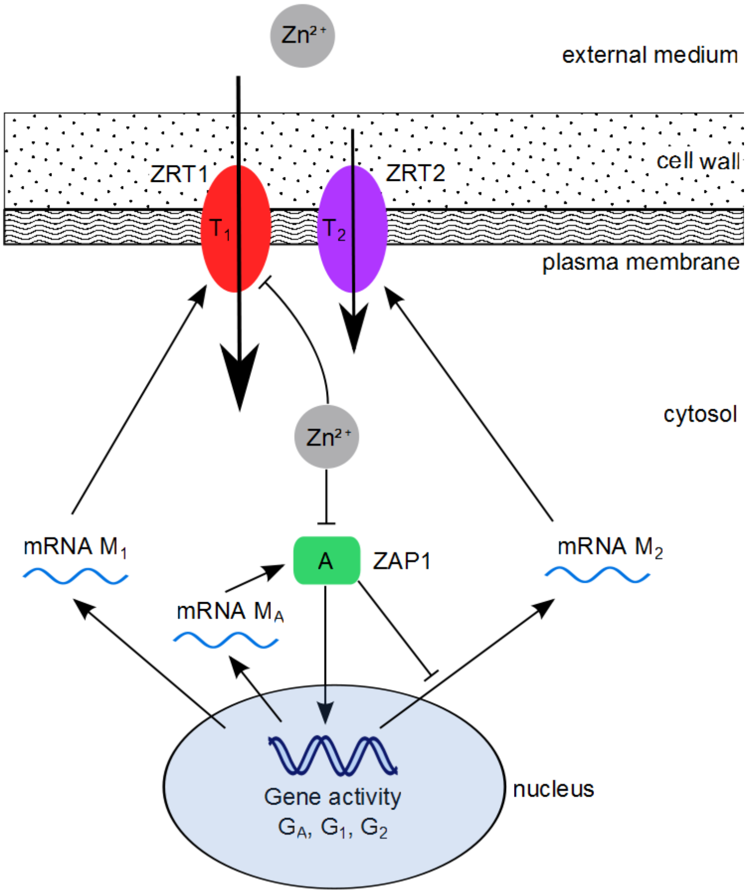

Figure 2.2: Yeast: scheme of zinc influx regulation model. The activator ZAP1 (A) is inactivated by zinc. It induces gene activity for its own gene, *ZRT1* and *ZRT2* (G_A, G_1, and G_2) and also inhibits transcription of *ZRT2*. Gene activity results in transcription of mRNAs (M_A, M_1, M_2) that are translated into the proteins ZAP1 and the transporters ZRT1 (T_1) and ZRT2 (T_2), respectively. ZRT1 is also post-translationally inhibited by zinc.

in Gitan et al. (2003), but it is yet unknown whether zinc ions bind directly to ZRT1 to induce its ubiquitination, or whether other zinc-binding proteins are involved. It has been proposed that the combination of transcriptional and post-translational regulation allows for a very quick response to changing environmental conditions and thus prevents a toxic zinc shock (Eide, 2003).

3 Mathematical background

3.1 Modeling with ordinary differential equations

Ordinary differential equations (ODE) are commonly used to model chemical reaction kinetics. For an elementary reaction of two reactants A and B to a product C, in chemical notation

$$A + B \xrightarrow{k} C \ ,$$

according to the law of mass action the reaction rate or velocity of the reaction at constant pressure, volume and temperature is proportional to the product of the concentration of the educts:

$$v = \frac{d[C]}{dt} = -\frac{d[A]}{dt} = -\frac{d[B]}{dt} = k[A][B] \ , \tag{3.1}$$

where $[\cdot]$ denotes the concentration of the respective species and k is the reaction-specific kinetic or rate constant. Eq. (3.1) assumes that the reactants interact directly in one mechanistic step without intermediates and is often used for chemical reactions when no further details on the specific reaction mechanism are known. In biological systems, however, a substrate S often reacts to a product P with the help of an enzyme. This reaction can be considered as a two-step mechanism

$$S + E \underset{k_r}{\overset{k_f}{\rightleftharpoons}} ES \xrightarrow{k_{\text{cat}}} P + E \ ,$$

where E is the catalytic enzyme, k_f, k_r and k_{cat} denote rate constants and double arrows indicate that the first reaction is reversible. These reactions can be written as a system of differential equations of the form

$$\begin{aligned}
\frac{d[S]}{dt} = \frac{d[E]}{dt} &= -k_f[S][E] + k_r[ES] \\
\frac{d[ES]}{dt} &= k_f[S][E] - k_r[ES] - k_{\text{cat}}[ES] \\
\frac{d[P]}{dt} &= k_{\text{cat}}[ES] \ .
\end{aligned}$$

Assuming that the intermediate product ES is in quasi-equilibrium, i.e. $\frac{d[ES]}{dt} = 0$, and that the total amount of enzyme is constant, i.e. $[E] + [ES] = [E]_0$ leads to the Michaelis-Menten (or Briggs-Haldane) equation

$$v = \frac{d[P]}{dt} = \frac{v_{\max}[S]}{K_m + [S]} \ , \tag{3.2}$$

where $v_{\max} = k_{\text{cat}}[E]_0$ is the maximum reaction velocity, and $K_m = \frac{k_r + k_{\text{cat}}}{k_f}$ is the so-called Michaelis-Menten constant. The Michaelis-Menten equation is commonly used for enzyme-catalyzed reactions, where the concentration of the substrate by far exceeds the concentration of the catalytic enzyme and saturation of the enzyme is therefore rate-limiting.

The above equations for elementary reactions can be extended to model entire systems of various reacting species,

$$\frac{du}{dt} = F(u) \ ,$$

where the vector $u(t) \in \mathbb{R}^n$ contains the reacting species and the right hand side $F : \mathbb{R}^n \to \mathbb{R}^n$ gives the corresponding reaction rates. Given such complete system of ordinary differential equations based on (3.1) and (3.2) with a defined set of kinetic parameters and starting values, its behavior over time can be computed. In some simple cases analytic solutions can be obtained, but usually complex biological systems are simulated numerically.

In praxis, however, most of the kinetic constants cannot be measured directly and therefore need to be inferred from experimental measurements of the reactive species. This is done by minimizing a cost function, most commonly the sum of square deviations

$$\chi^2(p) = \sum_{i=1}^{n} \frac{(M_i - S_i(p))^2}{E_i^2}$$

between data points M_i and their corresponding model predictions S_i for a given parameter set p, weighted by the respective experimental error E_i. The procedure of parameter estimation, i.e. finding the parameter set p with minimal χ^2, is called fitting and various methods exist to address different problematics. A common difficulty is the insufficiency of experimental measurements for the estimation of all parameters in a complex model. In some cases biological systems may react insensitively to changes in a certain parameter, which as a consequence cannot be estimated at all by a given measuring method. Another problem is the existence of local minima of χ^2 in the parameter space where optimization algorithms may get stuck and thus fail to find the global minimum.

3.2 Hopf bifurcations

Bifurcations occur in ODE systems of the form

$$\frac{du}{dt} = F(u, \mu) \tag{3.3}$$

that depend on a parameter $\mu \in \mathbb{R}$. Here, we assume $F : \mathbb{R}^n \times \mathbb{R} \to \mathbb{R}^n$ to be analytic with the Jacobian matrix $J(u, \mu)$ and the system to have an analytic family of stationary solutions $u^*(\mu)$ with $F(u^*(\mu), \mu) = 0$. Then, the eigenvalues $\lambda_i(\mu)$ of $J(u^*(\mu), \mu)$ can be real or pairs of complex conjugate values and determine the stability of the stationary solution. Bifurcations, i.e. qualitative changes in the behavior of stationary solutions, occur when eigenvalues cross the imaginary axis with variation in μ. While some bifurcations (e.g. pitchfork or saddle-node) change the number of stationary solutions, a Hopf (or Poincaré-Andronov-Hopf) bifurcation changes the dynamic behavior of the system. Namely, a stationary solution gains or loses stability and a family of periodic solutions emerges in a neighborhood of the bifurcation point. Commonly, this point is normalized to $\mu = 0$. The Hopf bifurcation theorem 3.1 gives criteria for such Hopf bifurcations. The concept of the normal form derived in Section 3.2.2 allows to determine the stability and direction of the evolving periodic orbits.

3.2.1 Hopf bifurcation theorem

The conditions for a local Hopf bifurcation have been described first by Hopf (1942) and refined by Hassard et al. (1981). The results are summarized in the following

Theorem 3.1 (Hopf bifurcation theorem). *For* $\mu = 0$ *let exactly two eigenvalues of* J *be purely imaginary,* $\lambda_{1,2}(0) = \pm i\omega \neq 0$. *For their continuation* $\lambda_{1,2}(\mu)$ *let*

$$\frac{d}{d\mu} \operatorname{Re}(\lambda_{1,2}(0)) \neq 0 \; .$$

Then there exists a family of real periodic solutions $u = u(t, \varepsilon)$, $\mu = \mu(\varepsilon)$ *with* $\mu(0) = 0$ *and* $u(t, 0) = u^*(0)$ *but* $u(t, \varepsilon) \neq u^*(\mu(\varepsilon))$ *for sufficiently small* $\varepsilon > 0$. $\mu(\varepsilon)$ *and* $u(t, \varepsilon)$ *are analytic in* 0 *and* $(t, 0)$, *respectively. The same is true for the period* $T(\varepsilon)$ *and*

$$T(0) = \frac{2\pi}{|\omega|} \; .$$

The periodic solutions exist for small μ *either only for* $\mu > 0$, *or only for* $\mu < 0$, *or only for* $\mu = 0$.

3.2.2 Normal form of Hopf bifurcations

In simple words, the normal form of Hopf bifurcations is a two-dimensional reduction of the original system (3.3) that allows to capture the key properties of periodic solutions in a simplified manner. It can be derived by a projection on the center manifold and a nonlinear transformation of variables as shown by Ipsen et al. (1998) and Haragus and Iooss (2011). In the end, the coefficients in the normal form allow to determine the stability and direction of emerging periodic orbits in a Hopf bifurcation.

In the standard theory it is assumed that the Hopf bifurcation occurs in $\mu = 0$. As F is smooth, the system (3.3) possesses a two-dimensional center manifold for sufficiently small μ (Haragus and Iooss, 2011, Theorems 2.9, 3.3). Eq. (3.3) reduced on this manifold and transformed by a specific polynomial transformation is then in the normal form (Haragus and Iooss, 2011)

$$\frac{dA}{dt} = i\omega\, A + a\,\mu\, A + b\, A\,|A|^2 + \mathcal{O}\left(|A|\left(|\mu| + |A|^2\right)^2\right) \tag{3.4}$$

with a complex “amplitude” function A. The parameters a and b in this normal form contain information about the stability and direction of the emerging periodic solutions.

Following Ipsen et al. (1998) and Haragus and Iooss (2011), the solutions u of eq. (3.3) on the center manifold are of the form

$$u = A\xi + \overline{A\xi} + \phi_\mu(A, \overline{A}) + u^*(0), \tag{3.5}$$

where $A(t) \in \mathbb{C}$ is the new amplitude function in (3.4) and $\xi, \overline{\xi} \in \mathbb{C}^n$ are the eigenvectors of the Jacobian $J(u^*(0), 0)$ for the purely imaginary eigenvalues $\lambda_{1,2} = \pm i\omega$. For $\phi_\mu \in \mathbb{C}^n$ a polynomial ansatz in $(A, \overline{A})$ is made with complex coefficient vectors depending on μ. Since the terms $A\xi + \overline{A\xi}$ represent the linear part of the projected system around the steady state $u^*(0)$, ϕ_μ contains only non-linearities. Therefore, $\phi_0(0,0) = 0$, $\partial_A \phi_0(0,0) = 0$, and $\partial_{\overline{A}} \phi_0(0,0) = 0$. Written as

$$\phi_\mu(A, \overline{A}) = \sum \phi_{rsq} A^r \overline{A}^s \mu^q, \tag{3.6}$$

this means that the coefficients $\phi_{100} = \phi_{010} = 0$. Also, $\phi_{rsq} = \overline{\phi}_{srq}$ (Haragus and Iooss, 2011).

Now, we can set the projected function (3.5) into the original equation (3.3)):

$$\begin{aligned} \frac{du}{dt} &= \frac{d(A\xi + \overline{A\xi} + \phi_\mu(A, \overline{A}) + u^*(\mu))}{dt} \\ &= \frac{dA}{dt}\left(\xi + \partial_A \phi_\mu(A, \overline{A})\right) + \frac{d\overline{A}}{dt}\left(\overline{\xi} + \partial_{\overline{A}} \phi_\mu(A, \overline{A})\right) . \end{aligned} \tag{3.7}$$

To obtain the parameters a and b of the normal form (3.4), we use the Taylor expansion of F and the series for ϕ_μ given in eq. (3.6) and compare coefficients in powers of A and μ.

To obtain more general results for a Hopf bifurcation in $\mu^* \neq 0$ we can shift the critical parameter values and stationary solution by setting $\tilde{\mu} := \mu - \mu^*$ and $\tilde{u} := u - u^*(\mu)$. Then, Eq. (3.6) becomes

$$\phi_{\tilde{\mu}}(A, \overline{A}) = \sum \phi_{rsq} A^r \overline{A}^s (\mu - \mu^*)^q \tag{3.8}$$

and

$$\frac{d\tilde{u}}{dt} = F(u^*(\tilde{\mu} + \mu^*) + \tilde{u}, \tilde{\mu} + \mu^*) \; .$$

Knowing the first term in the Taylor expansion of F at $\tilde{\mu} = 0$ and $\tilde{u} = 0$ to be $F(u^*(\mu^*), \mu^*) = 0$ we get

$$\begin{aligned} F(u,\mu) =& D^{10}F \cdot \tilde{u} + D^{10}F \cdot \partial_\mu u^* \tilde{\mu} + D^{01}F\tilde{\mu} + \frac{1}{2}D^{20}F(\tilde{u},\tilde{u}) \\ &+ D^{11}F \cdot \tilde{u}\tilde{\mu} + D^{20}F(\partial_\mu u^*, \tilde{u})\tilde{\mu} + \frac{1}{2}D^{02}F\tilde{\mu}^2 + D^{11}F \cdot \partial_\mu u^* \tilde{\mu}^2 \\ &+ \frac{1}{2}D^{20}F(\partial_\mu u^*, \partial_\mu u^*)\tilde{\mu}^2 + \frac{1}{2}D^{10}F \cdot \partial_\mu^2 u^* \tilde{\mu}^2 + \dots, \end{aligned} \tag{3.9}$$

where $\tilde{u} = A\xi + \overline{A\xi} + \phi_{\tilde{\mu}}(A, \overline{A})$ and the derivatives are defined by

$$D^{pq}F := \left. \frac{\partial^{p+q}F(u,\mu)}{\partial u^p \partial \mu^q} \right|_{(u^*(\mu^*),\mu^*)} .$$

As before, we use $J := D^{10}F$ to denote the Jacobian matrix of F. For higher orders the derivatives in u are multilinear operators like $D^{20}F : (\mathbb{C}^n)^2 \to \mathbb{C}^n$ and $D^{30}F : (\mathbb{C}^n)^3 \to \mathbb{C}^n$ with the i-th component of the result vectors given by

$$\begin{aligned} (D^{20}F(x,y))_i &:= \sum_{j,k}^{n} \frac{\partial^2 F_i}{\partial u_j \partial u_k} x_j y_k \\ (D^{30}F(x,y,z))_i &:= \sum_{j,k,l}^{n} \frac{\partial^3 F_i}{\partial u_j \partial u_k \partial u_l} x_j y_k z_l, \end{aligned}$$

where F_i, u_i, x_i, y_i, z_i denote the components of the vectors F, u, x, y, and z, respectively.

Comparing on the left hand side the ansatz (3.7) for $\tilde{u}$ with the expression (3.8) for $\phi_{\tilde{\mu}}$ and on the right hand side the Taylor expansion (3.9) of F for coefficients in powers of A, $\overline{A}$ and $\tilde{\mu}$, we find:

$$\begin{aligned}
&\mathcal{O}(A): \\
&\qquad i\omega A\xi = D^{10}FA\xi \\
&\qquad \Rightarrow (J - i\omega)\xi = 0 \\
&\mathcal{O}(\overline{A}): \\
&\qquad i\omega\overline{A\xi} = D^{10}F\overline{A\xi} \\
&\qquad \Rightarrow (J + i\omega)\overline{\xi} = 0.
\end{aligned}$$

This is the eigenvalue problem for the Jacobian of F in $(u^*(\mu^*), \mu^*)$. The pair $i\omega$, $-i\omega$ is the pair of complex eigenvalues crossing the imaginary axis, while ξ and $\overline{\xi}$ are the corresponding eigenvectors, so the condition is trivially fulfilled. Further on, we find:

$$\begin{aligned}
&\mathcal{O}(\tilde{\mu}): \\
&\qquad 0 = D^{10}F \cdot \phi_{001}\tilde{\mu} + D^{10}F \cdot \partial_\mu u^*\tilde{\mu} + D^{01}F\tilde{\mu} \\
&\qquad \Rightarrow J \cdot \phi_{001} + J \cdot \partial_\mu u^* + D^{01}F = 0 \\
&\qquad \Rightarrow \phi_{001} = J^{-1}D^{01}F - \partial_\mu u^* \\
&\mathcal{O}(\tilde{\mu}A): \\
&\qquad a\tilde{\mu}A\xi + i\omega A\tilde{\mu}\phi_{101} = D^{10}F \cdot \phi_{101}\tilde{\mu} + D^{20}F(A\xi, \phi_{001})\tilde{\mu} + D^{11}F \cdot A\xi\tilde{\mu} \\
&\qquad \Rightarrow a\xi + (i\omega - J)\phi_{101} = D^{20}F(\xi, \phi_{001}) + D^{11}F \cdot \xi \\
&\qquad \Rightarrow \langle a\xi, \xi^*\rangle + \langle (i\omega - J)\phi_{101}, \xi^*\rangle = \langle D^{20}F(\xi, \phi_{001}) + D^{11}F \cdot \xi, \xi^*\rangle \\
&\qquad \text{with } \langle (i\omega - J)\phi_{101}, \xi^*\rangle = \langle \phi_{101}, (-i\omega - J^*)\xi^*\rangle = \langle \phi_{101}, 0\rangle = 0 \\
&\qquad \text{and } \langle \xi, \xi^*\rangle = 1
\end{aligned}$$

$$\Rightarrow \boxed{a = \langle D^{20}F(\xi, \phi_{001}) + D^{11}F \cdot \xi, \xi^*\rangle} \quad ,$$

where $\langle \cdot, \cdot \rangle$ denotes the Hermitian scalar product, $J^* = J^T$ is the adjoint matrix (or simply transposed, since J is real) to J and ξ^* is the adjoint eigenvector to $-i\omega$ fulfilling $J^*\xi^* = -i\omega\xi^*$, scaled with a complex factor to let $\langle \xi, \xi^*\rangle = 1$. Since J is invertible, the first result can be used to obtain ϕ_{001} and from the second result we can calculate the parameter a in the normal form.

For b we need to go further and consider higher order terms in A and $\overline{A}$:

$\mathcal{O}(A^2)$:

$$
\begin{aligned}
2i\omega A^2\phi_{200} &= D^{10}F\cdot\phi_{200}A^2 + \frac{1}{2}D^{20}F(A\xi, A\xi)\\
\Rightarrow (2i\omega - J)\phi_{200} &= \frac{1}{2}D^{20}F(\xi,\xi)\\
\Rightarrow \phi_{200} &= \frac{1}{2}(2i\omega - J)^{-1}D^{20}F(\xi,\xi)
\end{aligned}
$$

$\mathcal{O}(|A|^2)$:

$$
\begin{aligned}
&0 = D^{10}F\cdot A\overline{A}\phi_{110} + D^{20}F(A\xi, \overline{A\xi})\\
&\Rightarrow -J\phi_{110} = D^{20}F(\xi,\overline{\xi})\\
&\Rightarrow \phi_{110} = -J^{-1}D^{20}F(\xi,\overline{\xi})
\end{aligned}
$$

$\mathcal{O}(A|A|^2)$:

$$
\begin{aligned}
&bA|A|^2\xi + 2i\omega AA\overline{A}\phi_{210} - i\omega\overline{A}A^2\phi_{210}\\
&\qquad = D^{10}F\cdot A^2\overline{A}\phi_{210} + D^{20}F(A\xi, A\overline{A}\phi_{110})\\
&\qquad + D^{20}F(\overline{A\xi}, A^2\phi_{200}) + \frac{1}{2}D^{30}F(A\xi, A\xi, \overline{A\xi})\\
&\Rightarrow bA|A|^2\xi + i\omega A|A|^2\phi_{210}\\
&\qquad = A|A|^2J\cdot\phi_{210} + A|A|^2D^{20}F(\xi,\phi_{110}) + A|A|^2D^{20}F(\overline{\xi},\phi_{200})\\
&\qquad + \frac{1}{2}A|A|^2D^{30}F(\xi,\xi,\overline{\xi})\\
&\Rightarrow b\xi + (i\omega - J)\phi_{210}\\
&\qquad = D^{20}F(\xi,\phi_{110}) + D^{20}F(\overline{\xi},\phi_{200}) + \frac{1}{2}D^{30}F(\xi,\xi,\overline{\xi})\\
&\Rightarrow \langle b\xi,\xi^*\rangle = \langle D^{20}F(\xi,\phi_{110}) + D^{20}F(\overline{\xi},\phi_{200}) + \frac{1}{2}D^{30}F(\xi,\xi,\overline{\xi}),\xi^*\rangle
\end{aligned}
$$

$$
\Rightarrow \boxed{b = \langle D^{20}F(\xi,\phi_{110}) + D^{20}F(\overline{\xi},\phi_{200}) + \tfrac{1}{2}D^{30}F(\xi,\xi,\overline{\xi}),\xi^*\rangle}
$$

Since $2i\omega$ and 0 are not eigenvalues of J by the assumptions of the Hopf bifurcation theorem 3.1, these equations can be solved successively and lead to a formula for the constant b.

Due to the normal form theory, the sign of the real part of b contains information on the type of Hopf bifurcation and stability of the evolving periodic solutions. If $\operatorname{Re} b < 0$, stable periodic orbits arise at the side of the bifurcation where the steady state becomes unstable. This is called a *supercritical* Hopf bifurcation. A *subcritical* Hopf bifurcation occurs if the real part of b is positive and unstable orbits arise at the side of the bifurcation where the steady state

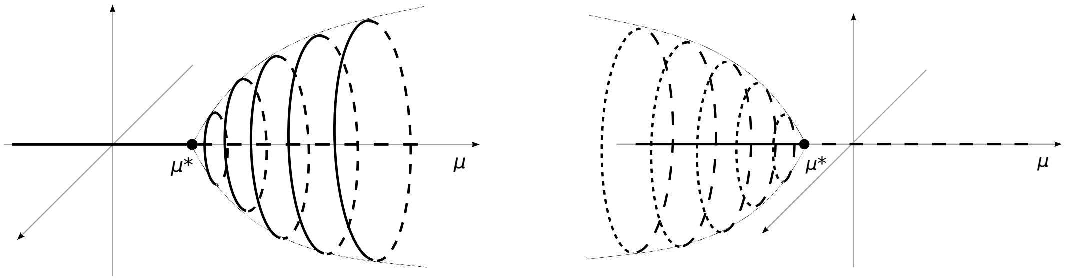

(a) **(b)**

Figure 3.1: (a) Supercritical Hopf bifurcation: a stable steady state (solid line left) becomes unstable in μ^* and stable oscillations emerge to the right. (b) Subcritical Hopf bifurcation: a stable steady state becomes unstable in μ^* and unstable oscillations emerge to the left.

is stable. A graphical illustration of these types in two dimensions is given in Fig. 3.1.

The results on the stability of periodic solutions in the normal form of the Hopf bifurcation can be interpreted by studying the time evolution of small perturbations of the amplitude function A. We recall the normal form (3.4)

$$\frac{dA}{dt} = i\omega A + a\mu A + bA|A|^2 + \dots \ .$$

Then for a small perturbation δA in the direction of A, i.e. $\delta A = \varepsilon\, A$ with a small $\varepsilon > 0$, we find up to the order of $A|A|^2$

$$\begin{aligned} \frac{d\delta A}{dt} &= \frac{d(\varepsilon\, A)}{dt} = \varepsilon\, \frac{dA}{dt} \\ &= \varepsilon\, (i\omega A + a\mu A + bA|A|^2) \\ &= i\omega\delta A + a\mu\delta A + b|A|^2\delta A \ . \end{aligned}$$

The evolution of the square modulus of the perturbation $|\delta A|^2 = \delta A\overline{\delta A}$ is then given by

$$\begin{aligned} \frac{d|\delta A|^2}{dt} &= \overline{\delta A}\, \frac{d\delta A}{dt} + \delta A\, \frac{d\overline{\delta A}}{dt} \\ &= i\omega|\delta A|^2 + a\mu|\delta A|^2 + b|A|^2|\delta A|^2 - i\omega A + \overline{a}\mu|\delta A|^2 + \overline{b}|A|^2|\delta A|^2 \\ &= 2\,\mathrm{Re}(a)\mu|\delta A|^2 + 2\,\mathrm{Re}(b)|A|^2|\delta A|^2 \ . \end{aligned}$$

Then, in $\mu = 0$ and a small neighborhood, the evolution of $|\delta A|^2$ is determined by the real part of b. Namely, if $\mathrm{Re}(b) > 0$, the perturbation grows exponentially, while if $\mathrm{Re}(b) < 0$, it falls exponentially.

3.2.3 Global continuation of periodic orbits

While the original results by Hopf (1942) give conditions for the local existence of periodic solutions, later works focused on the global continuation of the periodic solutions. The term "global" Hopf bifurcation was sometimes used to denote only unbounded sets of periodic solutions (Fiedler, 1986). We, however, will use it in the sense of Alexander and Yorke (1978) to mean any non-local continuation of a family of periodic orbits.

The first result on global continuability of periodic orbits for ordinary differential equations was presented in Alexander and Yorke (1978) using methods of algebraic topology. Another proof of the global result was given in Ize (1976) using homotopy theory. The Fuller index, an index for periodic solutions of a system of autonomous equations, was used in Chow and Mallet-Paret (1978) to generalize the global Hopf bifurcation theorem, proved by Alexander and Yorke (1978), to functional differential equations. An *orbit index* and a *center index* were introduced in Mallet-Paret and Yorke (1982) and applied also in Alligood et al. (1983) to analyze the large connected sets of periodic solutions of a one-parameter differential equation. Hopf bifurcation points with a center index of 1 are called *sources*, and those with center index of -1 are called *sinks*. Mallet-Paret and Yorke (1982) showed, that if a set of orbits is bounded with respect to the parameter, solution, and periods of the orbits, then the set must have as many source as sink Hopf bifurcations. Each source is connected to a sink by an oriented one-parameter path of orbits that contains no orbits with zero orbit index. The results on global continuability for locally continuable non-Möbius orbits of general C^1 dynamical systems were obtained in Alligood and Yorke (1984).

Here, we want to cite the main theorems of the above-mentioned authors. The first gives a global version of the Hopf bifurcation theorem:

Theorem 3.2 (Theorem A in Alexander and Yorke (1978)). *With the following assumptions*

1. *A parametrized autonomous differential system*

$$\dot{u} = f(\mu, u) \tag{3.10}$$

is given defined on an n-dimensional C^1 *manifold* M *(n finite). Here* μ *is a parameter ranging over some interval* Λ *of real numbers, and the parametrized cross section*

$$f : \Lambda \times M \to \text{tangent bundle of } M$$

is continuous. Furthermore, it is assumed that for any $\mu \in \Lambda$ *and any initial values* $u \in M$, *the system* (3.10) *has a unique solution for some* *future range of time. If u is a member of the boundary of M, the solution is assumed to remain in the boundary of M. It is supposed for some u_0 in the interior of M that $f(\mu, u_0) = 0$ for all μ in a neighborhood Λ_0 of some μ_0, so that u_0 is a stationary value of* (3.10) *for all $\mu \in \Lambda_0$.*

2. *There exists a linear endomorphism $L(\mu)$ of the tangent space of M at u_0, defined and continuous for $\mu \in \Lambda_0$, such that for any $\mu_1 \in \Lambda_0$,*

   $$\exp^{-1}\left(f(\mu, \exp v)\right) - L(\mu)v = \mathcal{O}(|v|)$$

   as $(\mu, v) \to (\mu_1, 0)$,

3. *The endomorphism $L(\mu_0)$ is non-singular and has a conjugate pair of purely imaginary eigenvalues $\pm i\omega$.*

4. *For μ near but no equal to μ_0, none of the eigenvalues in Mult$_\mu(i\omega)$ has zero real part, where Mult$(i\omega)$ is the ordered set $\{ik_1\omega, ik_2\omega, \ldots, ik_r\omega\}$ (with the k_i positive integers, $1 \leq k_1 \leq k_2 \leq \ldots \leq k_r$) of eigenvalues of $L(\mu_0)$ which are positive integral multiples of $i\omega$, counted with multiplicity, and including $i\omega$. For μ sufficiently close to μ_0, there is a unique set Mult$_\mu(i\omega)$ of eigenvalues close to the set Mult$(i\omega)$.*

5. *The parity of $i\omega$ is odd, where the parity is defined as follows: Let r^+ (r^-) be the number of elements in Mult$_\mu(i\omega)$ with positive real part for $\mu > \mu_0$ ($\mu < \mu_0$). Let $r = r^+ - r^-$. Then the parity of $i\omega$ with respect to L is the parity (even or odd) of r.*

6. *Let $G(\mu, t, u)$ be the solution of* (3.10) *at time $t \geq 0$ given the initial condition $u(0) = u$, and let the set $\mathcal{R}$ catalogue the parameter, period and initial condition of all non-stationary periodic solutions of* (3.10), *i.e.*

   $$\mathcal{R} = \{(\mu, t, u) \in \Lambda \times (0, \infty) \times M | G(\mu, t, u) = u \text{ and } (u, \mu) \text{ is periodic}\}.$$

   Let $t_0 = 2\pi\omega^{-1}$.

it holds that

1. *There exists a connected subset $\mathcal{R}_0$ of the set $\mathcal{R} \cup \{(\mu_0, t_0, u_0)\}$ containing (μ_0, t_0, u_0) and at least one periodic solution. Moreover for some neighborhood $\mathfrak{R}$ of (μ_0, t_0, u_0) in $\Lambda \times [0, \infty) \times M$, if $(\mu, t, u) \in \mathfrak{R} \cap \mathcal{R}$, then for some positive integer $k = k(\mu, t, u)$ such that $ik\omega \in$ Mult$(i\omega)$, the least period of $G(\mu, \cdot, u)$ is $k^{-1}t$.*

2. *In addition one or both of the following are satisfied:*

a) $\mathcal{R}_0$ is not contained in any compact subset of $\Lambda \times [0, \infty) \times M$,

b) There exists a point $(\overline{\mu}, \overline{t}, \overline{u})$ in $\overline{\mathcal{R}}_0 - \mathcal{R}_0$.

3. *Furthermore, for any $(\overline{\mu}, \overline{t}, \overline{u}) \in \overline{\mathcal{R}} - \mathcal{R}$, the solution $\overline{u}$ is stationary for (3.10) with $\mu = \overline{\mu}$. Also for any $\varepsilon > 0$, there is a neighborhood U_ε of $(\overline{\mu}, \overline{t}, \overline{u})$ such that for any $(\mu, t, u) \in U_\varepsilon \cap \mathcal{R}$, all points of the orbit $G(\mu, \cdot, u)$ are of distance less than ε from the point $\overline{u}$.*

Thus the theorem states that the periodic orbits emerging from a Hopf bifurcation point can be continued to a connected family that contains elements for μ arbitrarily close to the boundary of Λ, or contains elements of arbitrarily large period, or contains elements the orbits of which do not lie in any preassigned compact subset of M.

The following two theorems by Mallet-Paret and Yorke (1982) contain general results for paths of periodic orbits (not necessarily oriented). We need only the results for type 0 orbits and therefore leave out conditions used for other types. As before, we use the notation of a system

$$\frac{du}{dt} = f(u, \mu), \quad (u, \mu) \in \mathbb{R}^n \times \mathbb{R}$$

with the bifurcation parameter μ. The system is assumed to have a non-constant periodic solution $u = p_0(t)$ at $\mu = \mu_0$ and a family p_μ of periodic solutions in a neighborhood of μ_0 called the *Poincaré continuation* of p_0. With a new parameter β this family of orbits can interchangeably be written as $(p_\beta(t), \mu_\beta)$. T_β denotes the least period of an orbit. The family (p_β, μ_β) is called a *path*, if $\gamma(\beta) = (p_\beta(0), \mu_\beta)$ is a path, i.e. if its domain J is an interval and $\gamma : J \to \mathbb{R}^n \times \mathbb{R}$ is continuous. The *modulus* M is defined as the sum of period, parameter, and maximal norm of the periodic orbit,

$$M(\gamma, \beta) = T_\beta + |\mu_\beta| + \max_t \|\gamma(\beta)(t)\|,$$

where $\gamma(\beta)(t)$ is the x coordinate at time t of the trajectory starting from $\gamma(\beta)$ at time 0. For an end point β_0 (with $-\infty \leq \beta_0 \leq \infty$) of the domain J of γ the *limit set* is defined as $\Lambda = \Lambda(\beta_0) = \{(u_1, \mu_1) :$ there is a sequence $\beta_i \to \beta$ such that $T(\gamma(\beta_i))$ is bounded and $\mu(\beta_i) \to \mu_1$, and there is a sequence $\{t_i\}$ such that $p(\beta_i, t_i) \to u_1\}$.

Theorem 3.3 (Proposition 5.1 in Mallet-Paret and Yorke (1982))**.** *Let $\gamma(\beta) = (p_\beta, \mu_\beta)$ be a path whose domain is a bounded interval. Let β_0 be an end point of its domain J. Assume*

$$\liminf_{\beta \to \beta_0} M(\gamma, \beta) < \infty .$$

Then the limit set Λ *at* β_0 *is either an orbit or* $\Lambda = \{(u_1, \mu_1)\}$*, where* (u_1, μ_1) *is an isolated center. Furthermore*

$$d(\gamma(\beta), \Lambda) \to 0 \qquad \textit{as } \beta \to \beta_0$$

and

$$\limsup_{\beta \to \beta_0} T(\gamma(\beta)) < \infty \ .$$

The second theorem concretizes the case when the domain J of a path γ is bounded and the path is maximal, i.e. there are no orbits to further extend it beyond an endpoint β_0 of J. Then γ is *open* at an endpoint β_0 if $\beta_0 \notin J$ and *closed* if $\beta_0 \in J$.

Theorem 3.4 (Proposition 5.2 in Mallet-Paret and Yorke (1982))**.** *Let* γ *be a maximal path that is open at an endpoint* β_0*. Then either*

$$M(\gamma, \beta) \to \infty \qquad \textit{as } \beta \to \beta_0$$

or the γ *family of orbits is convergent to a center at* β_0*.*

Center index Following the notation in Mallet-Paret and Yorke (1982), the center index 中 can be defined to distinguish so-called “source” from “sink” Hopf points and thus give the connecting path of orbits a sense of direction. The center index is given by

$$\text{中}\ (u^*, \mu^*) = \chi(-1)^{E(\mu^*)} \ ,$$

where $E(\mu)$ denotes the sum of the multiplicities of the eigenvalues of the Jacobian $DF(u^*(\mu), \mu)$ having strictly positive real parts. $E(\mu+)$ and $E(\mu-)$ denote right- and left-hand limits of E at μ and the number χ is defined by

$$\chi = \frac{1}{2}(E(\mu^*+) - E(\mu^*-)) \ .$$

With this definition, Mallet-Paret and Yorke (1980) formulated the following theorem, reformulated and proved in detail in Mallet-Paret and Yorke (1982). It uses the term *snake* for a set S of periodic orbits on a maximal oriented path.

Theorem 3.5 (Snake Termination Principle in Mallet-Paret and Yorke (1980))**.** *A snake that emanates from a Hopf point either (1) tends to* ∞ *in* $\mathbb{R} \times \mathbb{R}^n$*, (2) has orbits whose periods tend to* ∞*, or (3) leads to a second Hopf point. In this latter case, the two Hopf points must have center indexes of opposite value,* 中 $= +1$ *for one and* 中 $= -1$ *for the other.*

Theorem 3.6 (Snake Termination Principle in Mallet-Paret and Yorke (1982))**.** *The source of an open snake* S *is either* ∞ *or a center, and its sink is either* ∞ *or a center. [...]*

3.3 Modeling with partial differential equations

Ordinary differential equations, as described above, provide useful models that can easily be analyzed and simulated numerically. These models, however, do not consider spatial aspects and processes such as flows and diffusion. Thus, in a biological context they are only valid in a homogeneously mixed fluid, where concentrations do not depend on the spatial coordinate. The assumption of homogeneous mixture is reasonable for small compartments and single cells, where the time scale of diffusion is much faster than reactions. On the tissue and organ level, however, spatial inhomogeneities and transport processes play an important role. To model these processes, partial differential equations are required.

The basis of all partial differential equations used here is a continuity equation that describes the transport of a conserved quantity. Many physical quantities (energy, momentum, electric charge) are conserved under appropriate conditions, most important in biological systems is the conservation of mass. In the differential form the general *continuity equation* is given by

$$\frac{\partial \rho}{\partial t} + \nabla \cdot \mathbf{j} = \sigma \ , \tag{3.11}$$

where ρ is the density of the considered quantity, $\mathbf{j}$ is the flux that will be discussed in more detail below, and the right hand side σ contains generation or degradation terms, called sources and sinks. For a conserved quantity that cannot be created or destroyed, one would find $\sigma = 0$. For reactive chemicals, σ includes reaction terms, where $\sigma > 0$ means that the chemical reaction creates more of the species, whereas $\sigma < 0$ denotes a consumption of the considered species.

From (3.11) one can derive useful equations for water and solute transport in biological systems. Considering water, the flux is given by $\mathbf{j} = \rho \mathbf{v}$ with a flow velocity vector field $\mathbf{v}$. Assuming incompressibility, i.e. ρ is constant, the mass continuity equation (3.11) simplifies to

$$\nabla \cdot \mathbf{v} = 0 \ ,$$

For a solute in a solution the flux $\mathbf{j}$ comprises a diffusive and an advective term. Diffusion is a mixing process that results in mass transport without bulk motion of the fluid. Based on Fick's first law the diffusive flux is proportional to the local concentration gradient

$$\mathbf{j}_{\text{diff}} = -D \nabla \rho$$

with the diffusivity or diffusion coefficient $D \in \mathbb{R}^+$. The law has been found phenomenologically, but can be explained physically with the random walk or Brownian motion of the diffusing particles. Setting the diffusive flux into (3.11) results in the *diffusion equation*

$$\frac{\partial \rho}{\partial t} = \nabla \cdot (D \nabla \rho) + \sigma \ , \tag{3.12}$$

which is a partial differential equation of parabolic type.

When the solute moves due to a bulk motion of the fluid this is called advection. The associated advective flux is given by

$$\mathbf{j}_{\text{adv}} = \rho \mathbf{v}$$

with a velocity vector field $\mathbf{v}$. Setting the advective flux into the continuity equation (3.11) results in the hyperbolic *advection equation*

$$\frac{\partial \rho}{\partial t} = -\nabla \cdot (\rho \mathbf{v}) + \sigma \ . \tag{3.13}$$

If the flow is assumed to be incompressible (i.e. $\nabla \cdot \mathbf{v} = 0$), the equation can be rewritten as

$$\frac{\partial \rho}{\partial t} = -\mathbf{v} \cdot \nabla \rho + \sigma \ .$$

Combining diffusive (3.12) and advective terms (3.13) results in a general *advection-diffusion equation* of the form

$$\frac{\partial \rho}{\partial t} = \nabla \cdot (D \nabla \rho - \rho \mathbf{v}) + \sigma \ . \tag{3.14}$$

This partial differential equation is a good description of transport processes in biological systems. However, it is in general not possible to find an analytic solution of (3.14) and even numerical solutions in 3-D are difficult and costly to compute. While there are stable numerical methods for the parabolic diffusion part, the hyperbolic advection term poses a numerical challenge and requires special treatment. To reduce computation costs it is also advisable to reduce the dimensions of the problem if possible.

4 Models of zinc uptake regulation

4.1 Models of homeostasis

Homeostatic regulation in biological systems is based on genetic regulatory systems, and ultimately, on concentrations. These are positive, which constrains the possibilities of control substantially. In Ni et al. (2009) the positiveness constraint of a robustly regulating enzyme was shown to lead to the need for two separate control mechanisms: for influx and efflux. The homeostatic model proposed in Ni et al. (2009) is

$$\begin{aligned} \frac{dS}{dt} &= I - E \ , \\ \frac{dR}{dt} &= k\,(S - S_s) \ , \end{aligned} \tag{4.1}$$

where $S(t) \in \mathbb{R}^+$ is the regulated species, $I(t) = I(S, R)(t) \in \mathbb{R}^+$ and $E(t) = E(S, R)(t) \in \mathbb{R}^+$ are the influx and efflux, respectively, R is the regulator, k is a coefficient (not necessarily positive) and S_s is the set point concentration. The above model may result in non-physical negative concentrations of the regulator (Ni et al., 2009). Independently of the type of mechanism sought after, the negative term in dR/dt needs certain properties to achieve robustness based on positive concentrations. The approach is to have a term which is linear in R for small R (positiveness), but becomes almost independent of R for larger R (robustness) (Ni et al., 2009).

Eq. (4.1) is an oversimplification of homeostatic control in cells, as substantially more complex mechanisms are needed (compare Figs. 2.2 and 4.3). Also the concept of perfect control is an idealization. Control of zinc fails in cells for low and high external concentrations. The presence of oscillations in perfect homeostasis, (Jolma et al., 2010), poses a problem to living organisms. Strong oscillations could lead to transient, very high and potentially lethal concentrations. Prescinding from perfect regulation could be a compromise between avoiding strong bursts and achieving good control.

Based on biological information available, we will develop several putative models of influx homeostasis in plant root cells. In Section 4.2, a general influx regulation model based on an ordinary differential equation system describing gene expression of transporters, will be developed and non-dimensionalized. Using the general model, the biological model for yeast in Zhao et al. (1998) will be translated into a corresponding mathematical model (Section 4.4). This model is simplified and fitted to transcript level data via a non-linear optimization method (Gegenfurtner, 1992). The mathematical properties of the steady state are analyzed and discussed. In Section 4.5, the experiences won with the yeast model are used to pose three models for plant roots. The possibilities are manifold, for which reason we restrict the models to the most simple cases of: activator only, activator with dimerization and activator-inhibitor.

4.2 General model

The zinc homeostasis mechanisms presented in this manuscript can be arranged into a general model, which will be developed in this section. Zinc homeostasis can be split into two components: short and long term regulation. Short term regulation is fast but rough, while fine tuning is done by long term regulation. The time scale of short term regulation is less than two hours in plant roots (Talke et al., 2006). Long term regulation has a substantially larger time scale of several hours, days, weeks, etc.

We are interested here in short term regulation, which is local in the sense that the processes occur at the level of single cells in plant roots. Other signals besides the fluxes seem not to be transmitted between cells or tissues. This is probably not the case for long term homeostatic control, which might rely on signals transmitted from tissue to tissue. Therefore, the short term response in plant roots and yeast cells is assumed to follow similar laws that can be subdivided into the phases

$$\text{sensing} \longrightarrow \text{transduction} \longrightarrow \text{reaction} \tag{4.2}$$

The zinc status is measured in the sensing phase, decisions are taken in the transduction phase and changes in cytosolic concentration occur in the reaction phase. As mentioned in Section 4.1, both influx and efflux can be adapted to achieve homeostatic control. In plant roots as well as in yeast cells, adaptation of the expression of influx transporters poses the major component of zinc regulation (Eide, 2003; Talke et al., 2006).

Based on the concept presented in Eq. (4.2), the models considered in this chapter have the following structure

Sensing:

$$\begin{aligned}
\tfrac{d\tilde{A}_i}{dt} &= \tilde{p}_{Ai}(\tilde{A}_i,\ldots) \quad - \left(\sum_{j=1}^{n_I} \beta_{ij}\,\tilde{I}_j \boxed{+\beta_{Ai}\,\tilde{Z}} + \gamma_{Ai}\right) \tilde{A}_i && , \; i = 1,\ldots,n_A \;, \\
\tfrac{d\tilde{I}_i}{dt} &= \boxed{\tilde{p}_{Ii}(\tilde{I}_i,\tilde{Z},\ldots)} - \left(\sum_{j=1}^{n_A} \beta_{ij}\,\tilde{A}_j \boxed{+\beta_{Ii}\,\tilde{Z}} + \gamma_{Ii}\right) \tilde{I}_i && , \; i = 1,\ldots,n_I \;, \\
\tfrac{d\tilde{T}_i}{dt} &= \alpha_{Ti}\,\tilde{M}_i - \gamma_{Ti}\,\tilde{T}_i \boxed{-\beta_{Ti}\,\tilde{T}_i\,\tilde{Z}} && , \; i = 1,\ldots,n_T \;,
\end{aligned}$$

Transduction:

$$\begin{aligned}
\tfrac{dG_i}{dt} &= \boxed{\tilde{\mathcal{A}}_i\left((1+\tilde{\mathcal{I}}_i)^{-1} - G_i\right)} - \gamma_{Gi}\,G_i && \\
\tfrac{d\tilde{M}_i}{dt} &= \boxed{\alpha_{Mi}\,G_i} - \gamma_{Mi}\,\tilde{M}_i && , \; i = 1,\ldots,n_T \;, \\
\tfrac{d\tilde{T}_i}{dt} &= \boxed{\alpha_{Ti}\,\tilde{M}_i} - \gamma_{Ti}\,\tilde{T}_i - \beta_{Ti}\,\tilde{T}_i\,\tilde{Z} &&
\end{aligned}$$

Reaction:

$$\tfrac{d\tilde{Z}}{dt} = \boxed{\sum_{j=1}^{n_T} \alpha_j\,\tilde{T}_j\,f(Z^e,K^t_j)} - \sum_{j=1}^{n_E} \beta_j \tilde{E}_j\,f(Z,K^e_j) - \gamma\,\tilde{Z} \;, \tag{4.3}$$

where $\tilde{Z}$ and Z^e are the cytosolic and external zinc concentrations, respectively, $\tilde{A}_i$ are activators, $\tilde{I}_i$ inhibitors, $\tilde{T}_i$ and $\tilde{E}_i$ influx and efflux transporters, respectively, G_i and $\tilde{M}_i$ the levels of gene expression and mRNA of $\tilde{T}_i$, respectively, and $\tilde{p}_{Ai}$ and $\tilde{p}_{Ii}$ are model dependent production terms. The total activation and repression are

$$\tilde{\mathcal{A}}_i = \sum_{j=1}^{n_A} \alpha_{ij}\,\tilde{A}_j + \sum_{j,k=1}^{n_A} \alpha_{ij}^{\,k}\,\tilde{A}_j\,\tilde{A}_k \quad \text{and} \quad \tilde{\mathcal{I}}_i = \sum_{j=1}^{n_I} \kappa_{ij}\tilde{I}_j \;. \tag{4.4}$$

The function $f(Z,K)$ describes saturation of the transporters

$$f(Z,K) = \frac{Z}{Z+K} \;.$$

Sensing is assumed to take place via binding of cytosolic zinc $\tilde{Z}$ to the activators $\tilde{A}_i$ or inhibitors $\tilde{I}_i$. The possibility that the transporters $\tilde{T}_i$ sense the cytosolic zinc concentration $\tilde{Z}$ directly was also introduced. To achieve regulation, the total activation $\tilde{\mathcal{A}}_i$ has to decrease with higher $\tilde{Z}$ values (see Section 4.1).

Transduction is modeled in the usual way (Keener and Sneyd, 2009). Three equations per protein are needed, namely for: gene activity G_i, transcription into $\tilde{M}_i$ and translation into $\tilde{T}_i$. The activators are introduced as essential transcription factors activating the gene transcription, i.e.

$$\frac{dG_i}{dt} = \tilde{\mathcal{A}}_i \overline{G_i} - \gamma_{Gi} G_i \ , \tag{4.5}$$

where $\overline{G_i}$ is the inactive gene open for binding of the activator and G_i is the activated form. The quadratic form in Eq. (4.4) allows to include dimerization. Total gene activity is normalized to 1, so in the case without gene repression by an inhibitor the proportion of inactive gene in Eq. (4.5) is $\overline{G_i} = 1 - G_i$. The inhibitors inhibit either the activators or directly repress gene activity through $\tilde{\mathcal{I}}_i$. Gene repression was assumed to be non-competitive and fast compared to activation, i.e. it is in quasi-equilibrium and κ_{ij} are equilibrium constants. Then the proportion of non-repressed gene equals $(\tilde{\mathcal{I}}_i + 1)^{-1}$ and the amount of inactive gene in Eq. 4.5 reduces to $\overline{G_i} = (\tilde{\mathcal{I}}_i + 1)^{-1} - G_i$. The production of $\tilde{M}_i$ and $\tilde{T}_i$ is then proportional to the amount of G_i and $\tilde{M}_i$, respectively.

Reaction is described by an equation for the cytosolic zinc concentration, which contains essentially the difference between influx and efflux mediated by $\tilde{T}_i$ and $\tilde{E}_i$, respectively, and a general consumption term -$\gamma \, \tilde{Z}$ that may include transporter independent outflow, sequestration, and dilution effects from cell growth. Regulation of the efflux transporters $\tilde{E}_i$ was left out of Eq. (4.3), as these vary only slightly in roots and no information on yeast was available. If included into the model, these proteins would follow a similar transduction system as the influx transporters $\tilde{T}_i$.

Non-dimensionalization of the equations in (4.3) is done by choosing characteristic values $M_{0,i}$, $T_{0,i}$, etc. and introducing non-dimensionalized quantities $M_i := \tilde{M}_i / M_{0,i}$, $T_i := \tilde{T}_i / T_{0,i}$, etc. The choice of characteristic values aims to eliminate as many parameters as possible.

Consequently, non-dimensionalization of *Transduction* in is straightforward using

$$M_{0,i} = \frac{\alpha_{Mi}}{\gamma_{Mi}} \ , \quad T_{0,i} = \frac{\alpha_{Ti}}{\gamma_{Ti}} \, M_{0,i} \ , \quad \Gamma_{Ti} = \frac{\beta_{Ti}}{\gamma_{Ti}} \, Z_0 \ ,$$

and the non-dimensionalized total activation and repression

$$\mathcal{A}_i = \sum_{j=1}^{n_A} K_{ij} \, A_j + \sum_{j,k}^{n_A} K_{ij}^{\;k} \, A_j \, A_k \quad \text{and} \quad \mathcal{I}_i = \sum_{j=1}^{n_I} K'_{ij} \, I_j \ , \tag{4.6}$$

with

$$K_{ij} = \frac{\alpha_{ij}}{\gamma_{Gi}} \, A_{0,j} \ , \quad K_{ij}^{\;k} = \frac{\alpha_{ij}^{\;k}}{\gamma_{Gi}} \, A_{0,j} \, A_{0,k} \ , \quad \text{and} \quad K'_{ij} = \frac{\kappa_{ij}}{\gamma_{Gi}} \, I_{0,j} \ .$$

Reaction is non-dimensionalized by choosing

$$Z_0 = \frac{\alpha_1}{\gamma} T_{0,1} \ , \quad \kappa_j = \frac{\alpha_j}{\alpha_1} \frac{T_{0,j}}{T_{0,1}} \quad \text{and} \quad \Gamma_j := \frac{\beta_j}{\gamma} E_{0,j} \ .$$

Non-dimensionalization of *Sensing* depends on the particular structure of the production terms. The decay terms can be non-dimensionalized choosing

$$\Gamma_{ij} = \frac{\beta_{ij}}{\gamma_{Ai}} I_{0,j} \ , \qquad \Gamma'_{ij} = \Gamma_{ij} \frac{\gamma_{Ai}}{\gamma_{Ii}} \frac{A_{0,j}}{I_{0,j}} \ , \qquad \Gamma_{Ai} = \frac{\beta_{Ai}}{\gamma_{Ai}} Z_0 \ , \qquad \Gamma_{Ii} = \frac{\beta_{Ii}}{\gamma_{Ii}} Z_0 \ ,$$

while the productions terms still have to be non-dimensionalized accordingly

$$\begin{aligned} p_{Ai}(A_i, \ldots) &= \frac{1}{\gamma_{Ai}\, A_{0,i}} \tilde{p}_{Ai}(\tilde{A}_i, \ldots) \quad \text{and} \\ p_{Ii}(I_i, Z, \ldots) &= \frac{1}{\gamma_{Ii}\, I_{0,i}} \tilde{p}_{Ii}(\tilde{I}_i, \tilde{Z}, \ldots) \ . \end{aligned}$$

In the end, we obtain a non-dimensionalized regulation system of the form

$$\begin{aligned} \frac{dA_i}{dt} &= \gamma_{Ai} \left(p_{Ai}(A_i, \ldots) - \left(\sum_{j=1}^{n_I} \Gamma_{ij} I_j + \Gamma_{Ai} Z + 1 \right) A_i \right) && , \ i = 1, \ldots, n_A \ , \\ \frac{dI_i}{dt} &= \gamma_{Ii} \left(p_{Ii}(I_i, Z, \ldots) - \left(\sum_{j=1}^{n_A} \Gamma'_{ij} A_j + \Gamma_{Ii} Z + 1 \right) I_i \right) && , \ i = 1, \ldots, n_I \ , \\ \frac{dG_i}{dt} &= \gamma_{Gi} \left(\mathcal{A} \left((1 + \mathcal{I})^{-1} - G_i \right) - G_i \right) && , \ i = 1, \ldots, n_T \ , \\ \frac{dM_i}{dt} &= \gamma_{Mi} \left(G_i - M_i \right) && , \ i = 1, \ldots, n_T \ , \\ \frac{dT_i}{dt} &= \gamma_{Ti} \left(M_i - T_i - \Gamma_{Ti} T_i Z \right) && , \ i = 1, \ldots, n_T \ , \\ \frac{dZ}{dt} &= \gamma \left(\sum_{j=1}^{n_T} \kappa_j T_j f(Z^e, K_j^t) - \sum_{j=1}^{n_E} \Gamma_j E_j f(Z, K_j^e) - Z \right) \ . \end{aligned} \tag{4.7}$$

The regulation system can be written as

$$\frac{dU}{dt} = F(U) \ , \qquad U(0) = U^0 \ , \tag{4.8}$$

with $U = (A_1, .., A_{n_A}, I_1, .., I_{n_I}, G_1, .., G_{n_T}, M_1, .., M_{n_T}, T_1, .., T_{n_T}, Z)^T \in \mathbb{R}^n$, where $n = n_A + n_I + 3n_T + 1$, and $F : \mathbb{R}^n \to \mathbb{R}^n$ is the right hand side of the system as given in (4.7). This system is well-posed and remains positive for positive starting values, as shown in the following

Theorem 4.1. *For any positive parameters and production terms and any initial value* $U^0 \geq 0$*, there exists a unique solution* $U \in C^\infty([0,T])$ *for some* $T > 0$ *of the system* (4.8) *and* $U(t) \geq 0$ *for all* $t \in [0,T]$.

Proof. Since F is locally Lipschitz continuous, we obtain local existence and uniqueness of the solution $U(t)$ of (4.8) by the Picard-Lindelöf theorem on a maximal interval $[0,T]$. To prove the positivity of the solution, we show that 0 is a lower bound for the system (4.8), i.e. that any trajectory $U(t)$ with $U(0) \geq 0$ remains positive for all times $t \in [0,T]$. From the equations in (4.7) and by using the positivity of the coefficients and production terms we obtain the following estimates

$$\begin{aligned}
F_{Ai}(U)|_{A_i=0} &= \gamma_{Ai} p_{Ai} \geq 0 \ , \\
F_{Ii}(U)|_{I_i=0} &= \gamma_{Ii} p_{Ii} \geq 0 \ , \\
F_{Gi}(U)|_{G_i=0} &= \gamma_{Gi} \mathcal{A}(1+\mathcal{I})^{-1} \geq 0 \qquad \text{for } \mathcal{A} \geq 0 \text{ and } \mathcal{I} \geq 0 \ , \\
F_{Mi}(U)|_{M_i=0} &= \gamma_{Mi} G_i \geq 0 \qquad \text{for } G_i \geq 0 \ , \\
F_{Ti}(U)|_{T_i=0} &= \gamma_{Ti} M_i \geq 0 \qquad \text{for } M_i \geq 0 \ , \\
F_{Z}(U)|_{Z=0} &= \gamma \sum_{j=1}^{n_T} \kappa_j T_j f(Z^e, K_j^t) \geq 0 \qquad \text{for } T_j \geq 0 \ ,
\end{aligned}$$

which by the invariant region theorem (Theorem 14.7 in Smoller, 1994; Amann, 1990, Theorem 16.9) imply the lower bound $U \geq 0$. □

Starting from this very general system, we will use knowledge from experimental measurements to describe more specified zinc regulatory systems in yeast and plant roots in the following sections.

4.3 Numerical Methods

The ordinary differential equation systems were simulated with either an explicit eighth-order Runge-Kutta method or an implicit Rosenbrock stepper for stiff differential equations. Steady states were calculated by Newton's method in combination with a continuation method for varying parameters. Jacobians were calculated analytically. The model parameters were determined by fitting the model to measurements. For this purpose, Brent's algorithm was applied to minimize χ^2 (Gegenfurtner, 1992; Bevington and Robinson, 2003). The standard deviation of a measurement was assumed to be proportional to its value and the relative error (17%) was chosen such to obtain a reduced χ^2 of the order of one. This way, low and high values had the same weights and were fitted equally well. Penalties were added to χ^2 to avoid negative parameter values. The confidence intervals were obtained by calculation of the covariance matrix via the Hessian of χ^2 (Bevington and Robinson, 2003). The measurements in Zhao et al. (1998) and Bird et al. (2004) were combined and scaled correctly. Scaling factors were in part included into the fitting process while others were prescribed with given values (personal communication of D. Eide).

4.4 Yeast

4.4.1 Model for ZRT regulation

As described in Chapter 2, Section 2.2, zinc uptake regulation in yeast comprises the two zinc transporters ZRT1 and ZRT2, as well as the transcription factor ZAP1 as the only activator, which is directly inhibited by zinc ions without an inhibitor. The production of the activator, which corresponds to the term $p_{Ai}(A_i, ...)$ in the general model Eq. (4.7), is a system of *Sensing*, *Transduction* and *Regulation* by itself, because ZAP1 acts as its own transcription factor through a positive feedback loop. While *ZRT1* is simply activated by ZAP1, *ZRT2* is both activated and repressed by the same molecule (Bird et al., 2004). Therefore, we assume a model with two binding sites of ZAP1 close to the *ZRT2* gene, one activating and one repressing. The total inactivation $\mathcal{I}_i$ (see Eq. (4.6)) introduces this mechanism into the general model Eq. (4.3). Here, the inhibitor is equal to the activator and only the *ZRT2* gene is affected: $\mathcal{I}_1 = 0$ and $\mathcal{I}_2 = K_2' A$.

Following the framework of the general model and the non-dimensionalization derived in Section 4.2, we obtain the following system:

$$
\begin{aligned}
\tfrac{dG_A}{dt} &= \gamma_{GA} \Big(K_A \, A \, (1 - G_A) - G_A \Big) \\
\tfrac{dM_A}{dt} &= \gamma_{MA} \, (G_A - M_A) \\
\tfrac{dA}{dt} &= \gamma_A \, (M_A - A - \Gamma_A \, Z \, A) \\[1ex]
\tfrac{dG_1}{dt} &= \gamma_{G1} \Big(K_1 \, A \, (1 - G_1) - G_1 \Big), \\
\tfrac{dG_2}{dt} &= \gamma_{G2} \Big(K_2 \, A \Big((1 + K_2' \, A)^{-1} - G_2 \Big) - G_2 \Big) \\
\tfrac{dM_i}{dt} &= \gamma_{Mi} \, (G_i - M_i), \qquad\qquad\qquad i = 1, 2 \\
\tfrac{dT_1}{dt} &= \gamma_{T1} \, (M_1 - T_1 - \Gamma_{T1} \, T_1 \, Z) \\
\tfrac{dT_2}{dt} &= \gamma_{T2} \, (M_2 - T_2) \\[1ex]
\tfrac{dZ}{dt} &= \gamma \Big(T_1 \, f(Z^e, K_1^t) + \kappa \, T_2 \, f(Z^e, K_2^t) - Z \Big).
\end{aligned}
\tag{4.9}
$$

The post-translational regulation of ZRT1 is given by the term $-\gamma_{T1}\,\Gamma_{T1}\,T_1\,Z$. For simplicity the term $-\gamma\,Z$ accounts for all zinc consumption processes. These may include export from the cell through zinc efflux transporters, sequestration into the vacuole and other compartments as well as irreversible binding and chelation of zinc by various proteins in the cytoplasm.

The trivial solution (all species zero) is a steady state of Eq. (4.9). There is at least one non-trivial steady state, which for the activator ZAP1 can be written as a function of the intracellular zinc concentration

$$A^* = \frac{1}{1+\Gamma_A\,Z^*} - \frac{1}{K_A}. \tag{4.10}$$

For A^* not to become negative, this equation poses the condition $K_A > 1 + \Gamma_A\,Z^*$. As K_A is constant and given, this implies that for large Z^* the non-trivial and trivial solutions cross. A detailed analysis of this case is presented below. The case of total deficiency (i.e. $Z^e \to 0$) brings insight into some of the parameters. As expected, we find $Z^* \to 0$, which means that $A^* \to 1 - 1/K_A$. From the biological point of view, A^* is expected to shoot to a value close to 1 for total deficiency, which implies $K_A \gg 1$. Assuming that $A^* \approx 1$ for $Z^e \to 0$, the concentrations of the transporters T_1^* and T_2^* behave for $Z^e \to 0$ as

$$T_1^* \to \frac{1}{1+1/K_1} \quad \text{and} \quad T_2^* \to \frac{1}{1+1/K_2+K_2'/K_2+K_2'}\ .$$

High affinity of ZRT1 and low affinity of ZRT2, i.e. $T_1^* \approx 1$ and $T_2^* \approx 0$ for $Z^e \to 0$, are obtained when the conditions $K_1 \gg 1$ and $K_2' + K_2'/K_2 + 1/K_2 \gg 1$ are fulfilled. Considering $K_2 \approx K_1 \gg 1$, the second condition is essentially $K_2' \gg 1$. Expression of *ZRT2* is maximal for a ZAP1 concentration of $A^* = (K_2\,K_2')^{-1/2}$, while expression of *ZRT1* rises monotonically with A^* and approaches its highest value for $Z^e \to 0$. The non-trivial maximum of *ZRT2* expression is possible, because it is both activated and repressed by ZAP1, and the strength of both competing processes determines the position of the maximum. For a given activation K_2, repression K_2' has to be large to shift the expression maximum towards low A^* and high Z^e.

Using the quantitative data measured in Zhao et al. (1998) and Bird et al. (2004), we estimated the model parameters by a least-square method. These measurements are stationary values of the four unknowns A, T_1, T_2 and Z. The parameters obtained are listed in Table 4.1. These clearly reflect the above conditions for K_A, K_1, K_2 and K_2'. Nevertheless, most of the parameters could only be fitted with very high standard deviations. Especially for K_1, K_2' and Γ_A the standard deviation is more than 50% of the fitted parameter value, which shows that the model reacts rather insensitive towards these parameters. In

Table 4.1: Yeast: parameters

Parameter	Value	± s.d.	Biological meaning
K_A	109	±38	*ZAP1* gene activation by ZAP1
K_1	450	±307	*ZRT1* gene activation by ZAP1
K_2	444	±119	*ZRT2* gene activation by ZAP1
K_2'	2171	±1191	*ZRT2* gene repression by ZAP1
Γ_A	714	±600	posttranslational inhibition of ZAP1 by zinc
Γ_{T1}	29.6	±31.5	posttranslational inhibition of ZRT1 by zinc
κ	6.3	±3.0	relative transport rate of ZRT2
K_1^t / μM	139	±65	Michaelis-Menten constant of ZRT1
K_2^t / μM	2584	±1511	Michaelis-Menten constant of ZRT2

Parameters values and standard deviations obtained by fitting the model to measurements published in Zhao et al. (1998) and Bird et al. (2004).

the case of Γ_{T1} the standard deviation is larger than the parameter value. This means that the existence and strength of posttranslational regulation of ZRT1 through zinc found in experiments cannot be identified by our model based on steady state data. Dynamical data may help to analyze and clarify the role of this process. As shown in Fig. 4.1 the model with the above parameters reproduces the measurements very well.

4.4.2 Roles of ZRT1 and ZRT2

In Zhao et al. (1998) ZRT1 and ZRT2 were proposed to play different roles in zinc uptake of yeast cells. While ZRT1 is most active only in zinc-deficient cells, ZRT2 is transiently active also in zinc-replete cells with external zinc concentration around 1000 μM. This implies that under low external zinc concentrations ZRT1 dominates the overall zinc uptake, while under high external zinc concentration, ZRT2 acts as the major transporter. Our model confirms this behavior.

Fig. 4.2a presents the relative contributions to the total flux. At low external concentrations ZRT1 is responsible for about 80% of the influx, while at replete conditions (above 500 μM) 70% of the influx can be attributed to ZRT2. ZRT1 seems indeed to act as a high affinity transporter with a Michaelis constant $K_1^t = 139\,\mu$M, while ZRT2 has less affinity reflected by a substantially larger $K_2^t = 2584\,\mu$M. A similar ratio was found in Zhao and Eide (1996b),

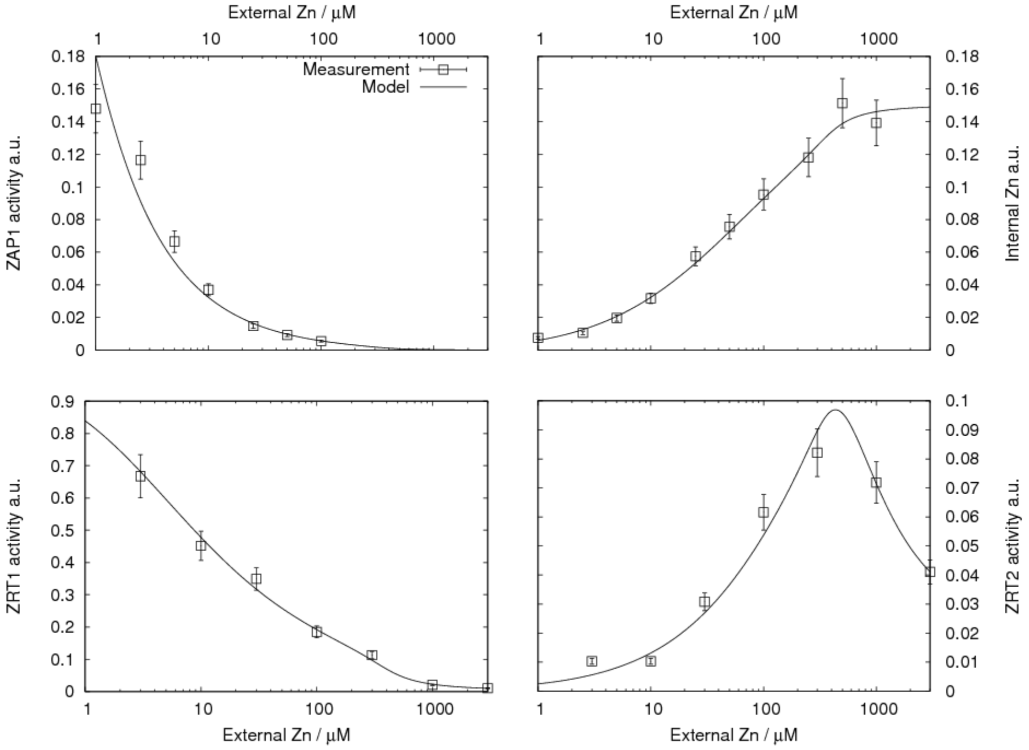

Figure 4.1: Yeast simulations: Comparison between measurements and simulated steady states of ZAP1, internal zinc, ZRT1 and ZRT2 for varying external zinc concentration. Measurements: ZRT1 and ZRT2 from Bird et al. (2004), ZAP1 and zinc from Zhao et al. (1998).

although their values about two orders of magnitude lower, namely $K_1^t \approx 1\,\mu$M and $K_2^t \approx 10\,\mu$M. This discrepancy stems from the assumption made in Zhao and Eide (1996b) that the mechanism is based on pure Michaelis-Menten kinetics without effects of regulation. Assuming regulation to take place on the same time scale as the transport of ions, similarly low values are obtained when Michaelis-Menten is fitted to our simulations. For the example of ZRT1, while Zhao and Eide (1996b) assumed a mechanism

$$v = T_1 \frac{Z^e}{Z^e + K_M} \tag{4.11}$$

for the reaction velocity v with constant amounts of transporter T_1 for all external zinc concentrations Z^e, it is likely that regulatory processes change the amount of transporters giving

$$v = T_1(Z^e) \frac{Z^e}{Z^e + K_1^t} \,. \tag{4.12}$$

Fitting Eq. (4.11) to (4.12) with the parameters shown in Table 4.1 via a Lineweaver-Burk-linearization yields an apparent $K_M \approx 2.2\,\mu$M, which is in the range of the values proposed in Zhao and Eide (1996b). Another reason for proposing high values of K_1^t and K_2^t is that these constants have to be larger than the optimal concentration of the corresponding system, as saturated transporters cannot pass information on external zinc status ($f(Z^e, K_i^t) \approx 1 = \text{const}$ for $Z^e \gg K_i^t$).

ZRT1 is maximally expressed at total deficiency, while *ZRT2* is most active at $430\,\mu$M (Fig. 4.1). A strong repression of *ZRT2* is essential to achieve a maximal expression at high external zinc concentrations (see Table 4.1). However, a strong repression also results in lower gene activities, which explains the low expression level of *ZRT2* compared to *ZRT1* (Fig. 4.1 and Bird et al. (2004)). To compensate the lower expression level, ZRT2 needs to transport zinc at higher rates or more copies need to be produced. This is reflected by the coefficient κ, which suggests that ZRT2 is six times more effective in transporting zinc than ZRT1. Assuming that the ZRT1 and ZRT2 molecules transport zinc at a similar rate, $\kappa \approx 6$ could indicate posttranslational regulation of ZRT1. Direct posttranslational regulation via Γ_{T1}, however, was shown not to be significant here (F-test: $P > 0.05$).

ZRT1 and *ZRT2* were found to be activated equally well by ZAP1, as reflected by the insignificantly small difference between K_1 and K_2. The self-activation constant K_A of *ZAP1*, is four times smaller than K_1 and K_2. This suggests that *ZRT1* and *ZRT2* have more ZAP1-binding promoters than *ZAP1*, which is in concord with experimental results (Zhao et al., 1998).

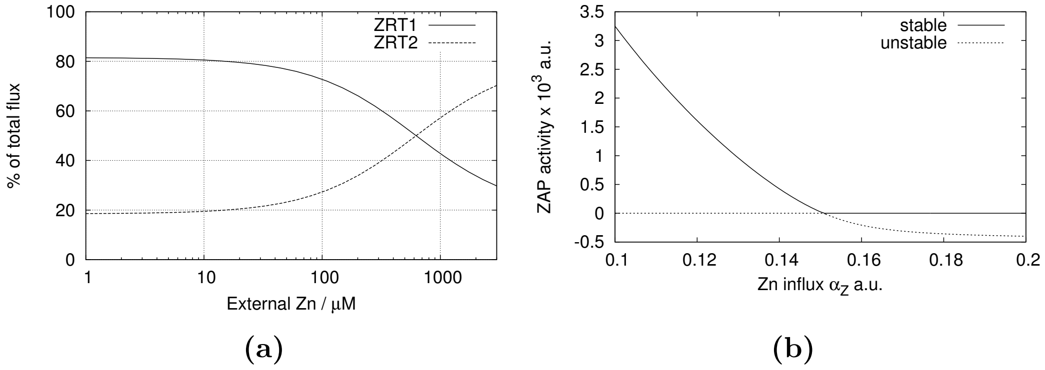

(a) **(b)**

Figure 4.2: Yeast: Role of ZRT1 and ZRT2 and ZAP1 feedback. (a) contributions of ZRT1 or ZRT2 to the total zinc influx for varying external zinc concentration. (b) ZAP activity for varying values of ZRT independent influx α_Z. The stable solution is marked with a solid line, the unstable solution is dotted.

4.4.3 ZAP1 transcriptional feedback

The feedback loop generated by ZAP1 acting as its own transcription factor introduces interesting properties into the model. In Eide (2003) this feedback was proposed to allow a stronger reaction to zinc-limiting conditions. In contrast, our model suggests that the advantage is rather for zinc-replete conditions. The steady state Eq. (4.10) of ZAP1 becomes negative for $Z^* > (K_A - 1)/\Gamma_A \approx 0.15$ and crosses the trivial steady state. Unless these two steady states exchange their roles, the model would become non-biological at the bifurcation. Based on the fitted parameters, the bifurcation is normally reached at very high external zinc concentrations. To examine the behavior of the model at the bifurcation, we introduced a ZRT1- and ZRT2-independent path into the cell. Such a path could for example be another transporter not regulated by ZAP1 and shifts the bifurcation towards lower Z^e. Without considering any details of these processes, the simplest modification is to include an additional constant zinc influx term α_Z to the last line in Eq. (4.9):

$$\frac{dZ}{dt} = \gamma \left(T_1 \, f(Z^e, K_1^t) + \kappa \, T_2 \, f(Z^e, K_2^t) - Z + \alpha_Z \right) .$$

The bifurcation is illustrated in Fig. 4.2b. There are at least two steady states, where one is trivial ($A^* = T_1^* = T_2^* = 0$ and $Z^* = \alpha_Z$) and the other is positive for small α_Z (other negative steady steady states exist). The stability of these are exchanged at the bifurcation. For low α_Z the positive steady state is stable, while the trivial steady state is unstable. After the steady states cross at the

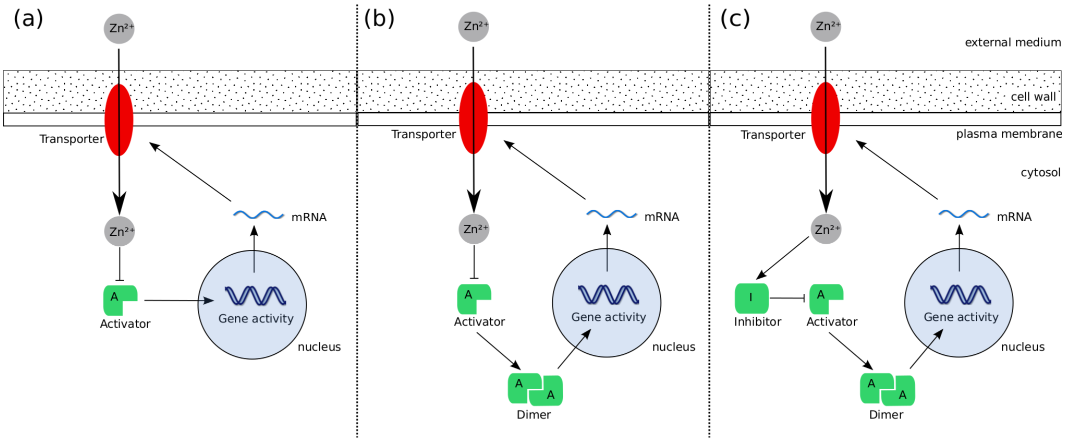

Figure 4.3: Plant roots: Scheme of the three models of zinc uptake regulation. (a) Activator only, (b) Activator with dimerization, (b) Activator-Inhibitor model.

bifurcation, the trivial solution becomes stable while the now negative steady states becomes unstable. The positive steady state is literally trapped by the trivial steady state. From the biological point of view the ZAP1 feedback allows the system to completely switch off expression of *ZAP1* and thus of *ZRT1* and *ZRT2*. In a mechanism without feedback, *ZAP1* expression would just decrease asymptotically towards zero for increasing zinc influx. Therefore, we conclude that the feedback of ZAP1 is advantageous for zinc- replete conditions.

4.5 Plant roots

We now focus on the uptake of zinc into the root cell space without consideration of further transport. By restricting the model to this specific situation, a similar approach as the one for yeast can be applied. We start with a simple model based on only one zinc dependent activator. Hereafter, the advantage of dimerization is analyzed, and a third more involved model based on an activator-inhibitor pair is presented. Using the data in Talke et al. (2006), some of the parameters are obtained via optimization. An F-Test is used to compare the models and select the most reasonable one. Finally, we analyze the relation between stability and robustness of the activator-inhibitor model.

4.5.1 Activator only model

Here, we assume that regulation takes place by one zinc dependent transcription factor (see Fig. 4.3a for a scheme). In terms of the general model Eq. (4.3) we set $n_A = n_T = 1$ and $n_I = 0$ and avoid unnecessary notation by dropping indexes (e.g. $A = A_1$ and $K = K_{11}$, etc.). Sensing is assumed to take place only at the activator level ($\beta_T = 0$). The possibility that the activator dimerizes is also ruled out ($\alpha_{ij}^{\,k} = 0$). Efflux transporters are assumed to be non-saturable, which allows combining efflux/consumption into one term $-\gamma\, Z$. In contrast to the case of yeast, there is no specific information on the production of the activator available. To keep the system simple, we introduce a constant pool A_0 of activator, which is split into active, A, and inactive molecules, $(A_0 - A)$. The net production is set to $\alpha_A\,(A_0 - A)$ and

$$p_A = \alpha_A\, A_0 \qquad \text{and} \qquad \alpha_A = \gamma_A \ . \tag{4.13}$$

The non-dimensionalized system is then

$$\begin{aligned}
\frac{dA}{dt} &= \gamma_A \Big(1 - (1 + \Gamma_A\, Z)\, A\Big) \ , \\
\frac{dG}{dt} &= \gamma_G \Big(K\, A\, (1 - G) - G\Big) \ , \\
\frac{dM}{dt} &= \gamma_M\, (G - M) \ , \\
\frac{dT}{dt} &= \gamma_T\, (M - T) \ , \\
\frac{dZ}{dt} &= \gamma\Big(T\, f(Z^e, K^t) - Z\Big) \ ,
\end{aligned} \tag{4.14}$$

with two steady states

$$\begin{aligned}
T^* &= M^* \;=\; G^* \;=\; \frac{K}{K + 1 + \Gamma_A\, Z^*} \ , \\
A^* &= \frac{1}{1 + \Gamma_A\, Z^*} \ , \\
Z^* &= \frac{1}{\Gamma_A} \left(-\frac{1}{2}\,(K+1) \pm \Big(K\,\Gamma_A\, f(Z^e, K^t) + \frac{1}{4}(K+1)^2\Big)^{\frac{1}{2}}\right) \ .
\end{aligned} \tag{4.15}$$

The steady state with $Z^* < 0$ is biologically irrelevant and therefore not considered. For total deficiency, i.e. $Z^e \to 0$, we find

$$Z^* \to 0 \qquad \text{and} \qquad G^* \to \frac{K}{K+1} \ . \tag{4.16}$$

Biology suggests that gene expression will shoot to a very high value, so G^* should be close to one. This implies: $K \gg 1$. For replete conditions, i.e. $Z^e \to \infty$ and $f(Z^e, K^t) \to 1$,

$$\begin{aligned} Z^* &\to \tfrac{1}{\Gamma_A}\left(-\tfrac{1}{2}(K+1) + \left(K\,\Gamma_A + \tfrac{1}{4}(K+1)^2\right)^{\frac{1}{2}}\right) \qquad \text{and} \\ G^* &\to 1/\left(\tfrac{1}{2} \pm \left(\tfrac{\Gamma_A}{K} + \tfrac{1}{4}\right)^{\frac{1}{2}}\right) \ , \end{aligned} \tag{4.17}$$

where $K \gg 1$ was used. Biology suggests that gene expression should be small for high external zinc concentrations, which implies

$$\Gamma_A \gg K \gg 1 \ . \tag{4.18}$$

For a given Z^e, the steady state depends on three more parameters: K, Γ_A and K^t. While K^t is a property of the transporters, K and Γ_A determine gene activity for extreme conditions. For ZIP1, a value $K^t = 13\,\mu\text{M}$ was published in Grotz et al. (1998) and used here. Assuming gene activity to reach at least 95% for total zinc deficiency, we obtain

$$K \geq 20 \ . \tag{4.19}$$

Determination of K from measurements would need data at very low zinc concentrations, which is uncertain and was not available to the authors. For this reason, an empirical value of $K = 20$ was used. The remaining parameter $\Gamma_A \approx 4.1 \cdot 10^4$ was obtained by fitting the model to published values of *ZIP3* expression (Talke et al., 2006). All parameters are listed in Table 4.2.

Fig. 4.4 shows the steady state as a function of Z^e. Gene activity slightly decreases for increasing Z^e resulting in a continuously increasing internal zinc concentration. Regulation fails for extreme zinc conditions, i.e. undersupply at low Z^e and oversupply for large Z^e. The reason for oversupply is the activator reacting insufficiently to changes in Z^e. By adjusting K and Γ_A, the model only offers the possibility to fix the maximum and minimum of gene expressions, but not the transition steepness between these. Γ_A is also very large compared to the value determined for yeast ($\sim$ 60 times larger; Table 4.1), rendering this simple activator-only model even more unlikely.

4.5.2 Activator model with dimerization

The transcription factors bZIP19 and bZIP23 are known to form dimers (Jakoby et al., 2002). Assuming that only these dimers activate the gene yields $\alpha_{ij}^k \neq 0$ and $\alpha_{ij} = 0$ in the general mode. A scheme of the model is presented in Fig.

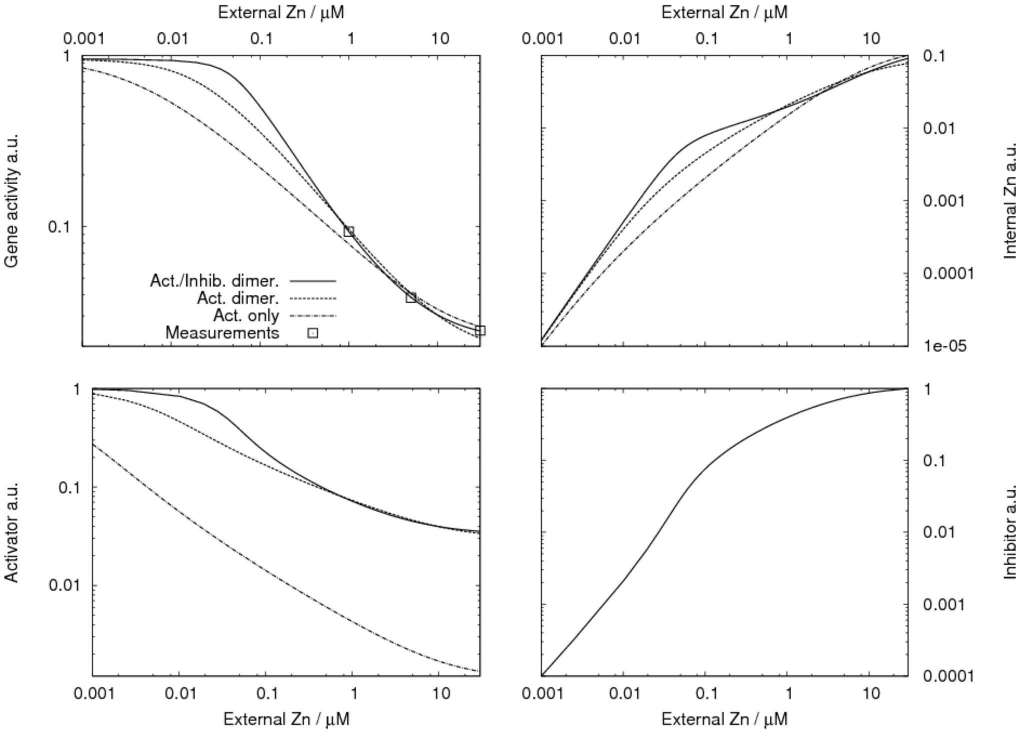

Figure 4.4: Plant roots: Steady states of the different regulation models. The models are: activator only, dimerizing activator and activator-inhibitor pair with dimerization. Measurements in Talke et al. (2006) are also shown.

Table 4.2: Plant roots: parameters used in the simulation of the *activator only*, *dimerized activator* and the *dimerized activator-inhibitor* models.

Parameter	Activ. only	Activ. dimer.	Activ./Inhib. dimer.
K^t $[\mu M]^*$	13	13	13
K	20	20	20
Γ_A	41138	1844	–
Γ	–	–	38
Γ'	–	–	167.2
Γ_I	–	–	1000
$\zeta^\dagger$	–	–	$4.4 \cdot 10^{-3}$
$\xi^\ddagger$	–	–	10^{-3}

* Value for ZIP1, Grotz et al. (1998); † $\zeta = \Gamma'/\Gamma\Gamma_I$; ‡ $\xi = 1/\Gamma_I$.

4.3b. The total activation is here $\mathcal{A} = K\,A^2$, while the rest stays the same as in Eqs. (4.14) and (4.15), meaning that only gene activity needs to be adapted:

$$\begin{aligned} \frac{dG}{dt} &= \gamma_G \Big(K\,A^2\,(1-G) - G\Big)\,, \qquad (4.20) \\ G^* &= \frac{K}{K + (1+\Gamma_A\,Z^*)^2}\,. \end{aligned}$$

Gene activity reacts more sensitive to changes of zinc status than in the non-dimerizing case (Fig. 4.4). The transition between gene on and off is steeper, rendering a more robust mechanism. Fitting the model to the measurements delivers $\Gamma_A \approx 1.8 \cdot 10^3$, which is approximately 20 times smaller than in the non-dimerizing case and substantially closer to the value for yeast. From an evolutionary point of view, dimerization allowed to down-regulate the transporters more strongly with less binding affinity. Also, by assuming that the standard deviations of the measured values are proportional to these, one finds that χ^2 for the model with dimerization is less than half that of the one without when fitted to the measurements in Talke et al. (2006). In total, the model with dimerization statistically and qualitatively outperforms the above activator model, although both models have the same number of degrees of freedom.

4.5.3 Activator-Inhibitor model

Including dimerization delivered a better fit to the measurements than the activator only model. However, a systematic deviation for high values of Z^e was found (Fig. 4.4). Following the proposition in Assunção et al. (2010b) of intermediate steps in sensing, we propose a mechanism involving an activator-inhibitor pair. We assume a competitive inhibition, i.e. the inhibitor can interact whith the activator (the transcription factor) while the latter is not bound to the DNA and the pairs of activator and inhibitor cannot activate the gene. Zinc is assumed to be sensed only by the inhibitor (Fig. 4.3c). Applying these assumptions to the general model Eq. (4.3) gives $n_A = n_I = n_T = 1$. Dimerization again is included by using the total activation $\mathcal{A} = K\,A^2$. Production of the activator is set as in the activator only model (Eq. (4.13)). Sensing occurs at the level of the inhibitor:

$$p_I = \alpha_I\, I_0\, Z \ , \quad \alpha_I = \beta_I \ , \quad \text{and} \quad \beta_A = 0 \ .$$

Transcription and translation are the same as in the dimerizing activator case. The equation for Z stays the same, meaning that the key differences to Eq. (4.14) are

$$\begin{aligned} \frac{dG}{dt} &= \gamma_G \left(K\,A^2\,(1-G) - G\right) \ , \\ \frac{dA}{dt} &= \gamma_A \left(1 - \Gamma\,A\,I - A\right) \ , \\ \frac{dI}{dt} &= \gamma_I \left(\Gamma_I\,Z - \Gamma'\,A\,I - (1+\Gamma_I\,Z)\,I\right) \ . \end{aligned} \tag{4.21}$$

If Z^* is considered to be a parameter in the above system, the steady state is

$$\begin{aligned} G^* &= \frac{K}{K + (1+\Gamma\,I^*)^2} \ , \\ A^* &= \frac{1}{1+\Gamma\,I^*} \ , \\ I^* &= \frac{1}{2}\left(\frac{Z^*-\zeta}{Z^*+\xi} - \frac{1}{\Gamma}\right) \pm \left(\frac{1}{\Gamma}\frac{Z^*}{Z^*+\xi} + \frac{1}{4}\left(\frac{Z^*-\zeta}{Z^*+\xi} - \frac{1}{\Gamma}\right)^2\right)^{\frac{1}{2}} \ , \end{aligned}$$

where $\zeta = \Gamma'/\Gamma\Gamma_I$ and $\xi = 1/\Gamma_I$. The solution with $I^* < 0$ is biologically irrelevant. For totally deficient conditions, i.e. $Z^e \to 0$,

$$I^* \to 0 \ , \quad A^* \to 1 \ , \quad \text{and} \quad G^* \to \frac{K}{K+1} \ .$$

The case of very high external zinc concentration needs to include the expression for Z^*. Instead of determining what happens for $Z^e \to \infty$, we determine the behavior for large internal concentrations, i.e. $Z^* \to \infty$:

$$I^* \to 1 \ , \quad A^* \to \frac{1}{1+\Gamma} \ , \quad \text{and} \quad G^* \to \frac{K}{K+(1+\Gamma)^2} \ .$$

The same biological conditions as those listed in Eqs. (4.18) and (4.19) are found here. In contrast to the activator models, gene activity does not go to zero for $Z^* \to \infty$. Again, the constants Γ and K determine gene activity for extreme zinc levels. The steady state values depend on two more constants: ζ and ξ. The meaning of these constants is found by the following reflection. The first term in I^* is zero for $Z^* = (\Gamma\,\zeta + \xi)/(\Gamma - 1) \approx \zeta$. Is Z^* smaller than this value, the term is negative and has to be compensated by the slightly larger positive square root term, i.e. the inhibitor level I^* stays close to zero. Is Z^* larger than this value, both terms are positive and the inhibitor level I^* increases fast with Z^*. The activator is inhibited substantially and a strong reduction of gene activity is the consequence (compare Fig. 4.5a). Thus, ζ determines the internal zinc concentration for switching the gene from on to off. The constant ξ determines the steepness of the transition between the on and off states (Fig. 4.5b). A small ξ corresponds to a strong binding affinity Γ_I between zinc and inhibitor. The switching steepness is also affected by Γ, as it weights the first term under the root. Large Γ result in steeper switches with a similar effect as decreasing ξ (Fig. 4.6b).

The activator-inhibitor model renders a better and more robust homeostatic control mechanism than the activator only models (Fig. 4.4). Of course, none of these models shows the kind of perfect homeostatic behavior described in Eq. (4.1). Compared to this simple model, the set point for Z^* depends here on the external zinc concentration. The activator-inhibitor model, however, reacts similar to Eq. (4.1) within a small region around $Z^* \approx \zeta$. The reason is the steep genetic switch obtained by the inclusion of an inhibitor, which reacts strongly to the internal zinc status (Fig. 4.5). Fitting the model to the measurements delivered $\Gamma \approx 38$ and $\zeta \approx 4.4 \cdot 10^{-3}$ (Table 4.2). ξ cannot be determined by a fit, because a robust mechanism is sought after and in that regime the model becomes almost independent of ξ (compare Fig. 4.5b) . Therefore, a value of the same order of magnitude as Γ_A for yeast was used ($\xi = 10^{-3} \Rightarrow \Gamma_I = 1000$ while $\Gamma_A = 714$ for yeast). The model describes the measurements very well (Fig. 4.4), which is also a consequence of the small number of degrees of freedom. No systematic deviation for large Z^e was found for this model. An F-Test showed that the activator-inhibitor is statistically more likely, even considering that it contains one more parameter ($P < 0.05$).

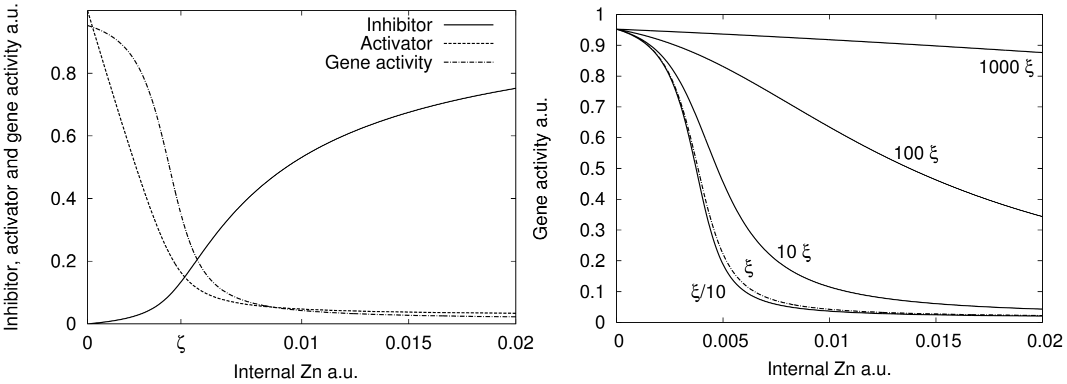

(a) **(b)**

Figure 4.5: Plant roots: Activator-Inhibitor model with dimerization. (a) steady state values of inhibitor, activator and gene activity in dependence of internal zinc concentration. (b) steady state gene activity in dependence of internal zinc status for varying ξ. Dashed curve corresponds to the nominal $\xi = 10^{-3}$.

4.5.4 Robustness and instability

In Jolma et al. (2010) perfect homeostatic control was shown to lead to undamped oscillations. In the case of a toxic substance, oscillations may cause lethal peaks. In view of this, the stability of the activator-inhibitor model was analyzed. Dynamics and stability depend on the time scales involved in the mechanism. The authors could not find suitable data for these. Similar values to those listed in Cook et al. (1998) were used, where the products were assumed to decay four times slower than gene activity. The reader should keep in mind that the specific choice of the time scales influences stability, but the relation between robustness and instability found below should remain valid.

Regarding robustness, a duality between the static and dynamic properties of the activator-inhibitor mechanism was found. Large Γ resulted in a steeper genetic switch and consequently the steady state internal zinc concentration varied less with Z^e (Fig. 4.6b). At a first glance robustness of the mechanism seemed to increase with Γ. However, large Γ lead also to instability of the steady state and to undamped oscillations (Fig. 4.6a). Therefore, from a point of view of the dynamics, robustness decreased for increasing Γ. During one oscillation period, the internal zinc concentration reached up to 3.5 times the steady state value (oscillation amplitudes for $10\,\Gamma$ also shown in Fig. 4.6b), meaning that strong and possibly toxic periodic peaks of zinc were produced. These peaks exceeded the steady state concentration for the nominal Γ. We

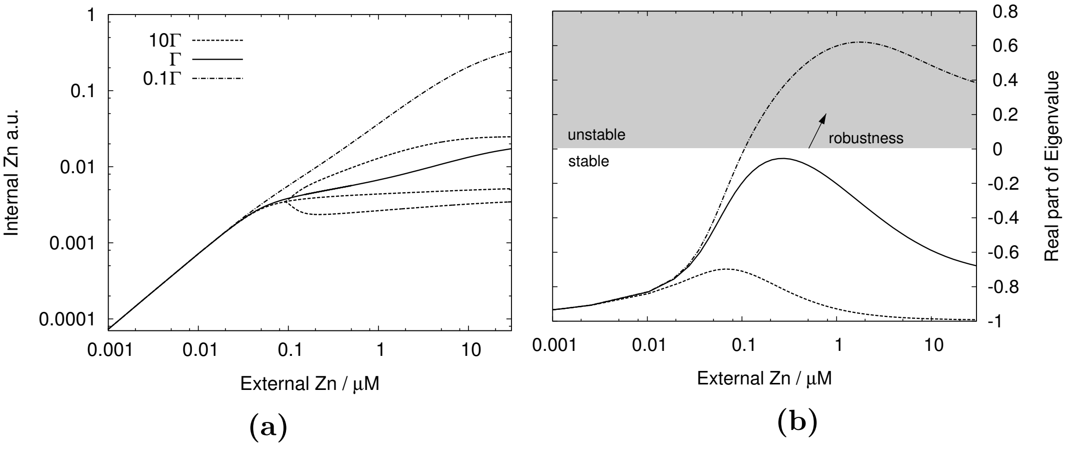

(a) **(b)**

Figure 4.6: Plant roots: Robustness and stability. Robustness and stability of the activator-inhibitor model for 0.1Γ, Γ and 10Γ and varying external zinc concentration. (a) Internal zinc concentration. Minimal and maximal values of limit cycle shown for unstable steady state (10Γ). (b) Real part of largest eigenvalue.

conclude that toxicity for high external zinc concentrations could either occur because of stable high internal zinc concentrations (small Γ) or due to toxic high amplitude oscillations (large Γ). Reducing the perfectness of the homeostatic control could be a strategy to avoid strong zinc bursts, but cells might also use other mechanisms to damp strong oscillations, e.g. buffering and sequestration. These processes will be discussed in detail in Chapter 7.

5 Hopf bifurcation in the ZIP system

5.1 Introduction

In the last Chapter 4 we have studied mathematical models describing different mechanisms for the regulation of ZIP transporters. The most promising model identified in this study was the activator-inhibitor model. It appeared to have the most robust regulatory mechanism. In the analysis of this model, however, we noticed the occurrence of oscillations for certain parameter choices. Here, we analyze the Hopf bifurcation leading to these oscillations in more mathematical detail. In Section 5.2 we introduce the simplified model used in this chapter and consider the well-posedness and uniform boundedness of the solutions as well as the existence of a unique stationary solution. In Section 5.3 we will show the existence of two local Hopf bifurcations for critical values of the bifurcation parameter Z^e and by deriving the normal form in Section 5.4 analyze the stability of the periodic orbits in a neighborhood of the two Hopf bifurcation points. Furthermore, in Section 5.5 we show the existence of a global continuous path of periodic orbits between the two Hopf bifurcation points and in Section 5.6 analyze the stability of periodic solutions by calculating the Floquet multipliers via the monodromy matrix.

5.2 Model description

The activator-inhibitor model presented in Chapter 4, Section 4.5.3, included a dimerizing activator A, as well as an inhibitor I that senses the internal zinc concentration Z and inhibits the activator. Gene activity (denoted by G) is induced by the activator and leads to transcription of mRNA (M) and production of ZIP transporter proteins (T).

We now consider a simplification of the original system, where transcription and translation of transporter proteins are assumed to be quasi-stationary and in equilibrium $G = M = T$. Thereby, the system reduces to four equations

Table 5.1: Parameter values for the ZIP regulation model.

Parameter	value	Biological meaning
K^t	13	Michaelis-Menten constant of ZIP
K	20	Gene activation rate by activator
Γ_I	1000	Binding constant of zinc to inhibitor
Γ	380	Binding constant of activator and inhibitor (scaled for activator)
Γ'	1672	Binding constant of activator and inhibitor (scaled for inhibitor)

describing the time evolution of gene activity G, internal zinc concentration Z, activator A and inhibitor I. For further simplification, all the time constants γ_i in (4.7) are set to one, resulting in

$$\begin{aligned}\frac{dG}{dt} &= KA^2(1-G) - G\\ \frac{dZ}{dt} &= Gf(Z^e, K^t) - Z\\ \frac{dA}{dt} &= 1 - \Gamma AI - A\\ \frac{dI}{dt} &= \Gamma_I Z - \Gamma' AI - (1+\Gamma_I Z)I,\end{aligned} \tag{5.1}$$

where $f(Z^e, K^t) = \frac{Z^e}{Z^e+K^t}$ is a function of the external zinc concentration Z^e. For convenience, we will simply write $f(Z^e)$. Parameter values were obtained in Chapter 4 and are shown in table 5.1. As oscillations appear only for high values of the parameter Γ (see Section 4.5.3), we use $\Gamma = 380$ in this chapter if not stated otherwise. The external zinc concentration Z^e varies naturally in the soil and is therefore taken as the variable bifurcation parameter. Since non-lethal external zinc concentrations for *A. thaliana* have been found in experiments to be in a range of $0\,\mu$M to $30\,\mu$M (Talke et al., 2006), we will use $Z^e \in \mathcal{Z} := [0, 30]$.

For more compact notation we will write $U := (G, Z, A, I)^T$ and $F(U, Z^e) = (F_1(U), F_2(U, Z^e), F_3(U), F_4(U))^T$ with

$$F_1(U) = KA^2(1-G) - G\ , \qquad F_2(U, Z^e) = Gf(Z^e, K^t) - Z\ ,$$
$$F_3(U) = 1 - \Gamma AI - A\ , \qquad F_4(U) = \Gamma_I Z - \Gamma' AI - (1+\Gamma_I Z)I\ .$$

Then, the system can be considered as a 4-dimensional autonomous system of ordinary differential equations in the form

$$\frac{dU}{dt} = F(U, Z^e) \; . \tag{5.2}$$

$F(U, Z^e)$ is continuously differentiable in U and its Jacobian matrix is given by

$$J(U, Z^e) = \begin{pmatrix} -KA^2 - 1 & 0 & 2KA(1-G) & 0 \\ f(Z^e) & -1 & 0 & 0 \\ 0 & 0 & -\Gamma I - 1 & -\Gamma A \\ 0 & \Gamma_I(1-I) & -\Gamma' I & -\Gamma' A - 1 - \Gamma_I Z \end{pmatrix} \tag{5.3}$$

Theorem 5.1. *For any initial value $U^0 \in \mathcal{S}$, where $\mathcal{S} = [0,1]^4$, there exists a unique global solution $U \in C^\infty([0,\infty) \times \mathcal{Z})$ of the system* (5.2) *and $U(t, Z^e) \in \mathcal{S}$ for all $t \in [0, \infty)$ and any $Z^e \in \mathcal{Z}$.*

Proof. Due to the local Lipschitz continuity of F, we obtain the local in time existence and uniqueness of a solution $U(t, Z^e)$ of (5.2) by the Picard-Lindelöf theorem. To prove the uniform boundedness of the solution, we show that $\mathcal{S}$ is a positively invariant region for the system (5.2), i.e. that any trajectory $U(t, Z^e)$ with $U(0, Z^e) \in \mathcal{S}$ remains in $\mathcal{S}$ for all times $t \geq 0$. From the equations of the system (5.2) and by using the positivity of the coefficients we obtain the following estimates

$$\begin{aligned} &F_1(U)|_{G=0} = KA^2 \geq 0 \; , && F_2(U)|_{Z=0} = Gf(Z^e) \geq 0 && \text{for } G \geq 0 \; , \\ &F_3(U)|_{A=0} = 1 > 0 \; , && F_4(U)|_{I=0} = \Gamma_I Z \geq 0 && \text{for } Z \geq 0 \; , \end{aligned}$$

which by applying the invariant region theorem (Theorem 14.7 in Smoller, 1994; Amann, 1990, Theorem 16.9) imply the lower bound $U \geq 0$. To show the upper bound we use the fact that $f(Z^e) < 1 \; \forall \; Z^e \in \mathcal{Z}$ and obtain

$$\begin{aligned} &F_1(U)|_{G=1} = -1 < 0 \; , && F_2(U)|_{Z=1} = Gf(Z^e) - 1 \leq 0 && \text{for } G \leq 1 \; , \\ &F_3(U)|_{A=1} = -\Gamma I - 1 \leq 0 \text{ for } I \geq 0 \; , && F_4(U)|_{I=1} = -\Gamma' A - 1 \leq 0 && \text{for } A \geq 0 \; . \end{aligned}$$

Then the invariant region theorem ensures that $U \leq 1$. Thus, any trajectory starting in $\mathcal{S}$ remains bounded within this set. The global existence and uniqueness of a solution of (5.2) is then implied by the uniform boundedness of $U(t, Z^e)$ together with continuous differentiability of F. The smoothness of $F : \mathbb{R}^4 \times \mathcal{Z} \to \mathbb{R}^4$ with respect to U and Z^e ensures also the smoothness of the solutions U of the system (5.2) (Amann, 1990). □

Theorem 5.2. *For any positive parameter set K, K^t, Γ, Γ', Γ_I and any $Z^e \geq 0$, there exists a unique steady state $U^*(Z^e)$ of the system* (5.2) *in $\mathcal{S} = [0,1]^4$. Furthermore, $U^* \in C^\infty((0,\infty))$.*

The proof of Theorem 5.2 will be based on the following two Lemmata. In these, $f := \frac{Z^e}{Z^e + K^t}$ will be used as one parameter instead of Z^e and K^t, as for any $K^t \in (0, \infty)$ the function $f(Z^e)$ is bijective in $[0, \infty)$ and every $f \in (0,1)$ is uniquely identified with a $Z^e \in (0, \infty)$. For $Z^e = 0$ we find $f(Z^e) = 0$ and we can explicitly calculate the values of the unique positive steady state $G = \frac{K}{K+1}$, $Z = 0$, $A = 1$, and $I = 0$. Therefore, in the following we will assume $f \in (0,1)$ and K, Γ, Γ', $\Gamma_I \in (0, \infty)$ and denote the parameter space by $\mathcal{P} := (0,1) \times (0, \infty)^4$ with elements $p = (f, K, \Gamma, \Gamma', \Gamma_I) \in \mathcal{P}$.

Lemma 5.1. *For any $p \in \mathcal{P}$ the system* (5.2) *has at least one steady state $U^* \in \operatorname{int} \mathcal{S}$ and none on $\partial \mathcal{S}$. Further, any steady state $U^* \in \operatorname{int} \mathcal{S}$ corresponds to a root A^* in $\mathcal{S}_A := \left(\frac{1}{1+\Gamma}, 1\right)$ of the polynomial*

$$\begin{aligned}\phi(x) :=& \Gamma' K x^4 + (f\Gamma_I(1+\Gamma) + 1 - \Gamma')Kx^3 \\ &+ (\Gamma' - K - f\Gamma_I K)x^2 + (1-\Gamma')x - 1 \; ,\end{aligned} \tag{5.4}$$

and any root of ϕ in $\mathcal{S}_A$ to precisely one steady state in $\operatorname{int} \mathcal{S}$.

Proof. Since $\mathcal{S}$ is a positively invariant (see Theorem 5.1), compact and convex subset of $\mathbb{R}^4$, existence of a stationary solution U^* of $F(U,p)$ in $\mathcal{S}$ follows from Brouwer's fixed point theorem (Smoller, 1994, cf. Theorem 12.10).

A steady state U^* is a solution of $F(U^*, p) = 0$. Equation $F_3(U^*, p) = 1 - \Gamma A^* I^* - A^* = 0$ implies

$$A^* = \frac{1}{1 + \Gamma I^*} \; . \tag{5.5}$$

This expression is monotonically decreasing in I^* and for $I^* \in [0,1]$ we therefore find $A^* \leq 1$ and $A^* \geq \frac{1}{1+\Gamma}$. From $F_1(U^*, p) = 0$, $F_2(U^*, p) = 0$ and $F_3(U^*, p) = 0$ we find expressions for G^*, Z^* and I^* as functions of A^*:

$$G^* = \frac{KA^{*2}}{1 + KA^{*2}} \; , \quad Z^* = \frac{fKA^{*2}}{1 + KA^{*2}} \; , \quad I^* = \frac{1 - A^*}{\Gamma A^*} \; , \tag{5.6}$$

showing $G^* < 1$ and $Z^* < 1$. G^* and Z^* increase and I^* decreases strictly monotonically with A^*. Since $A^* > 0$ this implies $G^* > 0$, $Z^* > 0$ and $I^* < 1$. Setting $Z^* > 0$ into $F_4(U^*, p) = 0$ delivers $I^* > 0$. Using $I^* \in (0,1)$ in Eq. 5.5 implies $A^* \in \mathcal{S}_A$. Combining everything we find $U^* \in \mathcal{S}$ and $U^* \notin \partial \mathcal{S}$ for all $p \in \mathcal{P}$.

Substituting the equations (5.6) in $F_4(U^*, p) = 0$ yields the equation $\phi(A^*) = 0$. Thus, any steady state U^* corresponds to a root of ϕ in $\mathcal{S}_A$. Conversely, if A^* is a root of ϕ in $\mathcal{S}_A$, then (5.6) delivers unique G^*, Z^*, and I^*, which fulfill $F(U^*, p) = 0$ and $U^* \in \operatorname{int} \mathcal{S}$. □

Lemma 5.2. *The number of steady states of system* (5.2) *in $\mathcal{S}$ is constant for all $p \in \mathcal{P}$ and the determinant of the Jacobian* (5.3) *is strictly positive when evaluated at a steady state $U^* \in \mathcal{S}$.*

Proof. We denote $D := \det J(U^*, p)$ the Jacobian of F in the steady state U^* for a given parameter set $p \in \mathcal{P}$. The equations (5.6) can be used to express G^*, Z^*, and I^* in terms of A^* and the determinant is then

$$\begin{aligned}\det J(U^*(Z^e), Z^e) = & \frac{1}{A^*(1+KA^{*2})}\Big(\Gamma' K^2 A^{*6} + (Kf\Gamma_I + 2\Gamma' + K)KA^{*4} \\ & + (2K + \Gamma')A^{*2} + (2f\Gamma_I(1+\Gamma)A^* - f\Gamma_I)KA^{*2} + 1\Big) .\end{aligned}$$

Apart from $-f\Gamma_I$, all terms are positive. Using $A^* > \frac{1}{1+\Gamma}$ we find

$$2f\Gamma_I(1+\Gamma)A^* - f\Gamma_I > f\Gamma_I > 0 .$$

Thus, $D > 0$ for any $p \in \mathcal{P}$ and any corresponding steady state $U^* \in \mathcal{S}$. Since $\mathcal{P}$ is connected and $\mathbb{N}$ is discrete, the number of steady states in $\mathcal{S}$ could only be non-constant if this number was discontinuous in $\mathcal{P}$. By Lemma 5.1 a steady state U^* cannot enter or leave the compact set $\mathcal{S}$ upon variation of p, because the steady state U^* depends continuously on p and does not cross over $\partial\mathcal{S}$. Hence, the only way the number of steady states could change is by bifurcation of steady states (pitchfork or saddle node), which is not possible because $D > 0$ in $\mathcal{P}$. In total, we find that the number of steady states in $\mathcal{S}$ has to be constant for all $p \in \mathcal{P}$. ☐

Proof of Theorem 5.2. Now we can finish the proof of Theorem 5.2 by choosing one specific parameter set in $\mathcal{P}$, namely $f = \frac{1}{2}$ and $K = \Gamma = \Gamma' = \Gamma_I = 1$ to obtain $\mathcal{S}_A = \left(\frac{1}{2}, 1\right)$ and

$$\phi(x) = x^4 + x^3 - \frac{1}{2}x^2 - 1 .$$

Since the derivative

$$\frac{d\phi}{dx} = 4x^3 + 3x^2 - x > \frac{1}{4} > 0$$

we find that ϕ is strictly monotonic in $\mathcal{S}_A$. On the boundary of $\mathcal{S}_A$ we have $\phi\left(\frac{1}{2}\right) = -\frac{15}{16} < 0$ and $\phi(1) = \frac{1}{2} > 0$. Therefore, ϕ has a unique root in $\mathcal{S}_A$. By Lemma 5.1 this corresponds to exactly one steady state $U^* \in \mathcal{S}$ and from Lemma 5.2 the same holds for any $p \in \mathcal{P}$.

The smoothness of U^* with respect to p follows from the smoothness of F and the implicit function theorem. As f is a smooth function in Z^e for fixed K^t, K, Γ, Γ', and Γ_I, the steady state $U^*(Z^e)$ can also be viewed as a smooth function in Z^e. ☐

5.3 Local Hopf bifurcation

In numerical simulations of the model (5.2) with sufficiently high values of the parameter Γ we observe a stable steady state for small Z^e, which becomes unstable at some critical parameter value Z^e_1 and stable again after some value $Z^e_2 > Z^e_1$. Between these values, i.e. for $Z^e \in (Z^e_1, Z^e_2)$, numerical simulations show the existence of stable limit cycles depending continuously on Z^e. In this section we show that at both critical values of Z^e a Hopf bifurcation occurs.

Theorem 5.3. *There exist two critical values* $Z^e_1, Z^e_2 \in \mathcal{Z}$ *of the external zinc concentration for which a Hopf bifurcation occurs in the system* (5.2).

Proof. We shall show that all criteria for existence of a local Hopf bifurcation (cf. Theorem 3.1 in Chapter 3) are satisfied by the system (5.2). The right hand side $F : \mathbb{R}^4 \times \mathcal{Z} \to \mathbb{R}^4$ of (5.2) is continuously differentiable in U and Z^e. Theorem 5.2 guarantees the existence of a family of unique equilibria $U^*(Z^e)$ inside the invariant set $\mathcal{S}$ depending continuously on Z^e. From this together with the continuity of $f(Z^e) = \frac{Z^e}{Z^e+K^t}$ and of the determinant, we obtain that the eigenvalues $\lambda_i(Z^e)$, $i = 1, 2, 3, 4$ of the Jacobian $J(U^*(Z^e), Z^e)$ evaluated at the stationary solution vary continuously with Z^e.

A diagram of these eigenvalues in the complex plane for different values of Z^e is shown in Fig. 5.1. For $Z^e = 0$ the eigenvalues can be calculated explicitly and are equal to $\lambda_{1,2} = -1$, $\lambda_3 = -K - 1 = -21$ and $\lambda_4 = -\Gamma' - 1 = -1673$. For $Z^e \in (0, 30]$ the eigenvalues were computed numerically by a reduction of the Jacobian matrix to Hessenberg form followed by QR iteration as described in Press et al. (2007).

The two smallest eigenvalues λ_3 and λ_4 have negative real parts for all $Z^e \in \mathcal{Z} = [0, 30]$, while λ_1 and λ_2 form a complex conjugate pair that crosses the imaginary axis in two points (Fig. 5.1). The values of $\lambda_1, \ldots, \lambda_4$ for the critical parameter points $Z^e_1 = 0.189537\ldots$ and $Z^e_2 = 12.6432\ldots$ at which $J(U^*(Z^e), Z^e)$ exhibits two purely imaginary eigenvalues are shown in Table 5.2. The purely imaginary eigenvalues $\lambda_{1,2}(Z^e_i)$ are simple and none of the multiples $n\lambda_{1,2}(Z^e_i)$ with $n \in \mathbb{N} \setminus \{1\}$ is an eigenvalue of $J(U^*(Z^e_i), Z^e_i)$ for $i = 1, 2$. This follows from $\det J(U^*(Z^e_i), Z^e_i) > 0$ and $\operatorname{tr} J(U^*(Z^e_i), Z^e_i) < 0$, which imply $\lambda_{3,4} < 0$. It was shown numerically that the eigenvalues $\lambda_{1,2}(Z^e)$ cross the imaginary axis with non-zero speed, i.e. $\frac{d}{dZ^e} \operatorname{Re} \lambda_i(Z^e_j) \neq 0$ for $i, j = 1, 2$ (see Table 5.2) .

Therefore, based on the Hopf Bifurcation Theorem (cf. Theorem 3.1) we conclude that the system (5.2) has a one-parameter family of periodic solutions bifurcating from the stationary solution in a neighborhood of both critical values Z^e_1 and Z^e_2. $\square$

Table 5.2: Critical values of $Z^e_{1,2}$ with the corresponding eigenvalues $\lambda_1, \dots, \lambda_4$ of the Jacobian matrix, derivative of the real part of the eigenvalue with respect to Z^e and sign of the real part of the parameter b in the normal form.

	Z^e (μM)	$\lambda_{1,2}$	λ_3	λ_4	$\frac{d}{dZ^e}\,\mathrm{Re}(\lambda_{1,2})$	$\mathrm{sgn}(\mathrm{Re}\, b)$
Z^e_1	$0.189\dots$	$\pm i1.983\dots$	$-3.474\dots$	$-238.6\dots$	$1.83\dots$	-1
Z^e_2	$12.64\dots$	$\pm i2.782\dots$	$-5.599\dots$	$-84.43\dots$	$-0.0126\dots$	-1

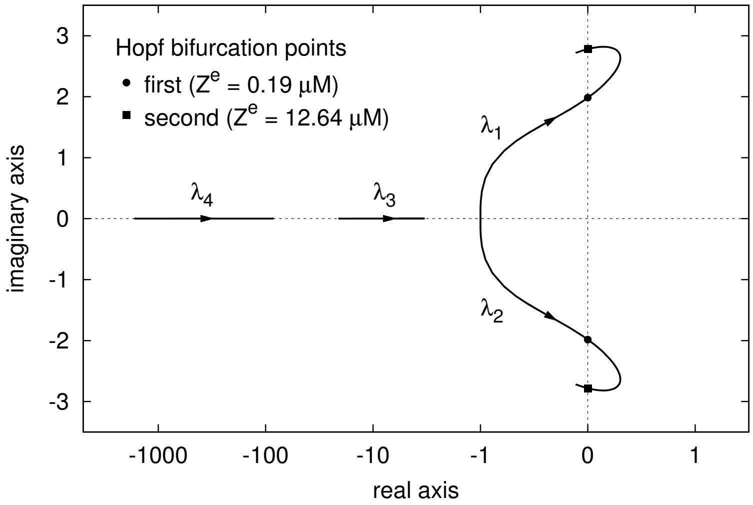

Figure 5.1: Eigenvalues of the Jacobian matrix of F in the steady state for varying external zinc concentrations between $0\,\mu$M and $30\,\mu$M. Arrows show the direction of growing external zinc concentration. The eigenvalues λ_3 and λ_4 are real and negative for the entire range of external zinc concentrations, while the complex conjugate pair $\lambda_{1/2}$ crosses the imaginary axis twice. These points are marked as first and second Hopf bifurcation points.

5.4 Normal form and stability of Hopf bifurcations

In the last section we showed the local existence of periodic orbits close to the two Hopf bifurcation points. Further information is needed to determine the stability and direction of the periodic solutions. To do so we use the concept of the normal form as explained in Section 3.2.2 and calculate the parameter b for the two Hopf bifurcations in the ZIP regulatory system (5.2). As in Eq. (3.4), the normal form of the Hopf bifurcation is given by

$$\frac{dA}{dt} = i\omega\, A + a\,\mu\, A + b\, A\, |A|^2 + \mathcal{O}\left(|A| \left(|\mu| + |A|^2\right)^2\right) \,.$$

The formulas from Section 3.2.2 are used to calculate b.

Theorem 5.4. *At both critical parameter values Z_1^e and Z_2^e a supercritical Hopf bifurcation occurs for the system* (5.2) *and the bifurcating periodic solutions are stable. In the first critical point Z_1^e the orbits arise for increasing values $Z^e > Z_1^e$, whereas in the second critical point Z_2^e the orbits arise for decreasing values $Z^e < Z_2^e$.*

Proof. In order to calculate the parameter b in the normal form, we need a number of derivatives. The Jacobian of the system has already been given in (5.3). Second derivatives are needed in the form $D^{20}F(x,y)$, where $x, y \in \mathbb{C}^4$ analogous. These are given by

$$D^{20}F\left(\begin{pmatrix} x_1 \\ x_2 \\ x_3 \\ x_4 \end{pmatrix}, \begin{pmatrix} y_1 \\ y_2 \\ y_3 \\ y_4 \end{pmatrix}\right) = \begin{pmatrix} -2KA(x_1y_3 + x_3y_1) + 2K(1-G)x_3y_3 \\ 0 \\ -\Gamma(x_3y_4 + x_4y_3) \\ -\Gamma_I(x_2y_4 + x_4y_2) - \Gamma'(x_3y_4 + x_4y_3) \end{pmatrix}.$$

The third derivative term $D^{30}F(x,y,z)$ with $x, y, z \in \mathbb{C}^4$ is computed as

$$D^{30}F\left(\begin{pmatrix} x_1 \\ x_2 \\ x_3 \\ x_4 \end{pmatrix}, \begin{pmatrix} y_1 \\ y_2 \\ y_3 \\ y_4 \end{pmatrix}, \begin{pmatrix} z_1 \\ z_2 \\ z_3 \\ z_4 \end{pmatrix}\right) = \begin{pmatrix} -2K(x_1y_3z_3 + x_3y_1z_3 + x_3y_3z_1) \\ 0 \\ 0 \\ 0 \end{pmatrix}.$$

Having these derivatives, we can now apply the formulas derived in Section 3.2.2 and standard numerical methods like Newton's and continuation methods used to compute stationary solutions and eigenvalues of the Jacobian matrix in Section 5.3, as well as LU decomposition (Press et al., 2007) for equation solving. Thus, we obtain b for the critical parameter values Z_1^e and

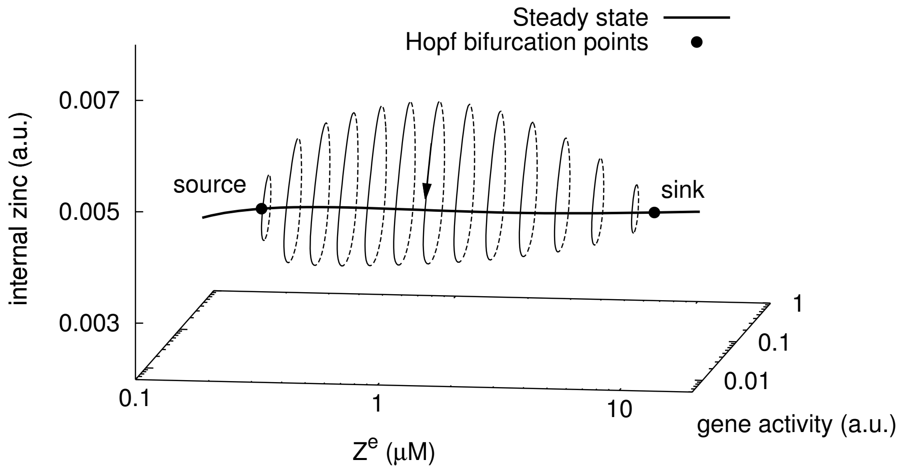

Figure 5.2: Illustration of the snake of periodic orbits between the two Hopf bifurcation points. From the four-dimensional system only two dimensions (gene activity and internal zinc concentration) are shown. The thick solid line marks the steady state, thin lines show the stable periodic solutions. The rotation direction is indicated with an arrow.

Z_2^e. For both cases, $\mathrm{Re}\, b$ is negative (see Table 5.2). Consequently, both Hopf bifurcations are supercritical, i.e. the families of periodic orbits in the neighborhoods of the bifurcations are stable and arise at the side of the bifurcation where the steady state becomes unstable. Therefore, the sign of the derivative $\frac{d}{dZ^e} \mathrm{Re}\, \lambda_1(Z^e),\ i = 1, 2$ determines the direction in which the orbits appear. In the first critical point, the derivative is positive and the orbits arise to the right (i.e. with increasing $Z_1^e < Z^e$), while at the second the derivative is negative and orbits emerge to the left (with decreasing $Z^e < Z_2^e$), as can be seen in Fig. 5.2.

□

5.5 Global continuation of periodic orbits

While the results in Section 5.3 only give the existence of stable periodic orbits in a small neighborhood of the critical values of Z^e, we now want to show the existence of a continuous path of periodic orbits between those two bifurcation points. Section 3.2.3 summarizes the main results that will be applied to the ZIP system in the following.

Theorem 5.5. *The model* (5.2) *possesses a continuous path of periodic solutions connecting two Hopf bifurcation points, where the first point* $(U^*(Z_1^e), Z_1^e)$ *is a source and the second point* $(U^*(Z_2^e), Z_2^e)$ *is a sink for the path.*

Proof. We shall show in the following that for the model (5.2) neither parameter nor period nor solution can become unbounded, so the path of periodic orbits bifurcating from the stationary solution must end in another Hopf point. Theorem 5.1 ensures uniform boundedness of solutions of the model (5.2). The parameter $Z^e \in \mathcal{Z}$ is naturally bounded since zinc concentrations in the soil only appear within a certain range. Here, we chose the non-lethal range for *A. thaliana*, $\mathcal{Z} = [0, 30]$ (Talke et al., 2006). We note, however, since Z^e enters the system only via the term $f(Z^e) < 1$, that its contribution is bounded for all $Z^e > 0$. The least period of the orbits is a continuous function of Z^e. Numerical computations show that the period is also bounded for all $Z^e \in [Z_1^e, Z_2^e]$, see Fig. 5.3(a).

Thus, since parameter, period and solution remain bounded, and the domain $\mathcal{Z}$ of the parameter contains exactly two Hopf bifurcation points, the path of periodic orbits emerging from one Hopf point must terminate in another Hopf point (cf. Theorem 3.3 and 3.4). Therefore, there exists a continuous family of periodic solutions between these two points. An illustration of this path of periodic orbits in two dimensions is given in Fig. 5.2.

To distinguish source from sink Hopf bifurcation points we use the center index 中 (see Section 3.2.3). In our case, exactly two eigenvalues cross the imaginary axis in the critical values $Z_{1,2}^e$. In Z_1^e the two eigenvalues cross the imaginary axis from left to right ($\chi = 1$), whereas in Z_2^e they cross the imaginary axis from right to left ($\chi = -1$). Then with $E(Z_{1,2}^e) = 0$ we find 中 $(U^*(Z_1^e), Z_1^e) = +1$, so the first Hopf bifurcation (left point in figure 5.2) is a source of the path of periodic orbits. For the second Hopf point (right point in figure 5.2) we obtain 中 $(U^*(Z_2^e), Z_2^e) = -1$ showing that it is a sink. This result is in concord with the Snake Termination Principle by Mallet-Paret and Yorke (1980) stating that if a path of periodic orbits emerging from one Hopf point terminates in a second Hopf point, then the two Hopf points must have center indexes of opposite value.

$\square$

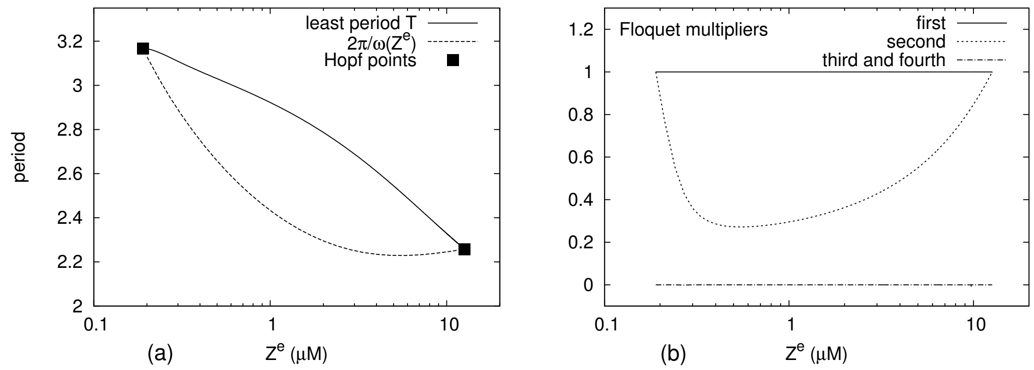

Figure 5.3: Least period $T(Z^e)$ (a) and Floquet multipliers (b) of periodic orbits as a function of the external zinc concentration Z^e between the two Hopf bifurcation points. (a) The numerically computed least period T (solid line) is shown together with the hypothetical period $2\pi/\omega(Z^e)$ of the linearized system in the steady state (dashed line), where $\omega(Z^e)$ is the imaginary part of the first eigenvalue of the Jacobian matrix $J(Z^e)$. In the critical values ($Z_1^e \approx 0.19$ and $Z_2^e \approx 12.6$) the lines cross, showing $\lim_{Z^e \to Z^e_{1,2}} T = 2\pi/\omega(Z^e_{1,2})$. (b) Floquet multipliers were computed numerically. While the first Floquet multiplier equals one, the others are smaller than one. Therefore, the periodic solutions are of type 0 and asymptotically stable for all external zinc concentrations within this range.

5.6 Floquet multipliers and stability of periodic orbits

The stability of periodic solutions can be analyzed by studying its Floquet multipliers. These multipliers can be derived as eigenvalues of the linearized Poincaré map and equivalently as eigenvalues of the monodromy matrix. In the following, we will focus on the latter.

Theorem 5.6. *The periodic solutions of the model* (5.2) *for* $Z^e \in [Z^e_1, Z^e_2]$ *are asymptotically stable.*

Proof. In the previous section we have shown that for a given $Z^e \in [Z^e_1, Z^e_2]$ the system of differential equations (5.2) has a periodic solution $U(t) = U(Z^e, t)$ with a period $T = T(Z^e) \in (0, \infty)$, i.e. $U(T) = U(0)$. Naturally, all integer multiples of T are also periods, so we choose T to be the least period. Similar to a fixed point, the periodic orbit is called asymptotically stable, if trajectories starting near the orbit converge to the orbit for $t \to \infty$. This stability is determined by the eigenvalues of the monodromy matrix.

For $Z^e \in [Z^e_1, Z^e_2]$ let $\Phi_t(U^0)$ denote the solution $U(t)$ at time t starting from $U(0) = U^0$. For a point $(U^0(Z^e), Z^e)$ on a periodic orbit and $T = T(Z^e)$ the least period of this orbit the monodromy matrix is given by

$$M = \frac{\partial \Phi_T(U, Z^e)}{\partial U}\Big|_{U=U^0} .$$

Its eigenvalues are called Floquet multipliers or characteristic multipliers. The Floquet multipliers are independent of the choice of U^0 on the periodic orbit, whereas the monodromy matrix and its eigenvectors do depend on this choice. In an autonomous system like Eq. (5.2), one of the multipliers is always 1 and its eigenvector points in the direction tangent to the periodic cycle, i.e. $F(U^0)$ (Marx and Vogt, 2011). The periodic solution is asymptotically stable, if all other Floquet multipliers are strictly smaller than 1 in modulus (Lust, 2001).

In order to numerically compute the Floquet multipliers we first obtain $U^0(Z^e)$ and $T(Z^e)$ using the single shooting technique (Marx and Vogt, 2011). For a point $U^0(Z^e) \in \mathbb{R}^4$ on a periodic orbit with period $T(Z^e)$ it holds that

$$g(U^0(Z^e), T(Z^e)) := \Phi_T(U^0(Z^e)) - U^0(Z^e) = 0.$$

Since every point on a given orbit fulfills this equation, the system is underdetermined and an additional scalar "phase condition" of the form

$$h(U^0(Z^e), T(Z^e)) = 0$$

is needed. Most simply, the condition fixes one of the components of the vector $U^0(Z^e)$. Here, we estimated the stable periodic orbit by long-time numerical integration of the dynamical system (5.2) by starting slightly off the steady state $U^*(Z^e)$. Then the state $U(\tau, Z^e)$ for some large enough $\tau \in (0, \infty)$ was used to fix the first component $G^0(Z^e)$ by setting $h(U^0(Z^e), T(Z^e)) := G^0(Z^e) - G(\tau, Z^e)$. With this condition the combined system

$$g(U^0(Z^e), T(Z^e)) = 0, \quad h(U^0(Z^e), T(Z^e)) = 0$$

was solved for $(U^0(Z^e), T(Z^e)) \in \mathbb{R}^5$ with a standard Newton algorithm using $U(\tau, Z^e)$ and a rough estimate of $T(Z^e)$ as starting values. Numerical integration of (5.2) was done with a Rosenbrock stiffly stable ODE solver (Press et al., 2007). For regular periodic solution, the Newton iteration converges locally with quadratic rate (Marx and Vogt, 2011, Theorem 6.25). Having $U^0(Z^e)$ and $T(Z^e)$, the derivatives in the monodromy matrix were obtained by the finite difference formula and eigenvalues of the monodromy matrix were calculated using Hessenberg form and QR iteration as before.

The resulting minimal periods are shown in figure 5.3(a), while the resulting Floquet multipliers for varying external zinc concentrations $Z^e \in [Z_1^e, Z_2^e]$ are shown in figure 5.3(b). As confirmed by the theory, the first multiplier in the direction tangent to the periodic orbit equals unity, while the others are real positive and smaller than one in (Z_1^e, Z_2^e). Therefore, the periodic orbits are asymptotically stable for all external zinc concentrations between the two Hopf bifurcation points. In the bifurcation points, the second Floquet multiplier tends to unity and a conclusion on stability cannot be drawn. However, stability there is guaranteed by the normal form (see Section 5.4. Since all the multipliers are smaller than one in modulus for the open interval $Z^e \in (Z_1^e, Z_2^e)$, no secondary bifurcation takes place, i.e. all the periodic orbits are of type 0 (Mallet-Paret and Yorke, 1982). It is also noteworthy that two of the Floquet multipliers are very close to zero. This shows that the periodic solution is strongly attracting in two directions and corresponds in some sense to the two large negative eigenvalues of the Jacobian matrix J of the system (5.2) in the steady state.

$\square$

6 Radial transport of zinc in plant roots

6.1 Introduction

Based on the ZIP regulation model discussed in Chapter 4 we now develop a model for the radial transport of zinc across the root. There are several existent approaches to model water and solute transport through root tissues. One approach is to model transport in analogy to electric resistor networks according to Ohm's and Kirchhoff's laws (Steudle and Frensch, 1996; Steudle and Peterson, 1998). Katou and Taura (1989) and Taura et al. (1988) use advection-diffusion equations to describe water and solute movement in the apoplast. Many modelling approaches concern the interface between soil and root surface (Ptashnyk et al., 2011; Leitner et al., 2009; Zygalakis et al., 2011). However, to my knowledge, there has so far been no attempt to couple a structured transport model in the root tissue to a regulatory model for transporters.

Starting from the ODE model for the regulation of ZIP transporters discussed in Chapter 4 we now want to couple this model with PDEs describing the radial transport. The structure of the root and the processes involved in zinc transport have been introduced in Chapter 2. The regulatory mechanism of ZIP transporters is modeled in Chapter 4. For the sake of simplicity, the root was seen as one compartment there, disregarding the fact that uptake, symplastic transport and xylem loading involve several different cell types (Clemens et al., 2002; Hanikenne et al., 2008). Here we want to extend that model to consider the internal structure of root tissues in more detail. Symplastic and apoplastic transport in a radial geometry will be coupled to the regulatory mechanism to understand the accumulation pattern of symplastic zinc and to find the prerequisites of moving zinc ions from the root surface to the xylem.

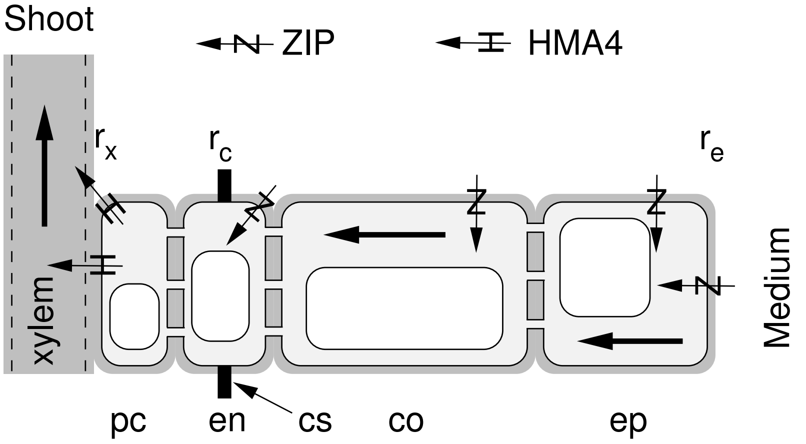

Figure 6.1: Radial scheme of root tissues in *A. thaliana* used for the transport model. The root consists of four tissue types: epidermis (ep), cortex (co), endodermis (en), and pericycle (pc). Water and nutrients move radially from the external medium across the root surface at radius r_e towards the xylem at radius r_x. The impermeable casparian strip is located at position r_c in the endodermis. Zinc is transported across cell membranes by ZIP and HMA4 transporters. Arrows denote the direction of water and zinc fluxes.

6.2 Model

6.2.1 Assumptions

The root geometry is simplified as a single radially symmetric cylinder and transport in the root is assumed to take place in radial direction only. This allows to reduce the three-dimensional problem into coupled one-dimensional problems in the later treatment. The structure of the root along the radius is shown schematically in Fig. 6.1. The root is assumed to be composed of the following cell types (from outside to inside): epidermis (ep), cortex (co), endodermis (en) and pericycle (pc). The cell layers extend from radius r_x (at the pericycle or xylem) to r_e (at the epidermis or outer root surface). A perfectly impermeable Casparian strip (cs) was assumed at position r_c in the endodermis (see Table 6.2 for values). Cell sizes have been estimated for typical young *A. thaliana* roots (see Table 6.1) with a cell wall thickness of $0.5\,\mu$M.

The overall geometry of the root is described in cylindrical coordinates. Reduction from 3-D to 1-D can then be achieved by averaging over the axial coordinate z and the azimuth angle φ. Cells are modeled as blocks, where the symplast volume is denoted by Ω_3 and different parts of the apoplast by Ω_1, Ω_2 and Ω_4 as shown in Fig. 6.2a. The apoplast components Ω_1 and

Table 6.1: Cell sizes used in simulations. Values correspond to a typical young *A. thaliana* root.

Cell type	Left radius (μm)	Right radius (μm)
Pericycle (pc)	6	9.75
Endodermis (en)	10.25	14.75
Cortex (co)	15.25	29.75
Epidermis (ep)	30.25	40

Ω_2 exchange water and ions with the symplast Ω_3, while the contribution of the "edges" Ω_4 is assumed to be negligible. These blocks are thought to be repeated periodically in azimuthal and axial direction. The model focuses on one line of cells as in Fig. 6.1, so we set Ω_i to span over all cell layers from r_x to r_e.

Cells form a continuum connected by plasmodesmata that allow symplastic flow from cell to cell. Within this continuum they have a complex internal structure with organelles, such as vacuoles, nucleus, etc. Plasmodesmata between neighboring cells also reduce the flow cross section substantially. To avoid the treatment of these internal structures, we regard the cell content to be a porous medium with a given volume fraction Φ. Vacuoles are considered only by a reduction of flow cross section, i.e. they are not treated as separate compartments and their role in sequestration is neglected. Cell walls are also assumed to be a porous medium of constant structure and porosity. We introduce a volume fraction Φ for the symplast, which depends only on the radial position. This assumption is valid in view of the periodic structure of the root and the orientation of cell layers (Fig. 6.1). The volume fraction Ψ of the apoplast is assumed to be constant, and based on the results of Kramer et al. (2007) it is set to have a value of 1/15. Fig. 6.3 presents at the bottom graph the volume fraction of the symplast used in the simulations. The volume fraction in plasmodesmata is of the order of 0.15 (Rutschow et al., 2011), while the vacuole is assumed to make up 0.8 of the cell volume giving a cytoplasmic volume fraction of 0.2. These parameters are coarse estimates, but the exact values are not of crucial importance to the model and the simulation results.

Membrane transport of zinc ions is achieved by several different influx and efflux proteins expressed in roots. For the sake of simplicity, we assume the existence of only two types of transporters: influx (ZIP) and efflux (HMA4). Epidermis, cortex and endodermis cells are allowed to have ZIP influx transporters, while pericycle cells produce only HMA4 efflux transporters. Following the results of Talke et al. (2006), the expression of *HMA4* is assumed to be

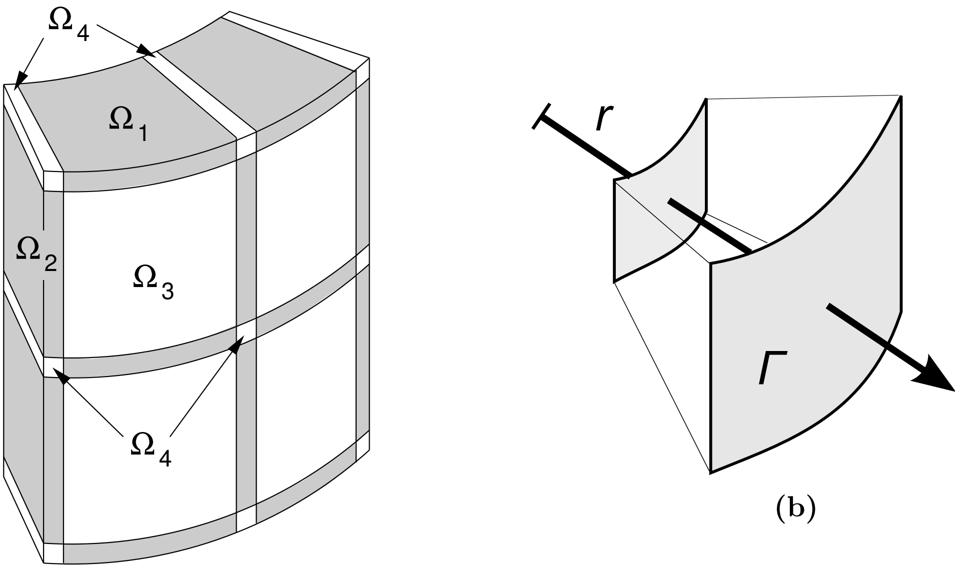

(a) (b)

Figure 6.2: (a) 3-D scheme of root cells showing the different compartments for the transport model. Ω_3 denotes the symplast, Ω_1, Ω_2 and Ω_4 denote different parts of the apoplast above/below and besides the symplast, respectively. (b) Sketch of concentric surfaces $\Gamma(r)$. Zinc concentrations are averaged over Γ to reduce the model from 3-D to 1-D.

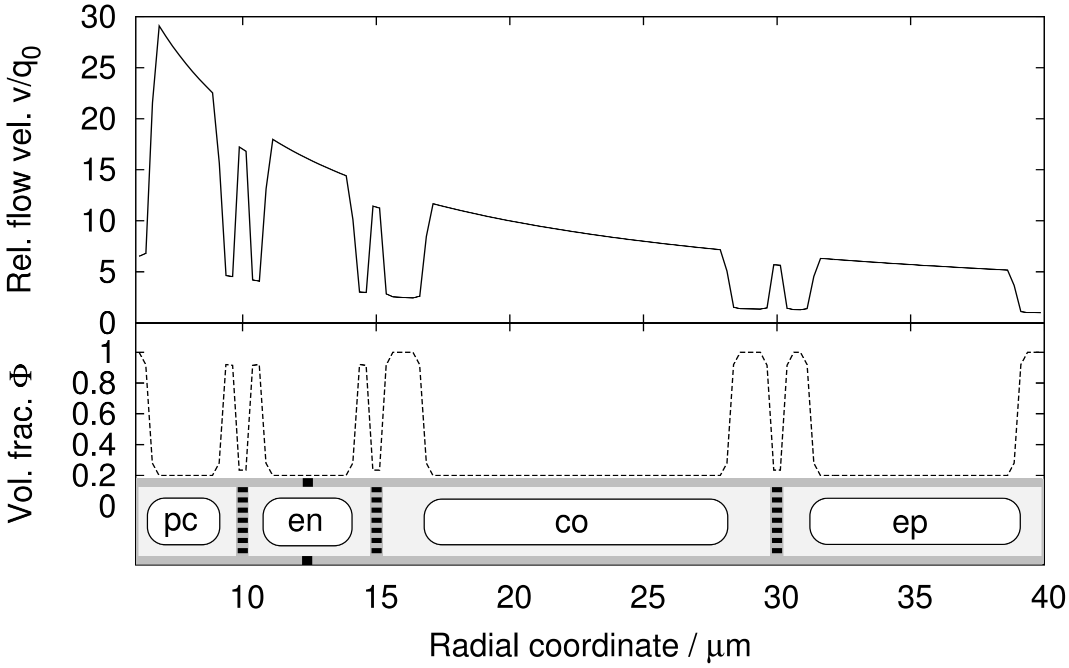

Figure 6.3: Relative water flow velocity v/q_0 (top) and the symplastic volume fraction Φ (bottom) as functions of the radial coordinate. Tissues include the epidermis (ep), cortex (co), endodermis (en) and pericycle (pc). The volume fraction Φ in the symplast varies due to the internal structure of the tissue consisting of cells with large vacuoles and plasmodesmata between neighboring cells. The flow velocity increases towards the xylem due to the radial geometry.

independent of the zinc concentration and is included into the model as a given amount of transporters. Both ZIP and HMA4 are assumed to be saturable. Therefore, transport across the membranes is modelled as an enzymatic reaction with Michaelis-Menten kinetics as described in Chapter 4. The expression of *ZIP* in the epidermis, cortex and endodermis is assumed to adapt to the current internal zinc status based on the dimerizing activator-inhibitor model proposed in Chapter 4. Depending on the average internal zinc concentration each cell regulates its *ZIP* expression independently of the others. The resulting amount of transporters is assumed to be evenly distributed on the plasma membrane and will thus vary from cell to cell, but not within one cell. This assumption is supported by the HMA2 expression pattern found in *A. thaliana* (Sinclair et al., 2007, Fig. 1(c)). The model uses no other type of signal besides the internal zinc concentration. Hence, coordination is achieved merely by zinc fluxes.

6.2.2 Zinc transport

Transport of zinc is modelled by a general advection diffusion problem stating the conservation of zinc

$$\partial_t(\Psi\,\mathcal{Z}_i) - \operatorname{div}(\Psi\, D\, \operatorname{grad} \mathcal{Z}_i) = 0 \qquad \text{in } \Omega_i \times (0,\infty)\ ,\ i = 1,\,2\ , \tag{6.1}$$

$$\partial_t(\Phi\,\mathcal{Z}_3) + \operatorname{div}(\Phi\,\mathbf{v}\,\mathcal{Z}_3 - \Phi\, D\, \operatorname{grad} \mathcal{Z}_3) = 0 \qquad \text{in } \Omega_3 \times (0,\infty)\ , \tag{6.2}$$

where Ψ is the volume fraction of the apoplast $\Omega_{1,2}$, Φ is the volume fraction in the symplast, $\mathcal{Z}_i$ is the zinc concentration in Ω_i, D the diffusion coefficient of zinc, and $\mathbf{v}$ the flow velocity of water. We assume no water fluxes in the apoplast, i.e. advection of zinc in the apoplast was neglected. This assumption is reasonable for simplification, because the small apoplast volume can be expected to contribute little to overall zinc transport, which has been confirmed by preliminary simulations. Leaving out advection in the apoplast makes the numerical simulation much simpler, as advective terms are prone to numerical instabilities.

Solving these equations would deliver the time evolution of three dimensional distributions of zinc in the root tissue. For this purpose, a precise 3-D representation of the tissue and computationally expensive numerical methods would be needed. To avoid this but still capture the essential features on the tissue structure shown in Fig. 6.1, we focused on the radial distribution by reducing Eqs. (6.1), (6.2) into a system of 1-D equations.

Reduction to 1-D

Reduction to 1-D is achieved by averaging zinc concentrations over concentric surfaces $\Gamma(r)$ with radius r as sketched in Fig. 6.2b. These surfaces are given by

$$\Gamma_i\,(r) := \left\{ \mathbf{x} \in \Omega_i \;\middle|\; x_1^2 + x_2^2 = r^2 \right\} \qquad \text{for } i = 1,\,2,\,3\ , \tag{6.3}$$

which can be described in cylindrical coordinates by

$$(r, \varphi,\, z) \in \{r\} \times (0, \varphi_{0,i}) \times (0,\, z_{0,i}) \qquad \text{for } i = 1,\,2,\,3\ ,$$

with azimuth $\varphi_{0,i}$ and height $z_{0,i}$ of the considered domain. We use different polar coordinate systems for Ω_1, Ω_2, and Ω_3. Let $\mu_i\,(r) = r\,\varphi_{0,i}\,z_{0,i}$ denote the area of $\Gamma_i\,(r)$. Then we define Z_i as the average of $\mathcal{Z}_i$ over $\Gamma_i(r) \subset \Omega_i$:

$$Z_i(r,t) := \frac{1}{\mu_i(r)} \int_{\Gamma_i(r)} \mathcal{Z}_i(x,t)\,\mathrm{d}\gamma\ , \qquad \text{for } (r,t) \in [r_x, r_e] \times [0,\infty)\ .$$

We will now average the equation for symplastic transport, Eq. (6.2). The result will also apply to apoplastic transport, Eq. (6.1), by exchanging Φ with

Ψ and setting $v = 0$. For the time derivative we find

$$\frac{1}{\mu_3(r)} \int_{\Gamma_3(r)} \partial_t \left(\Phi\, \mathcal{Z}_3\right) \mathrm{d}\gamma = \partial_t \left(\Phi\, Z_3\right) \ .$$

Averaging of the advection term in (6.2) results in

$$\begin{aligned} \frac{1}{\mu_3(r)} \int_{\Gamma_3(r)} \operatorname{div}(\Phi\, \mathbf{v}\, \mathcal{Z}_3)\, \mathrm{d}\gamma =& \frac{1}{r}\, \partial_r \left(r\, \Phi\, \frac{1}{\mu_3(r)} \int_{\Gamma_3(r)} v_r\, \mathcal{Z}_3\, \mathrm{d}\gamma \right) \\ &+ \frac{1}{\mu_3(r)} \int_{\partial\Gamma_3(r)} \Phi\, v_n\, \mathcal{Z}_3\, \mathrm{d}s \ , \end{aligned}$$

where v_n is the normal velocity on $\partial\Gamma_3$. Assuming no water exchange between symplast and apoplast ($v_n = 0$), the integral over $\partial\Gamma_3$ is zero. By the mean value theorem, there exists a $v(r)$ with

$$\int_{\Gamma_3(r)} v_r\, \mathcal{Z}_3\, \mathrm{d}\gamma = v(r) \int_{\Gamma_3(r)} \mathcal{Z}_3\, \mathrm{d}\gamma \ .$$

This leads to an approximation of the form

$$\frac{1}{\mu_3(r)} \int_{\Gamma_3(r)} \operatorname{div}(\Phi\, \mathbf{v}\, \mathcal{Z}_3)\, \mathrm{d}\gamma \approx \frac{1}{r}\, \partial_r \left(r\, \Phi\, v\, Z_3 \right)$$

with a characteristic radial velocity $v(r)$ that will be derived in Section 6.2.3. The diffusion term in Eq. 6.2 is expressed in cylindrical coordinates by

$$\operatorname{div}(\Phi\, D \operatorname{grad} \mathcal{Z}_3) = \frac{1}{r}\, \partial_r(\Phi\, D\, r\, \partial_r \mathcal{Z}_3) + \frac{1}{r}\, \partial_\varphi \left(\Phi\, D\, \frac{1}{r}\, \partial_\varphi \mathcal{Z}_3 \right) + \partial_z(\Phi\, D\, \partial_z \mathcal{Z}_3) \ .$$

The first term with r-derivative is averaged as

$$-\frac{1}{\mu_3(r)} \int_{\Gamma_3(r)} \frac{1}{r}\, \partial_r(\Phi\, D\, r\, \partial_r \mathcal{Z}_3)\, \mathrm{d}\gamma = -\frac{1}{r}\, \partial_r \left(\Phi\, D\, r\, \partial_r Z_3 \right) \ ,$$

while the term with φ- and z-derivatives is transformed into an integral over the boundary of $\Gamma_3(r)$

$$\begin{aligned} -\frac{1}{\mu_3(r)} \int_{\Gamma_3(r)} & \left(\frac{1}{r}\, \partial_\varphi \left(\frac{\Phi\, D}{r}\, \partial_\varphi \mathcal{Z}_3 \right) + \partial_z(\Phi\, D\, \partial_z \mathcal{Z}_3) \right) \mathrm{d}\gamma \\ &= -\frac{1}{\mu_3(r)} \int_{\partial\Gamma_3(r)} \Phi\, D\, \partial_n \mathcal{Z}_3\, \mathrm{d}s \ , \end{aligned}$$

where $\partial_n \mathcal{Z}_3$ is the normal derivative of $\mathcal{Z}_3$ on $\partial\Gamma_3(r)$. This boundary integral delivers the average flux through the membrane:

$$\begin{aligned} \frac{1}{\mu_3(r)} \int_{\partial\Gamma_3(r)} \Phi\, \left(v_n\, \mathcal{Z}_3 - D\, \partial_n \mathcal{Z}_3 \right) \mathrm{d}s &= -Q_3 \ , \\ Q_i &:= \sum_{j=1}^{2} \sigma_{ij}(r)\, J_j(r) \ , \end{aligned} \tag{6.4}$$

where Q_i, $i = 1, 2$, are zinc source terms and $J_j(r)$, $j = 1, 2$, denote flux densities through the transporters ZIP and HMA4 (see Section 6.2.4) and

$$(\sigma_{ij})(r) := \begin{pmatrix} -2/z_{0,1} & 0 \\ 0 & -2/r\varphi_{0,2} \\ 2/z_{0,3} & 2/r\varphi_{0,3} \end{pmatrix}$$

account for different ratios between the length of the pieces composing the boundary $\partial\Gamma_3$ towards apoplast compartments Γ_1 and Γ_2, respectively, and the area of Γ_3. The sign convention of J_i is as follows: positive for a flux from the apoplast into the symplast and negative vice versa.

In the end, the reduced model for the symplast Ω_3 is obtained as

$$\partial_t(\Phi\, Z_3) + \frac{1}{r}\,\partial_r\left(r\,\Phi\, v\, Z_3 - \Phi\, D\, r\, \partial_r Z_3\right) = Q_3 \qquad \text{in } (r_x, r_e) \times (0, \infty)\;. \tag{6.5}$$

For implementation purposes the equation can be rewritten into a conservative form with the variables rZ_i. Then, applying the reduction for the symplast in Eq. (6.5) also to the apoplast Ω_1 and Ω_2 we obtain

$$\begin{aligned} \partial_t(\Psi\, rZ_1) + \partial_r\Big((D/r)\,\Psi\, rZ_1 - \Psi\, D\, \partial_r(rZ_1)\Big) &= r\,Q_1\;, \\ \partial_t(\Psi\, rZ_2) + \partial_r\Big((D/r)\,\Psi\, rZ_2 - \Psi\, D\, \partial_r(rZ_2)\Big) &= r\,Q_2\;, \\ \partial_t(\Phi\, rZ_3) + \partial_r\Big(\,(v + D/r)\;\Phi\, rZ_3 - \Phi\, D\, \partial_r(rZ_3)\Big) &= r\,Q_3\;, \\ \text{in } (r_x, r_e) \times (0, \infty)\;. \end{aligned} \tag{6.6}$$

Initial values and boundary conditions

Eq. (6.6) needs initial values and suitable boundary contions to obtain a well posed (solvable) problem. The apoplast is assumed to have access to a perfectly stirred medium of concentration Z^e. A concentration $Z^x(t)$ is prescribed at the xylem. This concentration depends on the flux of zinc through HMA4 and a model will be developed in the next section. The impermeability of the Casparian strip is considered by setting a no-flux condition. In total, we prescribe for the apoplasts Ω_1 and Ω_2

$$\left.\begin{aligned} Z_i\Big|_{r=r_x} &= Z^x(t)\;, \\ (D/r)\,\Psi\, rZ_i - \Psi\, D\, \partial_r(rZ_i)\Big|_{r\nearrow r_c} &= 0\;, \\ (D/r)\,\Psi\, rZ_i - \Psi\, D\, \partial_r(rZ_i)\Big|_{r\searrow r_c} &= 0\;, \\ Z_i\Big|_{r=r_e} &= Z^e\;, \end{aligned}\right. \qquad \text{for } t \in [0, \infty),\ i = 1, 2\;. \tag{6.7}$$

The zinc flux is prescribed at the boundary of the symplast Ω_3

$$\left.(v + D/r)\ \Phi\, r Z_3 - \Phi\, D\, \partial_r(r Z_3)\right|_{r=r_x} = r\, H_0\, H_{pc}\, f\Big(Z_3(r_x), K^h\Big)\ , \tag{6.8a}$$

$$\left.(v + D/r)\ \Phi\, r Z_3 - \Phi\, D\, \partial_r(r Z_3)\right|_{r=r_e} = -r\, \Phi\, T_0\, T_{ep}\, f\Big(Z^e, K^t\Big)\ , \tag{6.8b}$$

$$\text{for } t \in [0, \infty)\ .$$

Published experimental results that capture the dynamics of regulation, focus on changes from one steady state at a given external concentration to another steady state for a different concentration (e.g. zinc resupply). Therefore, the initial conditions used here are solutions of the stationary version of Eq. (6.6)

$$\left. Z_i(r,t)\right|_{t=0} = \overline{Z}_i(r) \qquad \text{for } r \in [r_x, r_e]\ ,\ i = 1, 2, 3,$$

where the $\overline{Z}_i$ fulfill one of the following equations

$$\partial_r\Big(\ (D/r)\ \Psi\, r\overline{Z}_i - \Psi\, D\, \partial_r(r\overline{Z}_i)\Big) = r\, Q_i \qquad \text{in } (r_x, r_e) \times (0, \infty)\ ,\ i = 1, 2\ ,$$

$$\partial_r\Big(\ (v + D/r)\ \Phi\, r\overline{Z}_3 - \Phi\, D\, \partial_r(r\overline{Z}_3)\Big) = r\, Q_3 \qquad \text{in } (r_x, r_e) \times (0, \infty)\ ,$$

with boundary conditions Eqs. (6.7), (6.8a) and (6.8b). For dynamic simulations of the system, we use the steady state for given Z^e and q_0 as an initial condition to then capture the transition dynamics when one of these parameters is changed. This models the dynamic adaptation of a real plant to a sudden change in the external zinc concentration or transpiration rate.

Xylem

A calculation of the apoplastic zinc concentration in the region enclosed by the casparian strip ($r_x \le r \le r_c$) needs the concentration of zinc in the xylem. For simplicity, we will pose a model for the central cylinder $0 \le r < r_x$ (i.e. stele without the pericycle) and account the true size of the xylem by a constant volume fraction Ψ_x. The domain describing this tissue will be denoted as Ω_x, where the x stands for *xylem*.

Mass conservation of water and (6.2) apply also to this tissue

$$\operatorname{div}(\Psi_x \mathbf{v}_x) = 0 \qquad \text{in } \Omega_x\ ,$$

$$\partial_t(\Psi_x\, \mathcal{Z}_x) + \operatorname{div}\,(\Psi_x\, \mathbf{v}_x\, \mathcal{Z}_x - \Psi_x\, D\ \operatorname{grad} \mathcal{Z}_x) = 0 \qquad \text{in } \Omega_x \times (0, \infty)\ ,$$

where $\mathbf{v}_x$ is the flow velocity and $\mathcal{Z}_x$ is the zinc concentration in the central cylinder Ω_x. A surface average can be obtained as before in the radial reduction to 1-D. The main difference is that the surface over which the average is created is here the horizontal cross section

$$\Gamma_x\,(z) := \{\, \mathbf{x} \in \Omega_x \mid x_3 = z \}\ .$$

Conservation of water delivers

$$\partial_z(\Psi_x\, v_x) = -\frac{2}{r_x}\Phi(r_x)\, v(r_x)\ , \tag{6.9}$$

where $\Phi(r_x)v(r_x)$ is the flow velocity of the water being delivered from the symplast, and the average velocity in the xylem is defined as

$$v_x(z) := \frac{1}{\mu\Big(\Gamma_x(z)\Big)} \int_{\Gamma_x(z)} v_{z,x}(r, \varphi, z)\, \mathrm{d}\gamma\ , \qquad \text{for } z \in [0, L]\ \ ,$$

where L is the length of the root portion considered. In Section 6.2.3 we will derive an expression for the water flow velocity $v(r)$ given in Eq. (6.15). Expression of $\Phi(r_x)\, v(r_x)$ by this Eq. (6.15), integration of Eq. (6.9), and assumption of $v_x(0) = 0$ delivers

$$v_x(z) = -\frac{2}{r_x}\frac{r_e}{r_x}\frac{q_0}{\Psi_x}\, z \qquad \text{for } z \in [0, L]\ , \tag{6.10}$$

which is a linear function of z. Remeber that $q_0 < 0$ so that $v_x(z) \geq 0$ for $z \geq 0$. Eq. (6.10) is based on the assumption that q_0 is constant, which will not be true in reality. The pressure gradient between the xylem and the medium will fall with z and, hence, $v_x(z)$ cannot grow linearly indefinitelly and will stagnate at a constant value. However, $v_x(z)$ will behave similar to Eq. (6.10) in a region near $z = 0$. We focus on this region and assume validity of Eq. (6.10).

An average for the equation describing the conservation of zinc is obtained readily

$$\partial_t(\Psi_x Z_x) + \partial_z(\Psi_x\, v_x\, Z_x - \Psi_x\, D\, \partial_z Z_x) = \frac{2}{r_x} H_0\, H_{pc}\, f\Big(Z_3(r_x, t), K^h\Big)\ ,$$

where the boundary condition Eq. (6.8a) divided by r was used and the average zinc concentration is defined as

$$Z_x(z, t) := \frac{1}{\mu\Big(\Gamma_x(z)\Big)} \int_{\Gamma_x(z)} \mathcal{Z}_x(x, t)\, \mathrm{d}\gamma \qquad \text{for } (z, t) \in [0, L] \times [0, \infty)\ .$$

A preliminary simulation of this equation with no-flux and open vessel conditions at $z = 0$ and $z = L$, respectivelly, shows that Z_x is almost constant in space. Hence, we set $Z_x(z,t) \approx Z^x(t)$, use that Ψ_x is constant and express v_x by Eq. (6.10) to obtain

$$\begin{aligned} \frac{dZ^x}{dt} &= \frac{1}{\Psi_x}\frac{2}{r_x}\left(\frac{r_e}{r_x}q_0\, Z^x + H_0\, H_{pc}\, f\Big(Z_3(r_x,t), K^h\Big)\right) \qquad \text{for } t \in (0,\infty) \ , \\ Z^x\Big|_{t=0} &= Z_0^x \ . \end{aligned}$$

Note again that $q_0 < 0$ while $H_0 H_{pc} f(Z_3(r_x,t), K^h) \geq 0$, so that this equation has a non-trivial positive steady state solution

$$\overline{Z}^x = -\frac{r_x}{r_e}\frac{H_0\, H_{pc}}{q_0}\, f\Big(\overline{Z}_3(r_x), K^h\Big) \ .$$

6.2.3 Water flow

As described above, zinc is carried along the water flow path with the velocity of the water (advection). This process influences the distribution of zinc and determines how fast variations in external zinc concentration spread in the system. To avoid a complete treatment of water fluxes in root tissues, we focus only on mass conservation delivering the radial flow speed by considering the effective flow cross section. Variation of cross section in the symplast is included by the volume fraction shown in the bottom graph of Fig. 6.3 and explained in Sec. 6.2.1. Water fluxes in the apoplast were assumed to be small and were neglected, although the apoplast is believed to contribute to the total flux (Steudle, 2000). Hence, water exchange was assumed to occur only at the interfaces between medium and epidermis (especially root hairs) and between pericycle and xylem. Epidermal cells were assumed to take up water from the medium with a given constant flux velocity q_0. The value of q_0 was varied to simulate different transpiration rates. This approach is very simplistic. More sophisticated water flux models have been proposed by other authors, for example Katou and Furumoto (1986); Katou et al. (1987); Taura et al. (1988); Katou and Taura (1989); Murphy (2000); Chavarría-Krauser and Ptashnyk (2013). These models, however, do not couple water flow to regulation of membrane transporters.

Mass conservation for an incompressible fluid in the symplast reads

$$\operatorname{div}(\Phi \mathbf{v}) = 0 \qquad \text{in } \Omega_3 \ , \tag{6.11}$$

where again Φ is the volume fraction and $\mathbf{v}$ is the vector field of flow velocity. Eq. (6.11) can be expressed in cylindrical coordinates to reflect the geometry of the roots by

$$\frac{1}{r}\partial_r(r\,\Phi\, v_r) + \frac{1}{r}\partial_\varphi(\Phi\, v_\varphi) + \partial_z(\Phi\, v_z) = 0 \ . \tag{6.12}$$

where v_r, v_φ, and v_z denote the radial, azimuthal, and axial component of the velocity $\mathbf{v}$. To the end of reducing the model to 1-D we consider the surfaces $\Gamma_i(r)$ as given in (6.3). We introduce the averaged radial velocity in the symplast Ω_3

$$v(r) := \frac{1}{\mu_3\,(r)} \int_{\Gamma_3(r)} v_r(r,\varphi,z)\,\mathrm{d}\gamma\ , \qquad \text{for } r \in [r_x, r_e]\ ,$$

and consider the corresponding average of Eq. (6.12) over $\Gamma_3\,(r)$:

$$\frac{1}{\mu_3(r)} \int_{\Gamma_3(r)} \frac{1}{r}\partial_r(r\,\Phi\,v_r)\,\mathrm{d}\gamma = -\frac{1}{\mu_3(r)} \int_{\Gamma_3(r)} \Big(\frac{1}{r}\partial_\varphi(\Phi\,v_\varphi) + \partial_z(\Phi\,v_z)\Big)\,\mathrm{d}\gamma\ ,$$

where the second and third terms in Eq. (6.12) were moved to the right hand side. With the surface element $\mathrm{d}\gamma = r\,\mathrm{d}\varphi\,\mathrm{d}z$ the left hand side of the equation is

$$\frac{1}{\mu_3(r)} \int_{\Gamma_3(r)} \frac{1}{r}\partial_r(r\,\Phi\,v_r)\,\mathrm{d}\gamma = \frac{1}{r}\partial_r(r\,\Phi\,v)\ ,$$

while the terms on the right hand side correspond to a two dimensional divergence and can be transformed into an integral over the boundary $\partial\Gamma_i(r)$. This boundary integral is zero, based on the assumption that the apoplast and symplast do not exchange water (consequence of assuming no water fluxes in the apoplast). We obtain an equation for the average flow velocity in the symplast

$$\partial_r(r\,\Phi\,v) = 0 \qquad \text{for } r_x < r < r_e\ , \tag{6.13}$$

$$\Phi v\Big|_{r=r_e} = q_0\ , \tag{6.14}$$

where the water influx q_0 was prescribed on the root surface ($r = r_e$). This system can be solved by integration rendering

$$v(r) = \frac{r_e}{r}\frac{q_0}{\Phi(r)} \qquad \text{for } r_x \le r \le r_e\ . \tag{6.15}$$

The top graph in Fig. 6.3 shows the flow velocity obtained from the above derivation and used in the sequel. It shows clearly how the cylindrical geometry of the root results in a general increase of velocity towards the stele. Note that the flow profile can be computed independently from the zinc concentration, because the overall zinc concentration is very small and has practically no effect on the water potential.

6.2.4 Membrane transport

In addition to diffusion and advection, zinc fluxes through the membrane have to be considered (ZIP and HMA4 transporters). Namely, the zinc sources Q_i on the right hand side of Eq. (6.6) depend on the flux densities J_j, which still need to be specified. The zinc flux through transporters T (influx via ZIP) and H (efflux via HMA4) can be modelled by a saturable pointwise reaction mechanism

$$\begin{aligned} &Z_i + T \rightleftharpoons Z\!-\!T \rightarrow Z_3 + T \ , \qquad \text{for } i = 1, 2 \ , \\ &Z_3 + H \rightleftharpoons Z\!-\!H \rightarrow Z_i + H \ . \end{aligned}$$

We will assume that the above reactions follow Michaelis-Menten kinetics as in Chapter 4 with a saturation function

$$f(Z, K) = \frac{Z}{Z + K} \ , \tag{6.16}$$

where K is the corresponding Michaelis-Menten constant.

Regulation of ZIP has been discussed in detail in the previous Chapter 4, where we found an activator-inhibitor model with dimerisation to present a likely mechanism. This model along with the fitted parameters was used here to describe the amount of ZIP transporters for each cell type shown in Fig. 6.1 besides the pericycle. Although this regulatory mechanism was developed as an average description over the whole root, it is more realistic to assume individual gene expression and transporter production in each single cell:

$$\begin{aligned} \frac{dG_\alpha}{dt} &= \gamma_G \Big(K\, A_\alpha^2\, (1 - G_\alpha) - G_\alpha \Big) \ , \\ \frac{dM_\alpha}{dt} &= \gamma_M \,(G_\alpha - M_\alpha) \ , \\ \frac{dT_\alpha}{dt} &= \gamma_T \,(M_\alpha - T_\alpha) \ , \\ \frac{dA_\alpha}{dt} &= \gamma_A \Big(1 - \Gamma\, A_\alpha\, I_\alpha - A_\alpha \Big) \ , \\ \frac{dI_\alpha}{dt} &= \gamma_I \Big(\Gamma_I\, \zeta_\alpha - \Gamma'\, A_\alpha\, I_\alpha - (1 + \Gamma_I\, \zeta_\alpha)\, I_\alpha \Big) \ , \\ &\text{for } t \in (0, \infty),\ \alpha = en, co, ep \ , \end{aligned} \tag{6.17}$$

where G_α is the gene expression level, M_α the transcript level, T_α the transporter level, A_α an activator and I_α an inhibitor, and ζ_α the internal zinc concentration.

The coupling between ZIP regulation and the transport model (6.6) deserves a few considerations. First, zinc is not homogeneously distributed within each cell and it is unclear where and how the cell actually senses the concentration. Here, we assumed that a cell senses its average cytoplasmic concentration given by

$$\zeta_\alpha(t) = \zeta_0^{-1} \frac{1}{\mu(C_\alpha)} \int_{C_\alpha} \mathcal{Z}(x,t)\, dx \qquad \text{for } t \in [0,\infty),\ \alpha = en, co, ep\ ,$$

where ζ_0^{-1} is a scaling factor (ζ_α is non-dimensionalized), integration is over the cell $C_\alpha \subset \Omega_3$ and $\mu(C_\alpha)$ is its volume.

Depending on this sensed concentration, each cell adjusts its own expression level and the resulting amount of transporters independently of the other cells. The transporter proteins regulated by Eq. (6.17) are assumed to be confined to the cell they are produced in and evenly distributed on the plasmamembrane ∂C_α of each single cell. This assumption is supported by the HMA2 expression pattern found in A. thaliana (Sinclair et al., 2007, Fig. 1c). In mathematical terms, the distribution of transporters in the tissue is constructed as follows

$$\mathcal{T}(x,t) = \sum_{\alpha=en}^{ep} T_\alpha(t)\, \chi_{\partial C_\alpha}(x)\ , \qquad \text{for } (x,t) \in \overline{\Omega}_3 \times [0,\infty) \tag{6.18}$$

with the characteristic function

$$\chi_{\partial C_\alpha}(x) = \begin{cases} 1 & \text{if } x \in \partial C_\alpha\ , \\ 0 & \text{if } x \notin \partial C_\alpha\ . \end{cases}$$

HMA4 efflux transporters at the pericycle are included in a similar manner

$$\mathcal{H}(x) = H_{pc}\, \chi_{\partial C_{pc}}(x)\ , \qquad x \in \overline{\Omega}_3\ , \tag{6.19}$$

where the assumption that the level H_{pc} of HMA4 is constant was used (Talke et al., 2006).

Finally, we introduce versions of $\mathcal{T}(x,t)$ and $\mathcal{H}(x)$ which depend on the radius by averaging over $\partial\Gamma_3(r)$

$$\begin{aligned} T(r,t) &:= \frac{1}{\mu\big(\partial\Gamma_3(r)\big)} \int_{\partial\Gamma_3(r)} \mathcal{T}(x,t)\, \mathrm{d}s\ , \quad && \text{for } (r,t) \in [r_x, r_e] \times [0,\infty)\ , \\ H(r) &:= \frac{1}{\mu\big(\partial\Gamma_3(r)\big)} \int_{\partial\Gamma_3(r)} \mathcal{H}(x)\, \mathrm{d}s\ , \quad && \text{for } r \in [r_x, r_e]\ . \end{aligned}$$

Influx was assumed to take place on the surfaces of epidermis, cortex and endodermis cells, while efflux was assumed to take place only at pericycle

Table 6.2: List of parameters used in simulations of the zinc transport model.

Parameter	Value	Description
q_0	$0.1 - 4\,\mu$m/s	Water flux velocity at root surface r_e
D	$500\,\mu\text{m}^2$/s	Diffusivity of zinc in cytoplasm
r_x	$6\,\mu$m	Stele radius (without pericycle)
r_c	$12.5\,\mu$m	Position of Casparian strip
r_e	$40\,\mu$m	Root radius
$z_{0,1}$	$0.5\,\mu$m	Thickness of cell wall
$z_{0,3}$	$135\,\mu$m	Height of cells in cell line
$\varphi_{0,3}$	$\pi/10$	Width (azimuth angle) of cells in cell line
ζ_0	$166.67\,\mu$M	Scaling factor for dimensionalization of internal zinc concentration
T_0	$500\,\mu\text{M}/(\mu\text{m}^2\text{s})$	Maximal amount of ZIP
H_0	$5\,\mu\text{M}/(\mu\text{m}^2\text{s})$	Wild type amount of HMA4
K^h	$1\,\mu$M	Michaelis-Menten constant for HMA4
τ	$0.01 - 1$	Scaling factor for regulatory time scale

cells. Therefore, $T(r,t)$ is equal to $T_{en}(t)$, $T_{co}(t)$ and $T_{ep}(t)$, respectively, for an r inside one of these cells, zero elsewhere. $H(r)$ is equal to H_{pc} for an r inside the pericycle and zero elsewhere. The reaction probability depends on $\Psi T(r,t)$ instead of only $T(r,t)$, because Ω_1 and Ω_2 are porous media and only the reduced amount $\Psi T(r,t)$ has actually contact to Z_1 and Z_2. No correction is needed for $H(r)$, as the cytoplasm can be assumed to have direct contact with the membrane, so that the complete $H(r)$ can react with Z_3.

In total, the flux densities J_j are modelled as

$$J_j(r,t) = \Psi\, T_0\, T(r,t)\, f\Big(Z_j(r,t), K^t\Big) - H_0\, H(r)\, f\Big(Z_3(r,t), K^h\Big)\ , \quad j = 1, 2\ ,$$

where T_0 and H_0 are constants that characterize the true amount of transporters (non-dimensionalized regulation).

6.2.5 Parameters

The diffusivity of zinc ions in water has been measured by Harned and Hudson (1951) to be 700 $\mu m^2/s$. Values of 530 $\mu m^2/s$ have been found for calcium in the axoplasm of *Myxicola* (Donahue and Abercrombie, 1987). Based on these values we assumed an approximate diffusivity of $D = 500\,\mu m^2/s$ for zinc in the symplast. This value does not consider the diffusion of chelated zinc, which could be several times slower. Diffusion in the cell wall has been measured to be fifteen times slower than in the cytoplasm (Kramer et al., 2007). The reduction in diffusivity was accounted for in the model by inclusion of a volume fraction Ψ of 1/15 as in Eq. (6.6). The order of magnitude of the surface water flux velocity q_0 was estimated based on data from Rosene (1943) for water fluxes through root hair cells and data from Zarebanadkouki et al. (2012) for *Lupinus albus* roots. To obtain similar steady state patterns as observed in fluorescence images of zinc distributions in roots (Sinclair et al., 2007; Hanikenne et al., 2008) q_0 was then manually adjusted within this range to values between 1 and $4\,\mu m/s$. The other unknown parameters H_0 and T_0 were also manually adjusted to qualitatively reproduce those data. The steady state parameters of the regulation model are presented in Chapter 4. Sizes of cells and tissue layers were estimated from Hanikenne et al. (2008) with $r_e = 40\,\mu\text{m}$, $r_c = 12.5\,\mu\text{m}$, and $r_x = 6\,\mu\text{m}$. All model parameters are listed in Table 6.2 and the cell sizes used are listed in Table 6.1.

6.2.6 Numerical methods

Time simulations of PDEs require more involved numerical methods than ODEs. We implemented a conservative (i.e. mass-preserving) finite difference method on an equidistant grid in C^{++} and applied it to solve the system of partial differential equations (6.6) in one space dimension. Operator splitting was used to employ different stable explicit finite difference schemes to the advective (hyperbolic) and the diffusive (parabolic) contributions.

Namely, we applied a second-order MacCormack method for the advection term. Given a one-dimensional hyperbolic equation of the form

$$\partial_t \rho + \partial_x(\rho q) = 0 \ ,$$

the MacCormack method calculates the density ρ_i^{n+1} at space point x_i and time t_{n+1} by a two-step formula

$$\begin{aligned} \rho_i^* &= \rho_i^n - \Delta t \left(\frac{\rho_{i+1}^n q_{i+1} - \rho_i^n q_i}{\Delta x} \right) \\ \rho_i^{n+1} &= \frac{1}{2} \left(\rho_i^n + \rho_i^* - \Delta t \left(\frac{\rho_i^* q_i - \rho_{i-1}^* q_{i-1}}{\Delta x} \right) \right) \ , \end{aligned}$$

where ρ^* is a provisional value of ρ and $q_i = q(x_i)$ (Oran and Boris, 2001). For our system (6.6) ρ is given by $\Psi r Z_i$, $i = 1, 2$, in the apoplast and $\Phi r Z_3$ in the symplast, while the advection factor q is given by D/r in the apoplast and $v + D/r$ in the symplast.

A first-order FTCS (forward time centred space) scheme was used for the diffusion and reaction terms. It combines a forward Euler step in time with a central difference scheme in space. For a purely diffusive equation

$$\partial_t \rho - \partial_x (D \partial_x \rho) = 0$$

the density ρ_i^{n+t} as above is calculated by

$$\rho_i^{n+1} = \rho_i^n + \frac{\Delta t}{\Delta x^2} \left(D_{i+1} u_{i+1}^n - 2 D_i u_i^n + D_{i-1} u_{i-1}^n \right)$$

where $D_i = D(x_i)$.

The boundary conditions were implemented with upwinding. To guarantee mass conservation, the boundary flux was corrected for the numerical diffusion of the scheme. The ODEs of the regulation model Eq. (6.17) were solved by an explicit Euler method.

Using explicit schemes for the advective, diffusive and reactive parts allowed us to couple the solvers without much effort. A scheme of this coupling is given in Fig. 6.4. Initial conditions were obtained by calculating the steady state for a given set of parameters by Newton's method. Then, one parameter (Z^e or q_0) was changed to simulate the dynamical adaptation of the tissue. In each time step, first the average internal zinc concentration was computed separately for the three outer cell layers (epidermis, cortex, endodermis). Then, this internal zinc concentration ζ_α, $\alpha = en, co, ep$ was used to calculate the change in regulation by the system (6.17) with one Euler step and obtain the new amounts of ZIP transporter proteins T_α, $\alpha = en, co, ep$. With these amounts set into the flux densities J, Eqs. (6.6) can be advanced by the time step Δt with the MacCormack and FTCS methods as described above. The updated zinc concentrations are then used to start the next time step, until the defined end time T_{max} is reached.

Steady states of the combined system Eqs. (6.6) and (6.17) were calculated with Newton's method using numerical derivatives. Average gradients from spatial data were obtained by linear regression.

6.3 Results and Discussion

6.3.1 Steady state

Figure 6.5 shows the simulated steady state patterns of ZIP levels (boxes), and the zinc concentrations in the symplast (solid line) and apoplast (dashed line) for roots grown in media with high ($Z^e = 25\,\mu$M) and low zinc ($Z^e = 1\,\mu$M). Fluorescence imaging data (Sinclair et al., 2007; Hanikenne et al., 2008) show

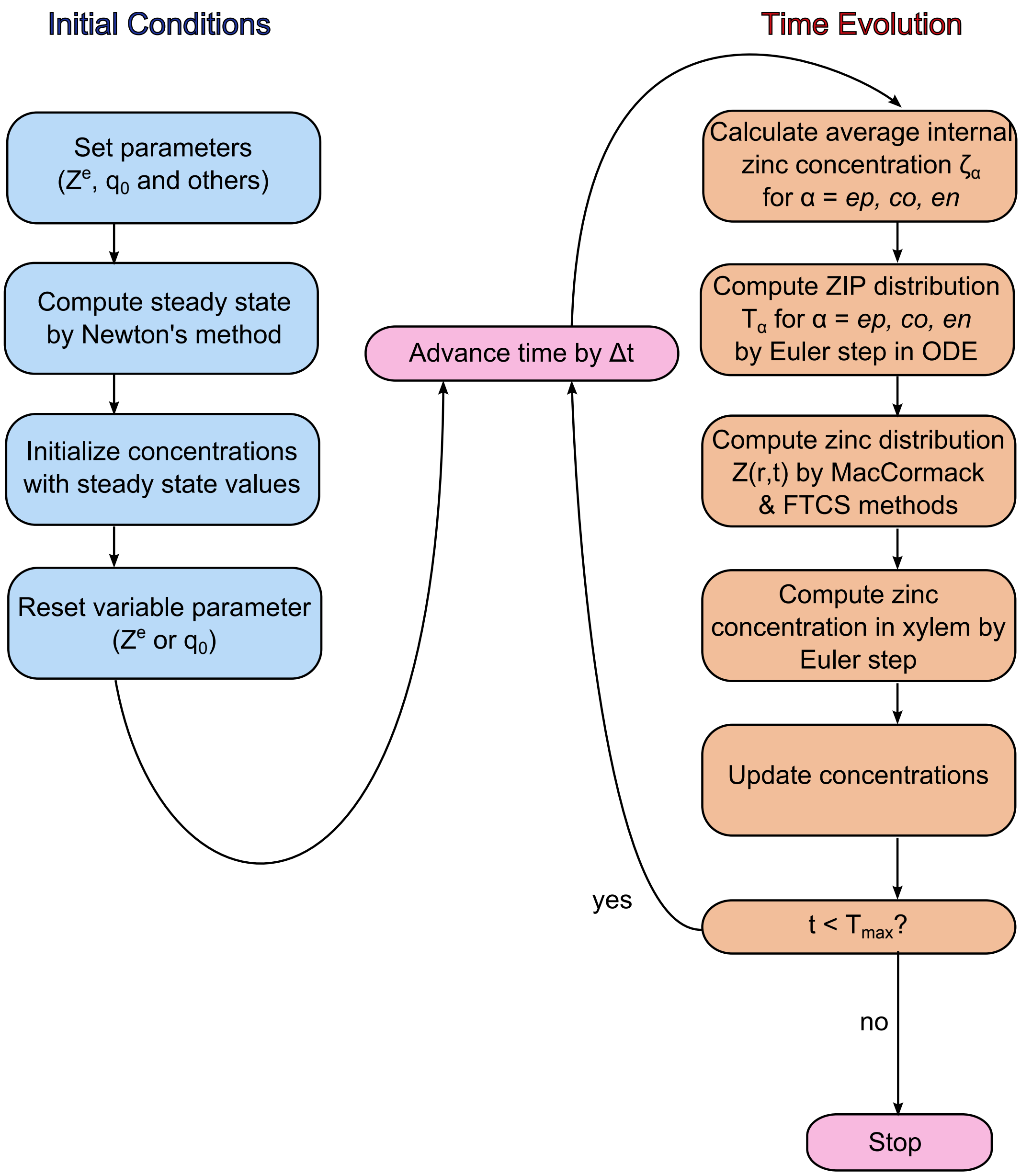

Figure 6.4: Scheme of the numerical methods for dynamic simulations of adaptation to sudden changes in external conditions (Z^e or q_0). Setting of initial conditions is shown in blue (left), time evolution steps are shown in red (right).

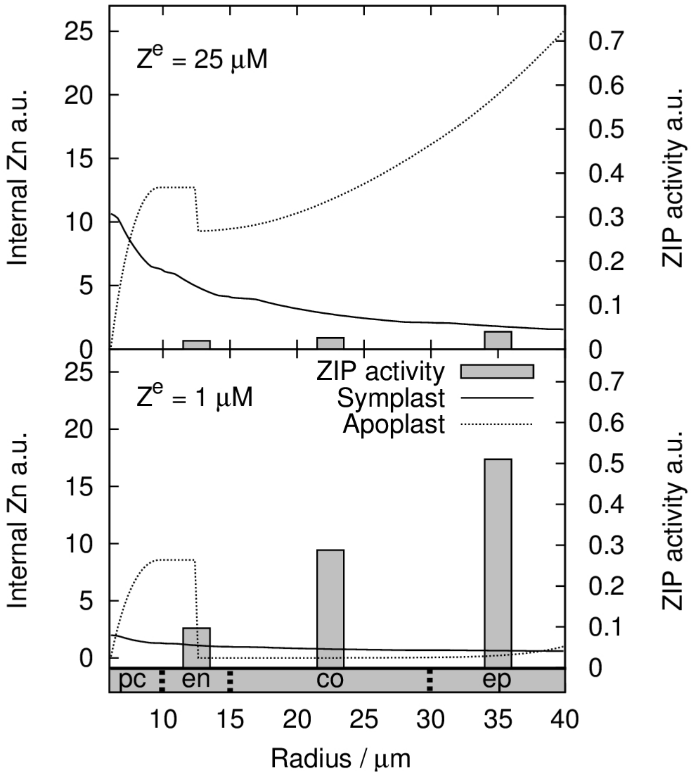

Figure 6.5: Spatial steady state distribution of zinc in wild type. Symplastic (solid line) and apoplastic (dotted line) zinc concentration for high (25 μM; top) and low (1 μM; bottom) medium concentration. Grey boxes illustrate the ZIP activity in epidermis (ep), cortex (co) and endodermis (en).

higher zinc concentrations in the apoplast than in the symplast. A similar distribution is seen in our simulations, although the accumulation in the apoplast may not appear as prominent as in the fluorescence images. This may be due to the fact that zinc and other cations can bind to components of the cell wall and accumulate in the apoplast (Sattelmacher, 2001), which is not considered in our model. Also, the fluorophore Zinpyr-1 used by Sinclair et al. (2007) and Hanikenne et al. (2008) reflects only levels of non-chelated zinc (Sinclair et al., 2007). Considering, in addition, that the vacuole contributes up to 90% of the cell volume, the fluorescence images reflect rather the concentration in the vacuole. All these points could result in underestimating the symplastic zinc concentration in measurements.

In the experimental measurements, no visible gradient was detected in the apoplast. However, in the simulations, under both high and low zinc conditions (see dotted lines in Fig. 6.5), the apoplastic zinc concentration decreases from the epidermis towards the Casparian strip. This is a consequence of zinc being pumped from the apoplast into the symplast by ZIP. In the pericycle, behind the Casparian strip, the apoplastic concentration rises again, as HMA4 mediates zinc efflux from the symplasm. The apoplastic concentration inside the stele is smaller for low external zinc. However, it is still about 60% of the concentration at high zinc, although the external concentration is 25 times smaller. The concentration in the xylem is very low in both cases, because inflowing water dilutes the solution strongly.

Regarding the symplastic concentration, a radial concentration gradient with accumulation in the pericycle has been found in experiments (Sinclair et al., 2007; Hanikenne et al., 2008). This pattern was reproduced very well by the model under certain conditions (see solid lines in Fig. 6.5). We found that for existence of the pattern the contributions of influx, efflux, diffusion and advection have to be properly balanced. Here, influx into the symplast (parameter T_0; Table 6.2) needed to be about 100 times higher than efflux into the apoplast (parameter H_0; Table 6.2) to sustain the pattern in equilibrium. Although the absolute value of H_0 and T_0 are more or less arbitrary, their ratio should give a good estimate for a real root. Much less HMA4 than ZIPs was needed to obtain the pattern, which could explain why roots express so many different ZIPs compared to HMAs. Higher influx or higher efflux produced retrograde gradients, when advection was not increased correspondingly. This result is surprising in the sense that the pattern can be expected to vary in the course of the day, since advection varies in roots as a consequence of changes in transpiration rates. Diffusion is by its nature an equilibrating process, which seeks to even out any concentration gradient. Hence, a large diffusivity compared to advection would destroy the pattern.

The two crucial points for the creation of the pattern are water flow and

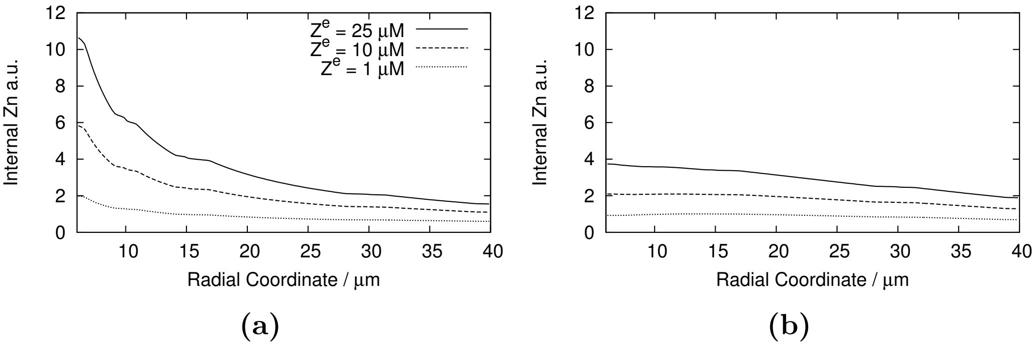

(a) **(b)**

Figure 6.6: Effect of different external zinc concentrations (25 μM, solid line; 10 μM, dashed line; 1 μM, dotted line) on the symplastic zinc gradient. (a) Steady states of symplastic zinc distribution with increasing flow velocity towards the root center (cf. Fig. 6.3). Even at lower external zinc levels, a gradient towards the stele can be seen. (b) Steady states of symplastic zinc concentration with constant flow velocity $q_0 = 4\,\mu$m/s. The gradient is less pronounced at $Z^e = 25\,\mu$M and disappears at lower external concentrations.

geometry. First, the radially oriented advection produced by water uptake is the only process that is physically able to create accumulation at the pericycle. It links the spatially separated influx and efflux cells. Although these are also linked by diffusion, accumulation cannot be explained by that process. The importance of the velocity of water influx will be discussed below in more detail. Second, the cylindrical geometry is beneficial to creation of the pattern, because the volume contracts for smaller radii. On the one hand, this accelerates water on its path to the xylem, helping to create a larger accumulation in the pericycle. On the other hand, the concentration increases faster at small radii for the same flux, because there is less solvent volume. Without the geometrical effects, the pattern was far less pronounced (Fig. 6.6b). The influx velocity of water, q_0, needed to be larger than 1 μm/s to produce a sufficient gradient (Fig. 6.7 bottom). Zarebanadkouki et al. (2012) measured velocities of approximately 0.2 μm/s in *Lupinus albus* during the day. The measured values are lower than the values used here, but these are for lateral roots of *L. albus* with a diameter substantially larger than the primary root of *A. thaliana*. Measurement of the flux velocity in *A. thaliana* roots and an extension of the water flow model would be necessary to be able to draw more precise conclusions.

Regarding the patterns of ZIP expression, our model predicts that ZIP activity follows conversely the pattern of symplastic concentration (see grey bars in Fig. 6.5). The gradient in expression is particularly clear for low zinc

($Z^e = 1\,\mu$M), where the epidermis is predicted to have an expression level that is five times higher than in the endodermis. In Chapter 4 we showed that the regulation mechanism proposed is particularly robust for certain internal concentrations (Fig. 4.5). Gene expression can vary substantially without affecting much the internal zinc concentration in this “robust” range. Our model suggests that a high dynamic range in expression level, i.e. high and low expression in the epidermis and endodermis, respectively, can be expected near $1\,\mu$M external zinc concentration. This is the external concentration at which an experimental validation of the expression pattern should be conducted to obtain the best results. Measurements of Birnbaum et al. (2003) are not in concord with our results. Using growth medium with $30\,\mu$M external zinc, these authors found the expression levels of ZIP2 and ZIP4 to be minimal in the cortex and similarly high in the epidermis and endodermis. The measurements of Birnbaum et al. (2003) are surprising in the sense that they are not in line with the well documented symplastic gradient. Their results suggest that concentration of zinc is maximal in the cortex cells, where expression was found to be lowest. Neither our model nor the fluorescence images of Sinclair et al. (2007) and Hanikenne et al. (2008) support this. As mentioned above, an experimental validation of the expression patterns should be conducted at an external concentration for which a high dynamic range in expression is expected. At $30\,\mu$M external zinc, where Birnbaum et al. (2003) conducted their measurements, expression can be expected to be very low in general and the dynamic range per se small (cf. Fig. reffig:fig4 top). Small gradients in expression level are probably insignificant compared to the uncertainty of the measurement at that high concentration. Future experiments are needed to verify the gradient in ZIP activity predicted by the model.

6.3.2 Variation of HMA4 and water influx velocity

The level of HMA4 has been increased in experiments by introducing an *HMA4* gene of the zinc hyperaccumulator *A. halleri* into roots of *A. thaliana* (Hanikenne et al., 2008). The *AhHMA4* gene has been found to contain multiple copies of *HMA4*, which leads to higher expression and more efficient transport of zinc into the xylem (Hanikenne et al., 2008). As a result, fluorescence images showed a change in the distribution of zinc in the tissue such that accumulation in the pericycle and the radial gradient were lost. To model such *A. thaliana* mutants with enhanced expression of *HMA4*, simulations were performed with higher levels of HMA4 transporters (via parameter H_0; Table 6.2). As a reference value for the wild type we use $H_0 = 5\,\frac{\mu\mathrm{M}}{\mu\mathrm{m}^2\mathrm{s}}$. Fig. 6.7 presents in the upper panel the symplastic concentration distribution for different HMA4 levels. Increasing HMA4 to two (dashed line) or three times

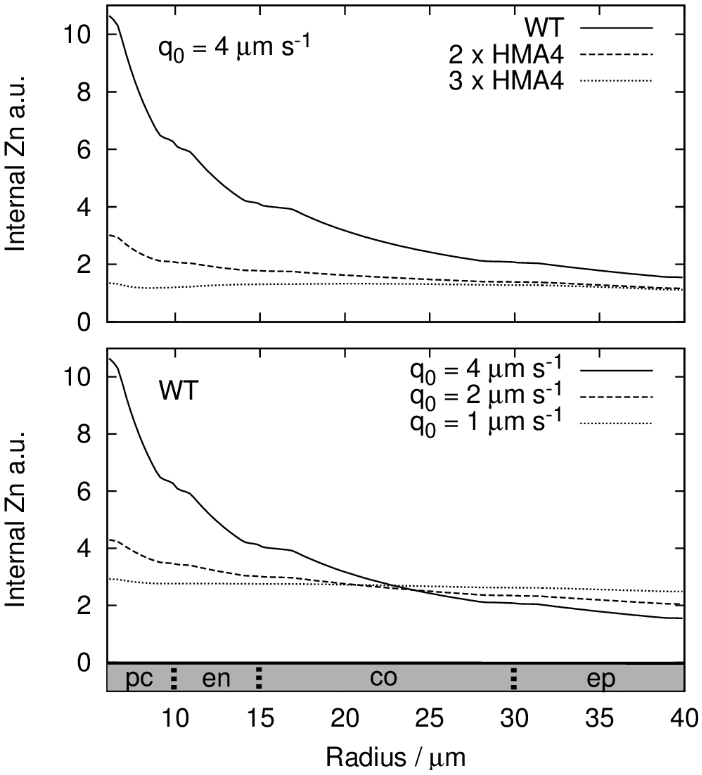

Figure 6.7: Variation of HMA4 and flow velocity. Symplastic zinc concentrations are shown along the radial coordinate in epidermis (ep), cortex (co), endodermis (en) and pericycle (pc) cells. Top: HMA4 levels were increased from the wild type level (WT, solid line) by a factor two (dashed line) or three (dotted line) at a constant flow velocity $q_0 = 4\,\mu$m/s. Bottom: Flow velocity q_0 was decreased from $4\,\mu$m/s (solid line) to $2\,\mu$m/s (dashed line) and $1\,\mu$m/s (dotted line) with constant HMA4 at WT level.

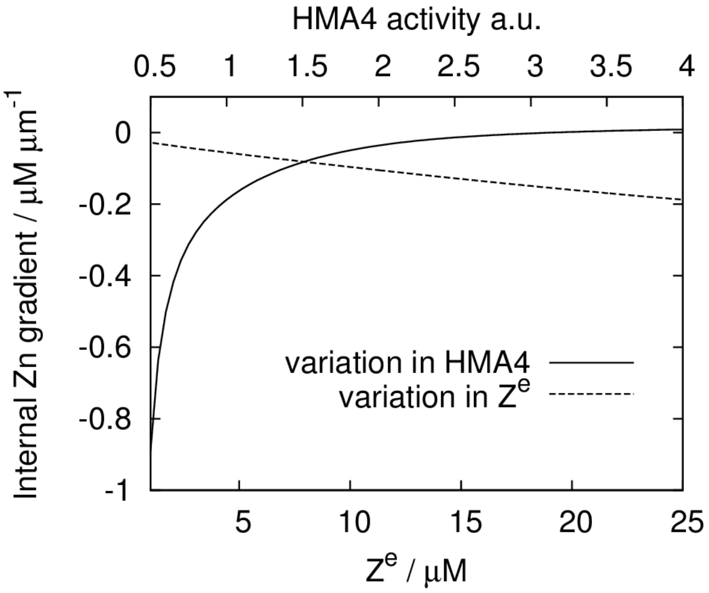

Figure 6.8: Average symplastic zinc gradient is shown as a function of HMA4 (in multiples of the wild type level, solid line) and of the external zinc concentration Z^e (dashed line). Negative numbers reflect a gradient oriented towards the stele.

(dotted line) of the original level (solid line) leads to a decrease of the overall zinc concentration and loss of the gradient.

The contrary effect has been observed in hma2, hma4 double knockout mutants of *A. thaliana* (Sinclair et al., 2007) and in *A. halleri* with reduced expression of *AhHMA4* (Hanikenne et al., 2008). The model describes this situation also very well (Fig. 6.8) and predicts a high sensitivity to variations in HMA4 in this regime. Talke et al. (2006) showed that HMA4 expression in *A. thaliana* and *A. halleri* roots varies substantially less in resupply and oversupply experiments than the one of ZIP genes. They used this fact to propose that its expression does not depend much on the zinc status. In view that our model predicts a regime of large sensitivity, HMA4 might actually also be subjected to regulation and only small adaptation of expression might be enough to create sufficient effect. This would explain why HMA4 expression varies much less.

Surprisingly, decreasing the influx velocity of water (parameter q_0; Table 6.2) had a very similar effect as increasing HMA4. Simulations with half (dashed line) or one fourth (dotted line) of the original velocity (see Fig. 6.7, lower panel) show a loss of symplastic zinc gradient similar to the one seen with increasing HMA4. The overall zinc concentration, however, remains higher than in the variation of HMA4, with even slightly higher values in the epidermis than for the original velocity ($q_0 = 4\,\mu$m/s). While an increase in HMA4 caused enhanced efflux of zinc into the xylem and thereby an increase in the total outflux from the symplastic domain, a decrease in velocity only changed the distribution of zinc in the tissue. Instead of accumulating zinc in the pericycle, diffusion took overhand and produced an almost homogeneous distribution. Very low water fluxes and very high HMA4 levels produce even a retrograde gradient with higher zinc concentrations in the epidermis than in the pericycle, as can be seen in Fig. 6.8 (postive gradient for high HMA4) and in the first panel in Fig. 6.10.

These results can be of major importance for future measurements, since plants change their respiration rates depending on the time of day, light, humidity, etc. and thus, the flow velocity of water in roots is highly variable. Adaptation to a new transpiration rate is even predicted to take place within less than a minute (Fig. 6.10). No published experimental data examining the relation between transpiration rate and solute localization in roots is known to the author. If the equilibration times predicted by the model prove to be realistic, experiments will have to be designed and conducted with much care to avoid artefacts–just moving the plant into dark to conduct the measurement might change the pattern.

To further investigate the relation between HMA4 level and symplastic gradient, the correlation between steady state average gradient and HMA4 activity is analysed. The average gradient was calculated by linear regression as the slope of a fitted linear function. In the case of an accumulation in the pericycle the result is a negative number, reflecting the fact that the gradient points inwards, i.e. concentrations increase towards the xylem. The absolute value of this gradient gives a measure of the “steepness” of the concentration profile. Fig. 6.8 shows the dependence of the average gradient on the normalized HMA4 activity (solid line) as a strongly non-linear response. Raising HMA4 leads to a decrease in the absolute value of the gradient. For HMA4 levels larger than three times the wild type level, the gradient becomes even retrograde (change in sign). At less than half the wild type value, a singularity/pole is found. The gradient becomes very steep when approaching the pole and no steady state can be sustained beyond. The reason is an imbalance of influx and efflux, leading to more zinc being pumped into the symplast than can flow out into the xylem. Small variation of HMA4 produces a strong reaction near the pole, i.e. zinc accumulation reacts very sensitive to HMA4 activity there.

The gradient also depends on the external zinc concentration. External zinc concentrations are predicted by the model to influence the strength of the

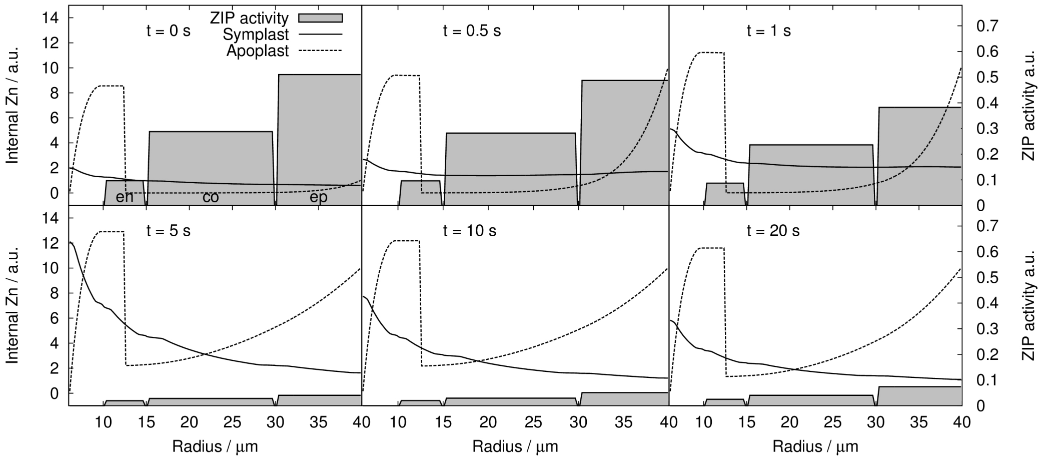

Figure 6.9: Dynamics after a change in the external zinc concentration (resupply experiment). Starting from the steady state distribution of zinc in the symplast (solid line) and apoplast (dashed line) at an external concentration of 1 μM, the medium concentration was changed to a high zinc condition (10 μM). Grey boxes show ZIP activity for epidermis (ep), cortex (co) and endodermis (en) cells. The new steady state is reached at $t = 20\,\text{s}$.

zinc concentration gradient in an almost linear manner (Fig. 6.6a and Fig. 6.8, dashed line), i.e. higher external concentrations lead to higher accumulations of zinc in the pericycle. No experimental quantifications of the concentration gradient for varying concentrations are known to the authors. Sinclair et al. (2007) found an almost linear relation between Zinpyr-1 fluorescence and zinc concentration in the medium, suggesting that the average internal concentration depends linearly on the external concentration. Our model predicts also a roughly linear dependency with a slope of $0.0887 \pm 0.0005\,\mu\text{M}/\mu\text{M}$. Talke et al. (2006) also measured the average zinc concentration in *A. thaliana* and *A. halleri* roots for different external concentration and found a positive correlation. They plotted their data with a logarithmic scale, which does not allow to compare directly the functional relations. However, plotting a linear relationship against a logarithmic scale produces a graph similar to the one published by Talke et al. (2006), suggesting that at least for small concentrations the relationship is roughly linear.

6.3.3 Dynamics

Similar to the resupply experiments by Talke et al. (2006), we simulated the adaptation of the system to a new environmental condition with increased external zinc. Starting from the steady state at low zinc ($Z^e = 1\,\mu$M), the external zinc level was raised to a high zinc condition ($Z^e = 10\,\mu$M). Figure 6.9 presents the evolution of the concentration profiles in time during this adaptation. After increasing the external concentration zinc diffused quickly into the apoplast outside the Casparian strip (in less than 1 s). During this time, regulation kept the high expression level of ZIP, resulting in an overall increase in symplastic concentration and a more pronounced gradient. This led to an increase in apoplastic concentration inside the stele and later to a sudden down-regulation of ZIP. Although the time scale of regulation was assumed to be equal to that of transport (parameter $\tau = 1$; Table 6.2), adaptation of ZIP activity lagged behind, leading to an “overshoot” at about 5 s, where symplastic zinc in the pericycle exceeded its final steady state value by a factor of two. From there on the system stabilized to finally approach the new steady state value after about 20 s. Talke et al. (2006) measured the expression levels every two hours, which is too coarse to resolve the dynamics of adaptation in the root, as suggested by our results and analysed in more detail in Section 6.3.4.

While a sudden change in the external zinc concentration is rather unlikely in a natural environment, changes in the flow velocity happen regularly caused by changes in leaf respiration rates. Transpiration, which defines the velocity of water flow, can vary substantially in the course of the day and is minimal during the night. To understand how adaptation to a change in transpiration rate takes place, we simulated the time evolution upon a sudden change in water influx velocity q_0 from 0.05 to $4\,\mu$m/s (see Figure 6.10). Due to the low water flux, a slightly retrograde concentration gradient was found at 0 s. ZIP expression was also almost constant in space, with a slightly higher expression in the endodermis. After increasing q_0, the concentration gradient built up quickly. An accumulation in the pericylce was clearly visible after 0.2 s and stabilized already after 1 s. This led to a reversal of the distribution of gene expression, with a clear gradient towards the epidermis, where expression stabilized at twice the level of endodermis cells. The apoplastic concentration outside the Casparian strip did not change much during equilibration. In contrast, the apoplastic concentration in the stele decreased to half the initial value as a consequence of the higher water flow rate. Due to the same reason, the concentration in the xylem fell from about $10\,\mu$M for low transpiration to almost $0\,\mu$M for a normal transpiration rate.

Equilibration predicted by our model seems at a first glance to take place

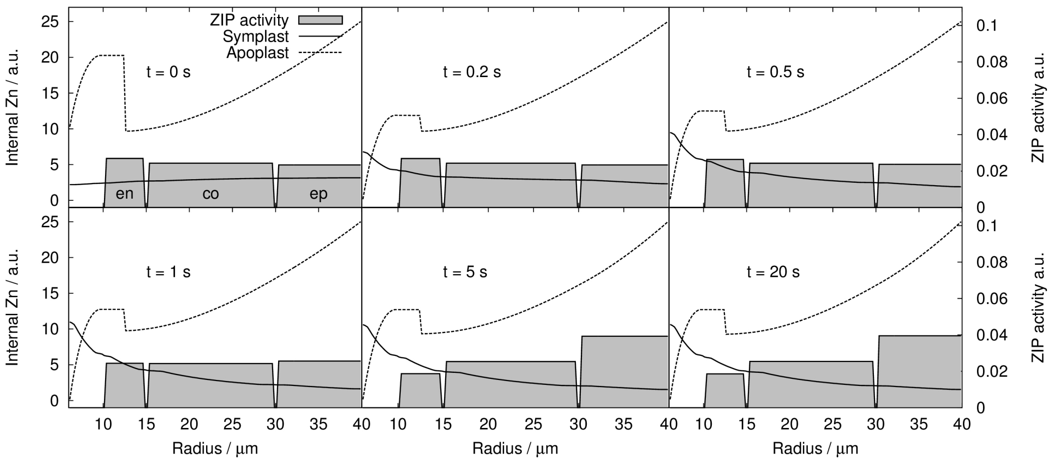

Figure 6.10: Dynamics after a change in flow velocity. Starting from the steady state distribution of zinc in the symplast (solid line) and apoplast (dashed line) at $q_0 = 0.05\,\mu\text{m/s}$, the flow velocity was increased to $q_0 = 4\,\mu\text{m/s}$. Grey boxes show ZIP activity for epidermis (ep), cortex (co) and endodermis (en). A new steady state is reached after 5 s. External zinc was kept constant at $Z^e = 25\,\mu\text{M}$.

very fast (within less than a minute). Due to the lack of data, the time scales of both transport and regulation had to be chosen more or less arbitrarily, which makes this result uncertain. Nevertheless, the following reflection indicates that equilibration within minutes is feasible. The time scale of transport is in principle determined by four parameters beside the diameter of the root (Table 6.2): q_0, D, H_0 and T_0. While q_0, H_0 and T_0 were chosen such that our results correspond qualitatively to the observations of Sinclair et al. (2007) and Hanikenne et al. (2008), the diffusivity D in the cytoplasm was estimated from measurements of free calcium in the axoplasm of *Myxicola* (Donahue and Abercrombie, 1987). That is, D was set while the rest was chosen to match the observations. The time scale can be adapted by multiplying these parameters with the same factor. Therefore, if the diffusion coefficient D would be smaller, q_0, T_0 and H_0 could have been chosen correspondingly smaller obtaining the same spatial pattern but with a slower equilibration. Zinc is known to be chelated in the cytoplasm (Clemens et al., 2002). Depending on the size of the chelator, diffusion coefficients may be an order of magnitude lower. Hence, the time scale of our model would be roughly ten times higher and equilibration would take place in three to four minutes. The time scale of equilibration should be considered with more detail in further experiments. Our model indicates that experiments should be conceived to capture effects that live only a few minutes (cf. Fig. 6.12).

6.3.4 Time scale of regulation

In the numerical experiments described above, the time scale of regulation was set to be comparable to the time scale of transport and diffusion (parameter $\tau = 1$; Table 6.2). The real time scale of regulation is unknown and may indeed be much slower. To understand how the specific choice of τ influences the entire process, simulations with different time scales were performed. Figure 6.11 shows the effect of resupply from low zinc ($Z^e = 1\,\mu$M; upper black square) to high zinc ($Z^e = 10\,\mu$M; lower black square) by plotting: the evolution in time of average ZIP activity and average internal zinc concentration as a phase diagram (Fig. 6.11a), and the average internal concentration against time (Fig. 6.11b). The paths shown in Fig. 6.11a represent the state of the root in time and the arrows mark the direction in which the state moved. The same transition from low to high zinc was conducted for three different time scale factors τ: 1 (red path), 0.1 (blue path) and 0.01 (green path). This means that the time scale of regulation was approximately 6 s for $\tau = 1$, 60 s = 1 min for $\tau = 0.1$ or 10 min for $\tau = 0.01$.

In general, the internal concentration rose strongly after resupply, exceeding the one of the new steady state at high zinc (“overshoot”, Fig. 6.11). The

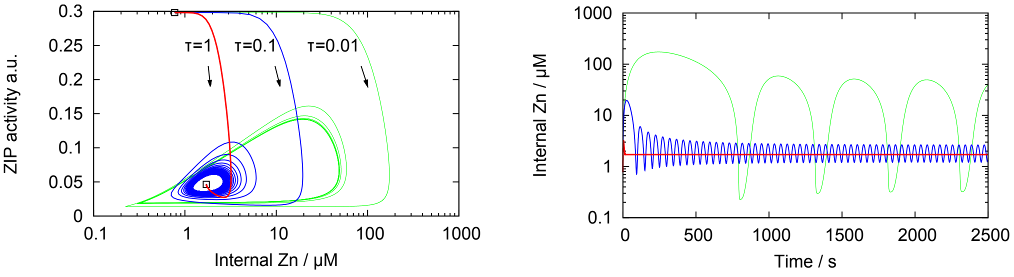

(a) **(b)**

Figure 6.11: Variation of regulation time scale. The time scaling factor τ of the ZIP regulation model was decreased from $\tau = 1$ (red line) to $\tau = 0.1$ (blue line) and $\tau = 0.01$ (green line) and time courses were simulated for a change of the external zinc concentration from 1 μM to 10 μM. (a) the transition between the two steady states (black squares) is shown as a phase diagramm of ZIP activity against symplastic zinc. For $\tau = 1$, the system reaches the new steady state after a minor overshoot. For $\tau = 0.1$ and $\tau = 0.01$, the new steady is unstable and concentrations oscillate on a limit cycle. (b) time course of the symplastic concentration showing clearly the oscillations.

reason was the high ZIP expression level at the initial state (about 30% activity; Fig. 6.11a). Regulation then reacted by shutting down the expression of ZIP (vertical portion of the paths; Fig. 6.11a), overreacting even slightly. For $\tau = 1$ the system eventually approached the new steady state. For slow regulation ($\tau = 0.1$ and 0.01) stable oscillations around the steady state were observed (Fig. 6.11). In those cases the system did not approach the steady state. The reason for the oscillation was the overreaction of regulation producing a strong sudden reduction in concentration (horizontal path; Fig. 6.11a), which led again to an overreaction of upregulation, and to a too large concentration. The amplitude of the oscillation correlated with the time scale of the regulation: slow regulation produced larger oscillations (Fig. 6.11). Similar oscillations emerging from a Hopf bifurcation had also been observed in the ODE regulatory model analyzed in Chapters 4 and 5. There, the appearance of these oscillations depended on the choice of a high value for the parameter Γ. Here, oscillations appear even at low Γ, but depend on the choice of the regulatory time scale.

Experimental validation of these oscillations may be difficult, because a real root lacks a high degree of spontaneous coordination. The model assumes that the root is perfectly coordinated resulting in well defined oscillations. In real roots, the oscillatory behaviour would rather come to light as a high variance in, for example, expression level. Since zinc shocks caused by oscillations can

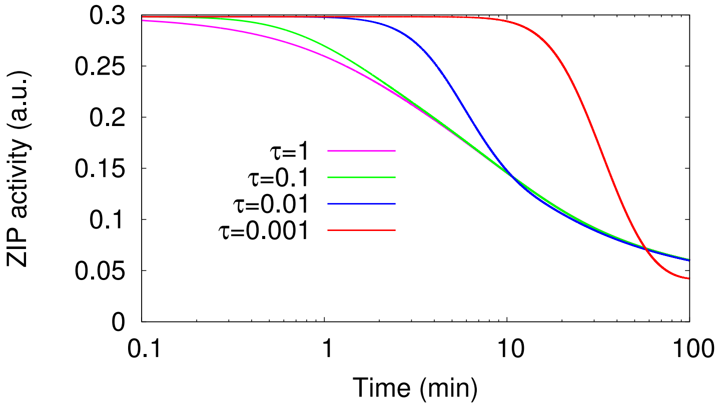

Figure 6.12: Dynamics of ZIP activity under different time scales of regulation. Characteristic time of 6 s ($\tau = 1$, magenta), 1 min ($\tau = 0.1$, green), 10 min ($\tau = 0.01$, blue), and 100 min ($\tau = 0.001$, red) were simulated. The buffering parameters were kept constant at $K_b = 1000$ and a characteristic time of 0.003 s.

be toxic and even deadly to plant cells, regulation either needs to be fast - on the same time scale as transport–or the cells need to have fast and efficient buffering mechanisms.

Zinc is known to be buffered and sequestered into the vacuole (Clemens et al., 2002). To be efficient in damping oscillations, these mechanisms have to be fast and not rely directly on regulation, which calls for a chelation mechanism. Such buffering (see Chapter 7 for details) can slow down the adaptation of the entire root system to external changes and allows slower regulation without oscillations. Nevertheless, Fig. 6.12 shows that even with strong and rapid buffering ($K_b = 1000$ and $\zeta_b = 1$, which corresponds to a characteristic time of 0.003 s, cf. Chapter 7), adaptation of ZIP activity is faster than two hours. Varying the time scale of regulation by a factor of 10^3 leads to no measurable differences in ZIP activity after one hour. To be able to determine a more realistic time scale of ZIP regulation, measurements need to be taken at shorter intervals of preferably less than 10 min.

6.3.5 Conclusions

Our simulations show that water uptake and the associated advection of zinc towards the stele is the main mechanism in formation of the radial zinc pattern in roots. The transpiration rate is therefore expected to influence the pattern strongly and its reduction should produce a similar effect as increasing the expression of *HMA4*. The cylindrical geometry supports the effect of advection.

Zinc accumulation in the pericycle depends nonlinearly on the expression of *HMA4*, where small variations of expression suffice to produce large effects. This might explain why HMA4 seems to be unchanged during resupply experiments. In general, a much smaller activity of HMA4 than of ZIPs is needed to maintain sufficient zinc supply, giving a possible explanation why so many different zinc uptake transporters (ZIP family) are expressed in roots compared to only few zinc release transporters (HMA).

Modelling of resupply experiments shows that regulation must occur within minutes to avoid strong peaks in symplastic concentration. Fast chelating agents seem to be necessary to dampen possible oscillatory behavior and short-term oversupply (see Chapter 7 for details). A slow sequestration possibly based on genetic regulation, e.g. into the vacuole, is less suited to counteract these short-term effects and may be rather important in long-term adaptation.

The model presented here describes the uptake and transport of zinc, but can easily be applied to other nutrients as well. Iron is another essential metal that seems to be mainly transported by IRT1, another member of the ZIP family of transporters (Kim and Guerinot, 2007). The distribution of iron in roots has been studied in a recent paper (Roschzttardtz et al., 2013, Fig. 1) and the results show a distribution pattern with strong accumulation in the apoplast of the pericycle. This pattern resembles the zinc pattern in our model and can most likely be explained by the same mechanisms of cylindrical geometry, water flow and regulated transport.

7 Roles of buffering and sequestration

7.1 Vacuolar sequestration in yeast

The vacuole is a key player in metal sequestration both in plants and in yeast. Zinc transport into the vacuole appears to be regulated in a similar manner as the uptake across the cell membrane. Little is known about the regulation of vacuolar transporters in plant roots, but considerable amounts of data are available for yeast. Therefore, we will again start this chapter with a discussion of the well-known processes in yeast.

7.1.1 Biological background

The vacuole has been shown to play a major role for zinc homeostasis in yeast. It acts in three different main functions: First, the vacuole is able to store zinc under zinc replete conditions for future periods of zinc deficiency. Secondly, the compartment can sequester excessive amounts of zinc from the cytosol for detoxification, and thirdly, it can buffer rapid changes of zinc levels and thus protect the cells under “zinc shocks” (MacDiarmid et al., 2002; Simm et al., 2007).

In the vacuole, zinc is supposedly bound to ligands that mainly contribute to the vacuolar zinc storage capacity. Among these are polyphosphates and organic anions such as glutamate and citrate (Simm et al., 2007). Other cell compartments like the mitochondria or zinc-enriched cytoplasmic vesicles seem not to play an important role in zinc sequestration in yeast (Simm et al., 2007).

Transport of zinc across the vacuolar membrane is driven by transporter proteins. Two transporters, ZRC1 and COT1, have been found to be responsible for transport into the vacuole (MacDiarmid et al., 2003), while a third transporter, ZRT3, seems to transport zinc out of the vacuole into the cytosol (MacDiarmid et al., 2000). While the expression of *COT1* is not responsive to the external zinc concentration, *ZRC1* and *ZRT3* are regulated by zinc. Both genes contain a ZRE (zinc responsive element) in their promoter region, which is activated by ZAP1. This transcription factor is expressed under zinc deficiency and also activates the expression of ZIP transporters ZRT1 and ZRT2 in the outer membrane to pump zinc from the external medium into the cytoplasm. A schematic overview of these processes is given in Fig. 7.1.

7.1.2 Model

The model is based on the model (4.9) on page 31 describing the regulation of zinc uptake transporters. We use the same notations as in Chapter 4: A is the activator ZAP1, G_A its gene activity, M_A the corresponding mRNA, T_1 and T_2 are the uptake transporters ZRT1 and ZRT2 with their gene activities G_1 and G_2 and mRNAs M_1 and M_2, respectively:

$$\begin{aligned}
\frac{dG_A}{dt} &= \gamma_{GA}\Big(K_A\,A\,(1-G_A)-G_A\Big)\\
\frac{dM_A}{dt} &= \gamma_{MA}\,(G_A-M_A)\\
\frac{dA}{dt} &= \gamma_A\,(M_A-A-\Gamma_A\,Z\,A)\\
\frac{dG_1}{dt} &= \gamma_{G1}\Big(K_1\,A\,(1-G_1)-G_1\Big),\\
\frac{dG_2}{dt} &= \gamma_{G2}\Big(K_2\,A\,\Big((1+K_2'\,A)^{-1}-G_2\Big)-G_2\Big)\\
\frac{dM_i}{dt} &= \gamma_{Mi}\,(G_i-M_i), \qquad i=1,2\\
\frac{dT_1}{dt} &= \gamma_{T1}\,(M_1-T_1-\Gamma_{T1}\,T_1\,Z)\\
\frac{dT_2}{dt} &= \gamma_{T2}\,(M_2-T_2)\,.
\end{aligned} \tag{7.1}$$

New equations are needed to describe the vacuolar transporters ZRT3 (T_3) and ZRC1 (T_4) with their respective gene activities G_3 and G_4 and mRNAs M_3 and M_4. We assume *ZRT3*, which pumps zinc from the vacuole into the cytoplasm, to be activated by the activator ZAP1 in the same manner as the membrane transporter *ZRT1* before. Transport from the cytoplasm into the vacuole is achieved by ZRC1, which is also expressed under activation by ZAP1, but has an additional basal zinc-independent activation term. The third transporter, COT1, seems not to be regulated by zinc and transport through it cannot be distinguished from the zinc-independent activity of ZRC1. Therefore, we will

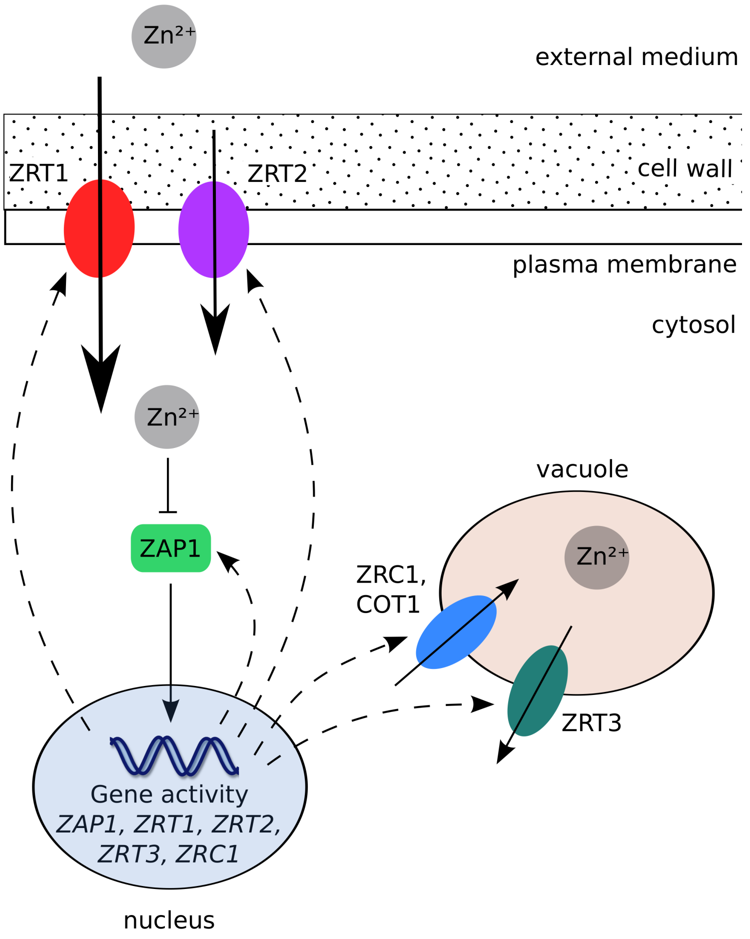

Figure 7.1: Scheme of vacuolar transport in yeast. The activator ZAP1 is inhibited by zinc. It induces gene activity for the membrane transporters ZRT1 and ZRT2 as well as for the vacuolar influx transporter ZRC1 and the efflux transporter ZRT3. Gene transcription into mRNA and translation into protein is combined in the dashed arrows. The influx transporter COT1 is not regulated by zinc.

not model it separately. These considerations lead to the equations

$$\begin{aligned}
\frac{dG_3}{dt} &= \gamma_{G3}\,(K_3\,A\,(1-G_3)-G_3) \\
\frac{dG_4}{dt} &= \gamma_{G4}\,(K_4\,A(1-G_4)+K_4'(1-G_4)-G_4) \\
\frac{dM_i}{dt} &= \gamma_{Mi}\,(G_i-M_i), \qquad i=3,4 \\
\frac{dT_i}{dt} &= \gamma_{Ti}\,(M_i-T_i), \qquad i=3,4\;.
\end{aligned} \tag{7.2}$$

The cellular zinc concentration is now divided into cytosolic zinc Z_{cyt} and vacuolar zinc Z_{vac}. For simplicity, we assume the volumes of cytoplasm and vacuole to be equal, which is roughly the case in average yeast cells. Then, we need no additional volume scaling factors and can use the same γ for cytosolic and vacuolar zinc to obtain

$$\begin{aligned}
\frac{dZ_{\text{cyt}}}{dt} &= \gamma\left(T_1\,f(Z^e,K_1^t)+\kappa\,T_2\,f(Z^e,K_2^t)+\kappa_3\,T_3\,Z_{\text{vac}}-\kappa_4\,T_4\,Z_{\text{cyt}}-Z_{\text{cyt}}\right) \\
\frac{dZ_{\text{vac}}}{dt} &= \gamma\,(-\kappa_3\,T_3\,Z_{\text{vac}}+\kappa_4\,T_4\,Z_{\text{cyt}})\;.
\end{aligned} \tag{7.3}$$

Here, we model transport into the vacuole with simple mass action equations without saturation effects, since preliminary numerical simulations showed no significant difference and zinc affinities of ZRT3 and ZRC1 are unknown.

7.1.3 Results and Discussion

Steady states and dynamic behavior

For the model we used the parameters obtained in Chapter 4 and fitted the new parameters with data from MacDiarmid et al. (2000) and MacDiarmid et al. (2003). These data consist of steady state values for zinc and the transporter proteins (see Fig. 7.2) at various external zinc concentrations and time data of zinc accumulation in conditions referred to as “zinc shock” (Fig. 7.3). Such a stress situation occurs when zinc-deficient cells with a maximal induction of zinc uptake transporters encounter even moderate amounts of external zinc, leading to rapid overaccumulation. While the parameters from Chapter 4 are given in Table 4.1, the new parameters are shown in Table 7.1.

The steady state measurements for ZRT3 in MacDiarmid et al. (2000) and ZRC1 MacDiarmid et al. (2003) were used to fit equilibrium constants K_3, K_4, and K_4'. As shown in Fig. 7.2a, the model can explain the data for the regulation of ZRT3 and ZRC1 very well. They are both regulated

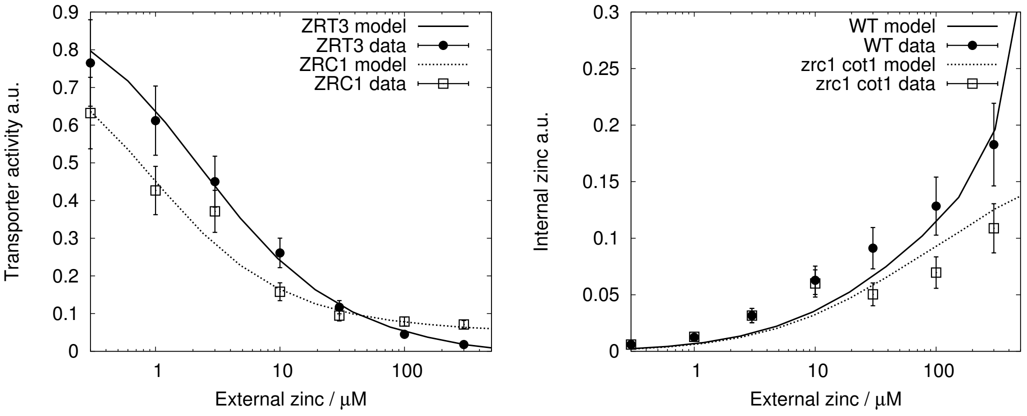

(a) **(b)**

Figure 7.2: Steady states of transporters and zinc for varying external zinc concentration with data points. (a) Model simulation and data for ZRT3 (solid line) and ZRC1 (dotted line) steady states. ZRT3 data is taken from MacDiarmid et al. (2000, Fig. 1A) (black circles), ZRC1 from MacDiarmid et al. (2003, Fig. 2A) (white squares). (b) Model simulation and data for internal zinc steady states in wild type (WT, solid line) and zrc1 cot1 double mutant (dotted line). Data is taken from MacDiarmid et al. (2003, Fig. 3B): WT - black circles and zrc1 cot1 mutant - white squares.

Table 7.1: Parameters used in the yeast vacuole model.

Parameter	Value	Biological meaning
K_3	9.81	Activation of *ZRT3* by ZAP1
K_4	4.23	Activation of *ZRC1* by ZAP1
K'_4	0.06	ZAP1-independent activation of *ZRC1*
κ_3	$4.6 \cdot 10^8$	Transport rate of ZRT3
κ_4	$7 \cdot 10^7$	Transport rate of ZRC1
τ_1	929	Time constant for ZAP1, ZRT1 and ZRT3 regulation
τ_2	0.28	Time constant for ZRT2 regulation
τ_3	0.09	Time constant for ZRC1 regulation
τ_4	0.16	Time constant for zinc transport

by the zinc-dependent activator ZAP1 and therefore highly expressed under zinc deficiency and down-regulated for increasing zinc levels. The vacuolar import transporter ZRC1 shows also ZAP1-independent basal expression at high zinc that is parametrized by K'_4. It is noticeable that the values of K_3 and K_4 that determine the ZAP1-dependent regulation of ZRT3 and ZRC1, respectively, are smaller by one magnitude than the corresponding value K_1 for the membrane transporter ZRT1. Indeed, the values reflect the steeper curve shown in the regulation of the vacuolar transporters (MacDiarmid et al., 2000, cf. Fig. 1A). Compared to the outer membrane transporter ZRT1, they are downregulated already at lower external zinc concentrations.

MacDiarmid et al. (2003) also present steady state measurements of the entire “cell-associated” zinc concentration combining cytosolic and vacuolar zinc in wild type yeast and various mutants. We focused on only one of these mutants, namely the zrc1 cot1 double knockout that can be assumed to have virtually no vacuolar sequestration of zinc. While the wild type data was compared to model simulations with the full model in Eqs. (7.1), (7.2) and (7.3), data for the zrc1 cot1 mutant was compared to a model with the same parameters but without vacuolar transport. The model fits the zinc data reasonably well. Higher deviations in the range from $0\,\mu$M to $10\,\mu$M external zinc may be due to the fact that the zrc1 cot1 mutant has nevertheless some vacuolar storage activity by other transporters (Simm et al., 2007), which is not considered in the model. In addition, the model assumes a steady state for all external zinc concentrations, whereas the experiments might not be measured under steady state conditions. Indeed, a more recent report by Simm et al. (2007) claims that zrc1 cot1 mutants are not even viable under zinc levels of $100\,\mu$M and more. In their measurements of cell-associated zinc in wild type and zrc1 cot1 mutants (Simm et al., 2007, Fig. 1A) the difference between the two is almost insignificant between $0\,\mu$M and $25\,\mu$M and only the wild type is measured for higher values. These measurements are in very good accordance to our model predictions.

The zinc steady state measurements shown in Fig. 7.2b and time data from MacDiarmid et al. (2003) measuring internal zinc in wild type and mutant cells in a zinc shock experiment (Fig. 7.3) have been used to fit the transport rates κ_3 and κ_4 of the vacuolar transporters. From the comparison of different fits we found that these rates seem to be correlated with a ratio $\kappa_3/\kappa_4 \approx 6.5$. This means that the efflux from the vacuole via ZRT3 is stronger then the influx through ZRC1, either by a higher number of transporters or by a higher transport efficiency. The absolute values of $\kappa_{3,4}$ could not be obtained wit high certainty from the fitting, but it is clear that they need to be much greater than the transport activities of the membrane transporters. In biological terms, this means that transport into and out of the vacuole must take place on a much faster time scale than the transport on the outer membrane. This allows the vacuole to act as a buffer for rapid transient changes in the cellular zinc concentration.

As there is no data on the individual speed of gene activation, transcription, and translation, we reduced the number of the time constants γ_i by assuming average rates for each of these steps in one regulation cycle, i.e. $\gamma_{Gi} = \gamma_{Mi} = \gamma_{Ti}$. Starting with one time constant for all reactions, the parameter fit was improved by adding new time constants until no further improvement could be seen. As a result, four different time constants were needed: τ_1 was used for the regulation of ZAP1, ZRT1 and ZRT3 (γ_{GA}, γ_{MA}, γ_A, γ_{G1}, γ_{M1}, γ_{T1}, γ_{G3}, γ_{M3} and γ_{T3}), τ_2 for the regulation of ZRT2 (γ_{G2}, γ_{M2}, γ_{T2}), τ_3 for the regulation of ZRC1 (γ_{G4}, γ_{M4}, γ_{T4}), and τ_4 was used as the time constant for zinc transport (γ). It appeared to be especially important that the regulation of ZRT2 (parameter $\tau_2 \approx 0.28$) is by magnitudes slower than the regulation of ZRT1 (parameter $\tau_1 \approx 929$). As shown in Fig. 4.1, ZRT2 follows a different regulation than ZRT1 with low expression under zinc deficiency and maximal activity between 500 and 1000 μM of external zinc. In the case of zinc shock, ZRT1 seems to be downregulated in less than 5 min, while upregulation of ZRT2 and the resulting increased influx of zinc cannot be observed in the data for 20 min (cf. dotted line in Fig. 7.3). The regulation of the vacuolar import transporter ZRC1 (parameter $\tau_3 \approx 0.09$) also appears to be slow compared to ZRT1. This ensures that all excessive zinc can be transported into the vacuole.

Simm et al. (2007) present zinc shock time measurements similar to those above, which can be used to validate the model. There, in addition to the entire cellular zinc content, the concentration of zinc in the vacuole was measured separately. The measurements show that after 10 min of zinc shock $80 - 90\%$ of the inflowing zinc is directly stored into the vacuole (Simm et al., 2007, Fig. 4). This is within the tolerance in accordance with our model predictions, where after 10 min ca. 75% of the total zinc is in the vacuole (cf. Fig. 7.3 and Fig. 7.4).

Proactive expression

In the curves shown in Fig. 7.2a it seems reasonable that the vacuolar efflux transporter ZRT3 is most active under zinc deficiency in order to provide the cytosol with sufficient amounts of the essential metal, while at higher zinc concentrations it is suppressed to retain more zinc in the vacuole and protect the cytosol from excessive zinc. The regulation of the vacuolar influx transporter ZRC1, however, appears contraproductive. Very similar to ZRT3, it is also strongly upregulated under zinc deficiency, although zinc sequestration is not needed under these conditions. From the economic point of view, it

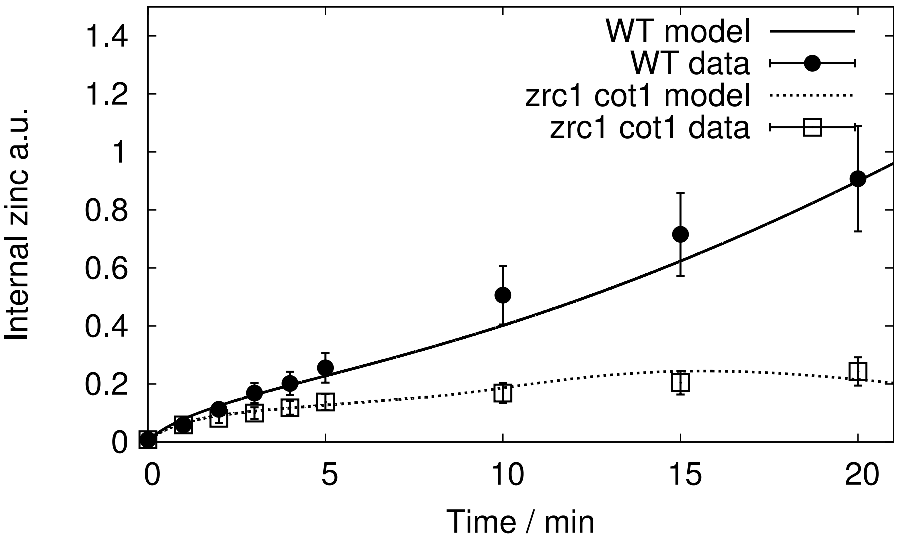

Figure 7.3: Time course of internal zinc for wild type (solid line) and zrc1 cot1 mutant (dotted line) for a resupply experiment after zinc deficiency. Data is taken from MacDiarmid et al. (2003, Fig. 6B): WT - black circles and zrc1 cot1 mutant - white squares.

seems costly and unnecessary to express ZRC1 in such high levels. MacDiarmid et al. (2003) argue that this behavior is nevertheless important for cell survival, as it appears to prevent toxicity under zinc shocks. These shocks occur when zinc deficient cells suddenly encounter moderate amounts of zinc in the medium. Due to the deficiency, their uptake transporters are upregulated to ensure maximal transport capacity. When the zinc concentration in the surrounding medium suddenly rises, these cells take up high amounts of zinc because the regulation of uptake transporters needs time to react to the new situation. Experiments show high sensitivity of zrc1 cot1 knockout mutants to zinc shocks even under external zinc concentrations that they can normally tolerate (MacDiarmid et al., 2003). These results suggest that ZRC1 plays a crucial role in the protection against zinc shocks. The most likely hypothesis presented by MacDiarmid et al. (2000) is that the upregulation of ZRC1 during zinc deficiency functions in a “proactive” manner to buffer zinc shocks by fast sequestration into the vacuole.

Our model simulations support this hypothesis, as shown in Fig. 7.4. The graph shows only the cytosolic zinc concentration during zinc shock in wild type yeast and in mutant cells without vacuolar sequestration. The zinc concentrations in both cell types eventually approach the same steady state. In

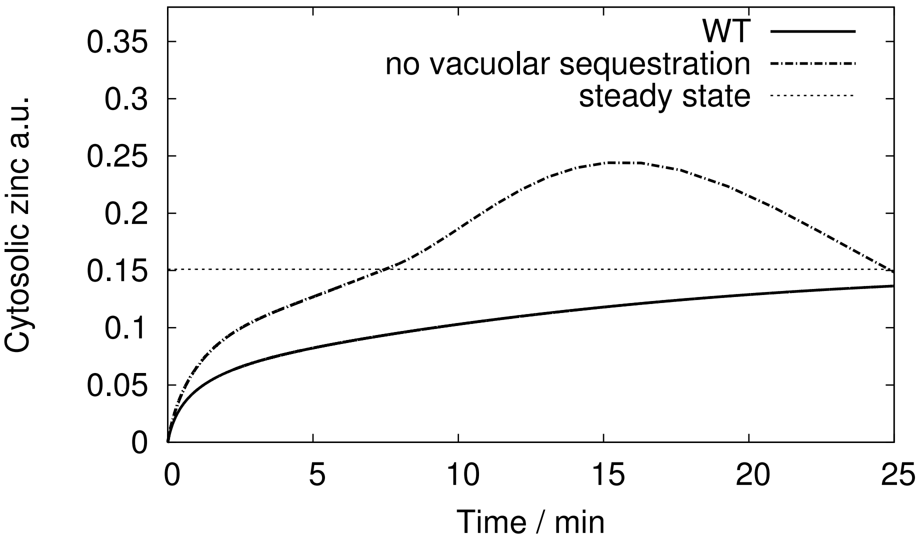

Figure 7.4: Simulation of the cytosolic zinc concentration in wild type (WT, solid line) yeast cells and mutants without vacuolar sequestration (dashed line). Both curves approach the steady state value, which is indicated by a horizontal dotted line.

the mutant cells, on the one hand, the cytosolic zinc concentration increases rapidly in the beginning of the zinc shock, which leads to an overshoot far above the steady state value. After about 15 min the concentration starts to slowly decrease towards the steady state. On the other hand, in wild type cells with ZRC1 expression, the excessive zinc is immediately stored into the vacuole. Therefore, the cytosolic concentration rises slowly and approaches the steady state without an overshoot. Assuming that yeast cells react very sensitively even to slight zinc excess in the cytosol, these curves explain the high lethality of zrc1 cot1 mutants after zinc shocks (MacDiarmid et al., 2003) and indeed suggest that ZRC1 upregulation during zinc deficiency is an efficient survival strategy of wild type yeast.

7.2 Buffering in plant roots

7.2.1 Biological background

Vacuolar sequestration in plant roots has been studied extensively during the last years but the underlying mechanisms are still not fully understood. It has been found that zinc is transported into the vacuole by different transporter proteins, namely MTPs like MTP1/3/8 and HMA3. Remobilization into the cytoplasm is accomplished by transporters of the NRAMP family.

Nicotianamine (NA) seems to play a key role in vacuolar sequestration. It is a low-molecular-weight metal chelator that is synthesized by the enzyme nicotianamine synthase (NAS). NAS has been shown to be transcriptionally regulated in response to changing zinc concentrations (Talke et al., 2006). During zinc deficiency the gene is upregulated, while transcription decreases in higher zinc levels. It is also known that zinc hyperaccumulators such as *A. halleri* have consistently higher levels of NAS and NA than non-hyperaccumulators like *A. thaliana*. Therefore it has been suggested that NA plays a role in detoxification and accumulation of zinc. Under this assumption, however, it seems surprising that NAS is downregulated at higher zinc concentrations in roots of *A. thaliana*. Besides buffering zinc by chlelation in the cytoplasm, NA seems to be involved in other processes. It enhances the transport of zinc into the xylem and shoot and the vacuolar sequestration of zinc in the root. To go into the vacuole, NA is transported by ZIF1 (Haydon and Cobbett, 2007). ZIF1 is induced by high zinc levels and seems to transport NA but not the complex of NA and zinc and no free zinc ions.

Unlike in yeast, virtually no data is available concerning the vacuolar sequestration of zinc in plants. This makes it difficult to develop a detailed realistic model and estimate its parameters. Therefore, we will confine ourselves to a simplistic model describing a very general buffering mechanism without regulation. This buffering can be accomplished both through vacuolar sequestration and by cytosolic zinc chelators.

7.2.2 Model

Buffering is modeled with a simple addition to the reduced regulatory system (5.1) as described in Chapter 5. The buffer is assumed to be present in high excess with almost constant concentration. The equilibrium constant K_b gives the steady state ratio of buffered to unbuffered zinc, i.e. $K_b = \frac{Z_b^*}{Z^*}$ and the time constant ζ_b controls the speed of the buffering reaction in relation to the other reactions (all other time constants in the model were set to 1). In terms of the differential equations, a new equation is needed to describe the dynamics of buffered zinc Z_b as

$$\frac{dZ_b}{dt} = \zeta_b(K_b Z - Z_b) \tag{7.4}$$

and the equation for the internal zinc concentration Z is extended by the corresponding term resulting in

$$\frac{dZ}{dt} = f(Z^e) - Z - \zeta_b(K_b Z - Z_b) \tag{7.5}$$

to guarantee zinc mass conservation.

7.2.3 Results and Discussion

The steady state of this extended system is equal to the steady state of system (5.1) with $Z_b^* = K_b Z$. The dynamic behavior of the system, however, can be changed dramatically. We want to analyze this change with respect to the two buffering parameters $p \in \{K_b, \zeta_b\}$.

Most informative for the dynamical behavior of the system around the steady state is the largest eigenvalue of the Jacobian matrix. The jacobian of the extended system with buffering is given by

$$J_b = \begin{pmatrix} -a & 0 & b & 0 & 0 \\ c & -1-\zeta_b K_b & 0 & 0 & \zeta_b \\ 0 & 0 & -d & -e & 0 \\ 0 & f & -g & -h & 0 \\ 0 & \zeta_b K_b & 0 & 0 & -\zeta_b \end{pmatrix} \tag{7.6}$$

where positive numbers a, b, c, d, e, f, g, h are introduced for simplification:

$$\begin{aligned} a &= KA^2 + 1 & b &= 2KA(1-G) \\ c &= f(Z^e) & d &= \Gamma I + 1 \\ e &= \Gamma A & f &= \Gamma_I(1-I) \\ g &= \Gamma' I & h &= \Gamma' A + 1 + \Gamma_I Z. \end{aligned}$$

The matrix is closely related to the Jacobian of the unbuffered system in (5.3). The characteristic polynomial $\chi(\lambda, K_b, \zeta_b)$ of J_b can be calculated as

$$\chi(\lambda, K_b, \zeta_b) = -bcef(\lambda+\zeta_b) - (a+\lambda)(-eg+(d+\lambda)(h+\lambda))(\lambda^2+\zeta_b+\lambda(1+\zeta_b+K_b\zeta_b)).$$

For an eigenvalue $\lambda(\mu, p)$ with $p \in \{K_b, \zeta_b\}$ of (7.6) it holds that $\chi(\lambda(\mu, p), p) \equiv 0$ and $\frac{d\chi}{dp} \equiv 0$. Having the solution λ^0 of $\chi(\lambda(\mu, p), p) \equiv 0$ for $p = 0$ (no buffering), we can use a continuation method with

$$\begin{gathered} \frac{\partial \lambda}{\partial p} = -\frac{\partial \chi}{\partial p} \Big/ \frac{\partial \chi}{\partial \lambda}\,, \\ \lambda(\mu, 0) = \lambda^0 \end{gathered} \tag{7.7}$$

to describe $\lambda(p)$ by a single ordinary differential equation. This equation was solved numerically at various values of Z^e using a Dormand-Prince method with adaptive step size for ordinary differential equations (Press et al., 2007).

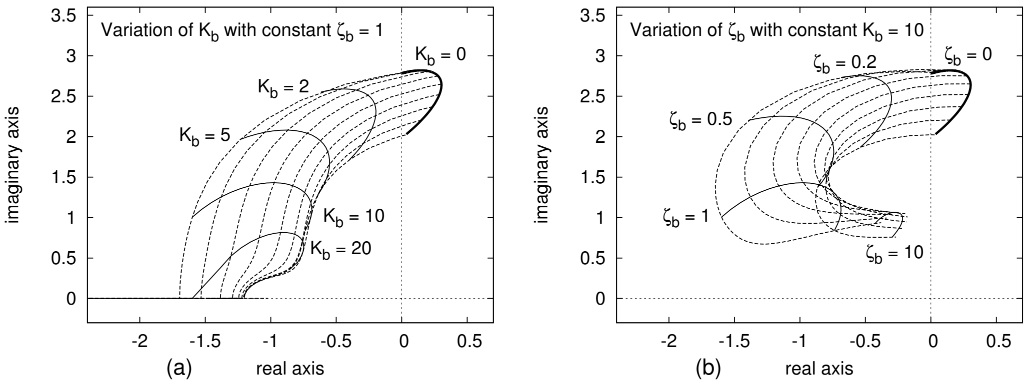

Figure 7.5: Largest eigenvalue λ_1 of the Jacobian matrix of the buffered system for variations of the two buffering parameters (a) K_b and (b) ζ_b. Dashed lines show isolines for constant external zinc concentration Z^e in the originally unstable region between $0.18\,\mu$M and $12.6\,\mu$M. Constant lines mark isolines for constant K_b (a) or ζ_b (b), respectively. Increasing either K_b (a) or ζ_b (b) stabilizes the system by decreasing real and imaginary part of the eigenvalue.

The effect of one of the buffering parameters $p \in \{K_b, \zeta_b\}$ can be calculated by choosing the other buffering parameter to be constant and solving $\chi(\lambda(\mu, p), p) \equiv 0$ via (7.7) for a given Z^e. Fig. 7.5 shows the results for both parameters and for various external zinc concentrations. The parameter K_b is related to the amount of zinc buffers in the cell and the strength of their binding affinity to zinc, ζ_b is the relative time scale of the binding and dissociation of zinc to buffer molecules. Both an increase in K_b and an increase in ζ_b decreases the real part of the first eigenvalue below zero and leads to asymptotic stability of the steady state for all external zinc concentrations. In biological terms this means that buffering needs to be sufficiently strong (high K_b) and/or sufficiently fast (high ζ_b) to stabilize the system. Equilibrium constants above $K_b \approx 1.1$ guarantee that all eigenvalues have negative real part and that the steady state is asymptotically stable. Indeed, experimental measurements suggest that most zinc in the cells is bound to chelators and buffers (Dittmer et al., 2009; Vinkenborg et al., 2009), so K_b can be estimated to be in the range of at least 1000. Under such high values of K_b all eigenvalues are real and negative and oscillations do not occur (Fig. 7.5a). The time scale ζ_b does not seem to play such an important role. The eigenvalues turn negative already at $\zeta_b \approx 0.09$ and further increase does not qualitatively change the system's behavior. Increasing ζ_b beyond 1 results even in less damping (Fig. 7.5b).

Until now, we analyzed how buffering changes the stability of the system for different values of Z^e. However, we have not dealt with the dynamic reaction to variations of Z^e, although the external zinc concentration tends to vary in time under natural soil conditions. To get an idea of how dynamic variation of Z^e affects the system, assume that the buffer reaction is such that the system stays near the steady state. Further, assume that variation in Z^e is small around a given Z_0^e. Under these conditions, the linearized system reflects the behavior of the full system sufficiently well and the concept of the transfer function of linear time invariant systems can be applied. With $U = (G, Z, A, I, Z_b)^T$ we denote with $U^0 := U^*(Z_0^e)$ the steady state U^* for $Z^e = Z_0^e$. The input is $x := (Z^e - Z_0^e)/Z_0^e$, while $y := (Z - Z_0)/Z_0$ is the output. In other words, the variation in external zinc concentration is the input and the output is given by the variation in internal zinc concentration. Note that the input and output were scaled to account for the difference in magnitude of Z and Z^e (~ 0.01 against ~ 1). The linearized system is then given by

$$\begin{aligned} \frac{d\tilde{U}}{dt} &= J_b^0\,\tilde{U} + B^0 x\ , \\ y &= C^0 \cdot \tilde{U}\ , \end{aligned} \tag{7.8}$$

where $\tilde{U} = U - U_0$, $J_b^0 = J_b(U_0, Z_0^e)$, $B^0 = Z_0^e\,\frac{\partial F}{\partial Z^e}(U_0, Z_0^e) = Z_0^e G_0 \partial_{Z^e} f(Z_0^e)\,\eta$, $\eta = (0,1,0,0,0)^T$ and $C^0 = \eta/Z_0$.

Laplace transforming (7.8) renders

$$\mathcal{L}y = C^0 \cdot \left(\left(sI - J_b^0\right)^{-1} B^0\right)\mathcal{L}x\ ,$$

where $\mathcal{L}y$ and $\mathcal{L}x$ are the Laplace transforms of y and x, respectively, and $s \in \mathbb{C}$. The function $G(s) := C^0 \cdot \left((sI - J_b^0)^{-1} B^0\right)$ is the transfer function of the system. We determined $G(s)$ numerically for $Z_0^e = 1$, $\zeta_b = 1$ and various values of K_b and present it in a Bode plot in Fig. 7.6. The details of how this graph was obtained follow. Firstly, the steady state of (5.1) extended by the equations (7.4) and (7.5) for the given Z_0^e was determined. Secondly, J_b^0, B^0 and C^0 were calculated for $\zeta_b = 1$ and various K_b. Finally, $G(s)$ was calculated using GNU Octave's *Computer-Aided Control System Design* toolbox.

Up to a resonance, the overall gain of the system is below $-20\,\mathrm{dB}$, and hence it is small (Fig. 7.6). Considering that the system is responsible for homeostasis of zinc, it makes sense that the gain is small to decouple the internal concentration as much as possible from the external concentration. A resonance at the frequency of the periodic orbits ($\omega(1\,\mu\mathrm{M}) \approx 2.92$) is clearly present for small K_b, as expected from the results on the global Hopf bifurcation in Sect. 5.5. The accumulated phases in the phase response of these unstable cases go beyond π and tend to $\frac{3}{2}\pi$ for $\omega \to \infty$. Hence, the corresponding principal values $\operatorname{Arg} G(s)$ are shown as dashed lines. Increasing K_b

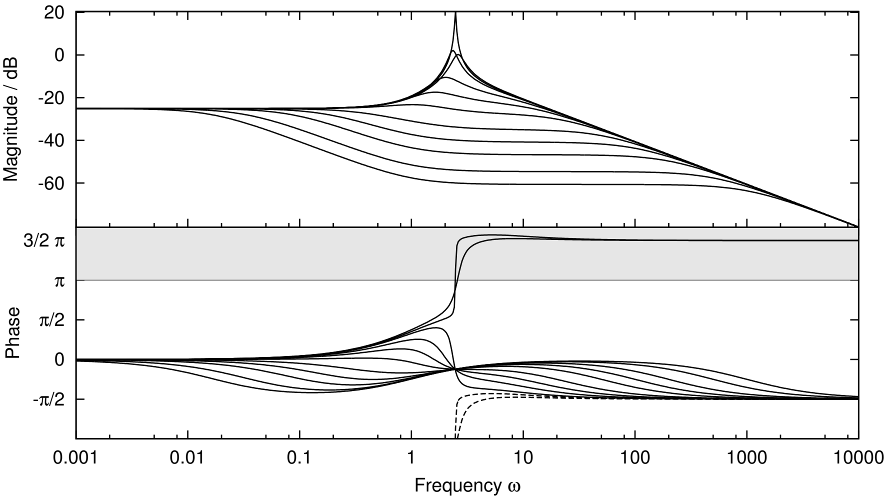

Figure 7.6: Bode plot of the transfer function $G(s)$ of the system with buffering for $Z^e = 1\,\mu\mathrm{M}$, $\zeta_b = 1$ and various K_b between 0 and 1000. For small K_b below ~ 1.1 (unstable steady state) a clear resonance appears. The accumulated phases of the unstable cases go beyond π (gray box) and the corresponding principal values $\operatorname{Arg} G(s)$ are shown as dashed lines.

damps the system until no Hopf bifurcations occur. This is seen by the sudden change in the phase response, where the argument of $G(s)$ stays smaller than π for all ω (Fig. 7.6 bottom). We found previously that high values of K_b imply overdamping of the system (Fig. 7.5a). This fact is also reflected in the phase response for large K_b: the phase for low frequencies becomes smaller than for moderate frequencies above the resonance frequency of the unbuffered system.

From a biological point of view, it is assumed to be optimal for plants to keep an almost constant zinc concentration under wide ranges of external zinc supply. In the model in Chapter 4, a high value of Γ, the binding affinity between activator and inhibitor, is required to make the steady state robust to variations in Z^e. Without buffering this high affinity, however, leads to a change in the system's dynamic behavior resulting in instability of the steady state and oscillations. Such oscillations generate toxic zinc peaks in the cells and therefore pose a dangerous threat for the plant. Without considering the important effect of buffering, we proposed in Chapter 4 that Γ should be smaller, yielding a model with less robust but stable steady states. The results of this chapter now showed that stability can also be affected by buffering without changing the steady state. We found that already weak buffering can switch the dynamic behavior of the system from oscillations to a stable steady state and thus protect the plant cells against toxic zinc shocks. Thus, our results suggest that buffering is not only important as a mechanism against fast transient supply changes, but also to stabilize the regulatory system and prevent strong self-oscillatory behavior.

8 Conclusion and Perspectives

The work presented here gives an example of how mathematical modeling can be applied to gain insights into biological systems. Zinc uptake and transport in plant roots was chosen as an example for a wide range of problems concerning transport in biological tissues. Special focus has been put on the interplay between "biological processes" like gene regulation and "physical processes" such as water flow and diffusion. The models developed here proved to be useful, since they helped to explain and analyze the zinc uptake system from a new perspective.

In Chapter 4 we proposed a very general model for the regulation of transporter proteins. This general model can be adapted and applied to zinc uptake in any organism and even more generally to any situation where solutes influence the level of their specific transporters via gene regulation and post-translational mechanisms. Here, it was used to model similar zinc uptake systems via ZIP transporters in yeast and plant roots. The system in yeast is well-understood and its behavior has been documented with extensive experimental data (e.g. Zhao and Eide, 1996b; Zhao et al., 1998; Bird et al., 2004). Still, modeling was able to provide new insights on certain aspects, especially on the important role of the ZAP1 transcriptional feedback under zinc-replete conditions. Zinc uptake regulation in plants is not as well-understood so far. Here, modeling with different possible variants derived from the general model identified a feasible mechanism. It comprises an activator and an inhibitor molecule, which provides more robust homeostasis than simpler models without an inhibitor.

In the model for zinc uptake in plant roots developed in Chapter 4 a Hopf bifurcation was found numerically for certain parameter choices. Chapter 5 is focused on the theoretical aspects of this bifurcation on a local and global scale. The analysis showed that the periodic solutions emerging from the Hopf bifurcation point are stable and that the family of periodic orbits ends in another Hopf point.

In Chapter 6 the regulatory model from Chapter 4 was coupled to a transport model describing spatial processes like advection and diffusion to model the radial movement of zinc across the plant root. This model was used to identify key processes for the creation of the radial pattern of zinc accumulation seen in experimental measurements (Hanikenne et al., 2008). Most importantly, it showed that so far the role of water flow through the root tissues has been underestimated when studying transport of solutes.

Chapter 7 focuses on another important process involved in zinc homeostasis, the buffering and sequestration of zinc by cytosolic chelators and organelles like the vacuole. Modeling the well-studied vacuolar sequestration system in yeast confirms the theory of pro-active regulation suggested by experimentalists (MacDiarmid et al., 2003). Because little detail is known on buffering in plant roots, a simple general model was used here. The results reveal that strong and fast buffering is essential in dampening transient zinc peaks and oscillations.

The methods developed here are of course not limited to the special case of zinc uptake in roots, but can also be applied to other solutes and other tissues. For example, iron is presumably taken up by a very similar system of influx and efflux transporters (Kim and Guerinot, 2007) and exhibits a similar spatial pattern (Roschzttardtz et al., 2013) in roots. Other ions, like sodium and potassium, are pumped by other transporters (Kronzucker and Britto, 2011; Shabala and Cuin, 2007) with different regulatory mechanisms, but can also be modeled in a similar framework.

The biggest drawback in the models presented here is the lack of reliable quantitative data. The parameter estimation relies on existing published experimental data and many parameters cannot be estimated at all from these few measurements. Although the results of our modeling suggest new measurements for effective validation, no attempts for the according experiments have been made so far. Therefore, the experimental validation followed by model modifications and improvements require further consideration in the future.

Bibliography

B. Alberts, A. Johnson, J. Lewis, M. Raff, K. Roberts, and P. Walter. *Molecular Biology of the Cell.* Garland Science New York, 2002.

J.C. Alexander and J.A. Yorke. Global bifurcations of periodic orbits. *Am. J. Math*, 100:263–292, 1978.

K.T. Alligood and J.A. Yorke. Families of periodic orbits: Virtual periods and global continuability. *J. Differ. Equ.*, 55:59–71, 1984.

K.T. Alligood, J. Mallet-Paret, and J.A. Yorke. An index for the global continuation of relatively isolated sets of periodic orbits. *Lect. Notes Math.*, 1007:1–21, 1983.

H. Amann. *Ordinary differential equations. An introduction to nonlinear analysis.* W. de Gruyter Berlin, 1990.

A.G.L. Assunção, E. Herrero, Y.-F. Lin, B. Huettel, S. Talukdar, C. Smaczniak, R.G.H. Immink, M. van Eldik, M. Fiers, H. Schat, and M.G.M. Aarts. *Arabidopsis thaliana* transcription factors bZIP19 and bZIP23 regulate the adaptation to zinc deficiency. *Proc. Natl. Acad. Sci. U.S.A.*, 107:10296–10301, 2010a.

A.G.L. Assunção, H. Schat, and M.G.M. Aarts. Regulation of the adaptation to zinc deficiency in plants. *Plant Signal. Behav.*, 5:1553–1555, 2010b.

P. R. Bevington and D. K. Robinson. *Data Reduction and Error Analysis for the Physical Sciences.* McGraw-Hill, 2003.

A. J. Bird, E. Blankman, D. J. Stillman, D. J. Eide, and D. R. Winge. The Zap1 transcriptional activator also acts as a repressor by binding downstream of the TATA box in ZRT2. *EMBO J.*, 23:1123–1132, 2004.

K. Birnbaum, D.E. Shasha, J.Y. Wang, J.W. Jung, G.M. Lambert, D.W. Galbraith, and P.N. Benfey. A gene expression map of the *Arabidopsis* root. *Science*, 302:1956–1960, 2003.

M.R. Broadley, P.H. White, J.P. Hammond, I. Zelko, and A. Lux. Zinc in plants. *New Phytol.*, 173:677–702, 2007.

I. Cakmak. Possible roles of zinc in protecting plant cells from damage by reactive oxygen species. *New Phytol.*, 146:185–205, 2000.

R.L. Chaney, M. Malik, Y.M. Li, S.L. Brown, E.P. Brewer, J.S. Angle, and A.J.M. Baker. Phytoremediation of soil metals. *Curr. Opin. Biotechnol.*, 8: 279–284, 1997.

A. Chavarría-Krauser and M. Ptashnyk. Homogenization approach to water transport in plant tissues with periodic microstructures. *Math. Model. Nat. Phenom.*, 8:80–111, 2013.

S.-H. Chow and J. Mallet-Paret. The Fuller index and global Hopf bifurcation. *J. Differ. Equ.*, 29:66–85, 1978.

J. Claus and A. Chavarría-Krauser. Modeling regulation of zinc uptake via ZIP transporters in yeast and plant roots. *PLoS One*, 7:e37193, 2012.

J. Claus and A. Chavarría-Krauser. Implications of a zinc uptake and transport model. *Plant Signal. Behav.*, 8:e24167, 2013.

J. Claus, A. Bohmann, and A. Chavarría-Krauser. Zinc uptake and radial transport in roots of *Arabidopsis thaliana*: a modelling apporach to understand accumulation. *Ann. Bot.*, 112:369–380, 2013.

J. Claus, M. Ptashnyk, A. Bohmann, and A. Chavarría-Krauser. Global Hopf bifurcation in the ZIP regulatory system. *submitted to J. Math. Biol.*, 2014. arXiv Preprint: 1401.5597.

S. Clemens. Molecular mechanisms of plant metal tolerance and homeostasis. *Planta*, 212:475–486, 2001.

S. Clemens, M. G. Palmgren, and U. Krämer. A long way ahead: understanding and engineering plant metal accumulation. *Trends Plant Sci.*, 7:309–315, 2002.

D. L. Cook, A. N. Gerber, and S. J. Tapscott. Modeling stochastic gene expression: Implications for haploinsufficiency. *Proc. Natl. Acad. Sci. U.S.A.*, 95:15641 – 15646, 1998.

C. D. Deppmann, R.S. Alvania, and E. J. Taparowsky. Cross-species annotation of basic leucine zipper factor interactions: Insight into the evolution of closed interaction networks. *Mol. Biol. Evol.*, 23:1480–1492, 2006.

R.J. DiDonato, L.A. Roberts, T. Sanderson, R.B. Eisley, and E.L. Walker. *Arabidopsis Yellow Stripe-Like2 (YSL2)*: a metal-regulated gene encoding a plasma membrane transporter of nicotianamine-metal complexes. *Plant J.*, 39:403–414, 2004.

P. J. Dittmer, J. G. Miranda, J. A. Gorski, and A. E. Palmer. Genetically encoded sensors to elucidate spatial distribution of cellular zinc. *J. Biol. Chem.*, 284:16289–97, 2009.

L. Dolan, K. Janmaat, V. Willemsen, P. Linstead, S. Poethig, K. Roberts, and B. Scheres. Cellular organisation of the *Arabidopsis thaliana* root. *Development*, 119:71–84, 1993.

B.S. Donahue and R.F. Abercrombie. Free diffusion coefficient of ionic calcium in cytoplasm. *Cell Calcium*, 8:437–448, 1987.

D.J. Eide. Multiple regulatory mechanisms maintain zinc homeostasis in *Saccharomyces cerevisiae.* *J. Nutr.*, 133:1532–1535, 2003.

B. Fiedler. Global Hopf bifurcation of two-parameter flows. *Arch. Ration. Mech. Anal.*, 94:59–81, 1986.

K. R. Gegenfurtner. PRAXIS: Brent's algorithm for function minimization. *Behav. Res. Meth. Ins. C.*, 24:560 – 564, 1992.

R.S. Gitan, M. Shababi, M. Kramer, and D.J. Eide. A cytosolic domain of the yeast Zrt1 zinc transporter is required for its post-translational inactivation in response to zinc and cadmium. *J. Biol. Chem.*, 278:39558–39564, 2003.

N. Grotz, T. Fox, E. Connolly, W. Park, M.L. Guerinot, and D.J. Eide. Identification of a family of zinc transporter genes from *Arabidopsis* that respond to zinc deficiency. *Proc. Natl. Acad. Sci. U.S.A.*, 95:7220–7224, 1998.

M.L. Guerinot. The ZIP family of metal transporters. *Biochim. Biophys. Acta*, 1465:190–198, 2000.

G. Hacisalihoglu, J.J. Hart, and L.V. Kochian. High- and low-affinity zinc transport systems and their possible role in zinc efficiency in bread wheat. *Plant Physiol.*, 125:456–463, 2001.

M. Hanikenne, I.N. Talke, M.J. Haydon, C. Lanz, A. Nolte, P. Motte, J. Kroymann, D. Weigel, and U. Krämer. Evolution of metal hyperaccumulation required *cis*-regulatory changes and triplication of HMA4. *Nature*, 453:391–396, 2008.

M. Haragus and G. Iooss. *Local Bifurcations, Center Manifolds, and Normal Forms in Infinite-Dimensional Dynamical Systems.* Springer London, 2011.

H.S. Harned and R.M. Hudson. The diffusion coefficient of zinc sulfate in dilute aqueous solution at 25°. *J. Am. Chem. Soc.*, 73:3781–3783, 1951.

B.D. Hassard, N.D. Kazarinoff, and Y.-H. Wan. *Theory and applications of Hopf bifurcation.* Cambrigde Univ. Pr., 1981.

M.J. Haydon and C.S. Cobbett. A novel major facilitator superfamily protein at the tonoplast influences zinc tolerance and accumulation in arabidopsis. *Plant Physiol.*, 143, 2007.

E. Hopf. Abzweigung einer periodischen Lösung von einer stationären Lösung eines Differentialsystems. *Ber. Math. Phys. Kl. Sachs. Akad. Wiss. Leipzig*, 94:1–22, 1942.

M. Ipsen, F. Hynne, and P. G. Sørensen. Systematic derivation of amplitude equations and normal forms for dynamical systems. *Chaos*, 8:834–852, 1998.

J. Ize. Bifurcation theory for Fredholm operators. *Mem. Am. Math. Soc.*, 7: 174, 1976.

M. Jakoby, B. Weisshaar, W. Dröge-Laser, J. Vicente-Carbajosa, J. Tiedemann, and F. Parcy. bZIP transcription factors in *Arabidopsis*. *Trends Plant Sci.*, 7:106–111, 2002.

I. W. Jolma, X. Y. Ni, L. Rensing, and P. Ruoff. Harmonic oscillations in homeostatic controllers: Dynamics of the p53 regulatory system. *Biophys. J.*, 98:743 – 752, 2010.

K. Katou and M. Furumoto. A mechanism of respiration-dependent water uptake in higher plants. *Protoplasma*, 130:80–82, 1986.

K. Katou and T. Taura. Mechanism of pressure-induced water flow across plant roots. *Protoplasma*, 150:124–130, 1989.

K. Katou, T. Taura, and M. Furumoto. A model for water transport in the stele of plant roots. *Protoplasma*, 140:123–132, 1987.

J. Keener and J. Sneyd. *Mathematical Physiology I: Cellular Physiology.* Springer Science+Business Media, 2009.

S.A. Kim and M.L. Guerinot. Mining iron: Iron uptake and transport in plants. *FEBS Letters*, 581:2273–2280, 2007.

E. M. Kramer, N. L. Frazer, and T. I. Baskin. Measurement of diffusion within the cell wall in living roots of *Arabidopsis thaliana*. *J. Exp. Bot.*, 58: 3005–3015, 2007.

H.J. Kronzucker and D.T. Britto. Sodium transport in plants: a critical review. *New Phytol.*, 189:54–81, 2011.

D. Leitner, S. Klepsch, M. Ptashnyk, A. Marchant, G.J.D. Kirk, A. Schnepf, and T. Roose. A dynamic model of nutrient uptake by root hairs. *New Phytol.*, 185:792–802, 2009.

K. Lust. Improved numerical Floquet multipliers. *Int. J. Bifurcat. Chaos*, 11: 2389–2410, 2001.

C.W. MacDiarmid, L.A. Gaither, and D. Eide. Zinc transporters that regulate vacuolar zinc storage in *Saccharomyces cerevisiae*. *EMBO J.*, 19:2845–2855, 2000.

C.W. MacDiarmid, M.A. Milanick, and D.J. Eide. Biochemical properties of vacuolar zinc transport systems of *Saccharomyces cerevisiae*. *J. Biol. Chem.*, 277, 2002.

C.W. MacDiarmid, M.A. Milanick, and D.J. Eide. Induction of the *ZRC1* metal tolerance gene in zinc-limited yeast confers resistance to zinc shock. *J. Biol. Chem.*, 278(17), 2003.

M.R. Macnair, V. Bert, S.B. Huitson, P. Saumitou-Laprade, and D. Petit. Zinc tolerance and hyperaccumulation are genetically independent characters. *Proc. R. Soc. Lond., B, Biol. Sci.*, 266:2175–2179, 1999.

J. Mallet-Paret and J.A. Yorke. Two types of hopf bifurcation points: sources and sinks of families of periodic orbits. *Ann. N. Y. Acad. Sci.*, 357:300–304, 1980.

J. Mallet-Paret and J.A. Yorke. Snakes: Oriented families of periodic orbits, their sources, sinks, and continuation. *J. Differ. Equ.*, 43:419–450, 1982.

W. Maret. Zinc biochemistry: From a single zinc enzyme to a key element of life. *Adv. Nutr.*, 4:82–91, 2013.

B. Marx and W. Vogt. *Dynamische Systeme: Theorie und Numerik*. Spektrum Akademischer Verlag Heidelberg, 2011.

R. Murphy. Some compartmental models of the root: steady state behavior. *J. Theor. Biol.*, 207:557–576, 2000.

X. Y. Ni, T. Drengstig, and P. Ruoff. The control of the controller: Molecular mechanisms for robust perfect adaptation and temperature compensation. *Biophys. J.*, 97:1244 – 1253, 2009.

S. Ó Lochlainn, H.C. Bowen, R.G. Fray, J.P. Hammond, G.J. King, P.J. White, N.S. Graham, and M.R. Boradley. Tandem quadruplication of HMA4 in the zinc (Zn) and cadmium (Cd) hyperaccumulator *Noccaea caerulescens*. *PLoS One*, 6(3), 2011.

E.S. Oran and J.P. Boris. *Numerical simulation of reactive flow*. Cambridge Univ Pr, second edition, 2001.

C.E. Outten and T.V. O'Halloran. Femtomolar sensitivity of metalloregulatory proteins controlling zinc homeostasis. *Science*, 292:2488–2492, 2001.

C.M. Palmer and M.L. Guerinot. Facing the challenges of Cu, Fe and Zn homeostasis in plants. *Nat. Chem. Biol.*, 5:333–340, 2009.

W.H. Press, S.A. Teukolsky, W.T. Vetterling, and B.P. Flannery. *Numerical Recipes: The art of scientific computing*. Cambridge Univ Pr, third edition, 2007.

M. Ptashnyk, T. Roose, D.L. Jones, and G.J.D. Kirk. Enhanced zinc uptake by rice through phytosiderophore secretion: a modelling study. *Plant Cell Environ.*, 34:2038–204, 2011.

K. Ranathunge, E. Steudle, and R. Lafitte. A new precipitation technique provides evidence for the permeability of casparian bands to ions in young roots of corn (*Zea mays* L.) and rice (*Oryza sativa* L.). *Plant Cell Environ.*, 28:1450–1462, 2005.

J. Robb, L. Busch, and W.E. Rauser. Zinc toxicity and xylem vessel wall alterations in white beans. *Ann. Bot.*, 46:43–50, 1980.

A.G. Roberts and K.J. Oparka. Plasmodesmata and the control of symplastic transport. *Plant Cell Environ.*, 26:103–124, 2003.

H. Roschzttardtz, G. Conéjéro, F. Divol, C. Alcon, J-L. Verdeil, C. Curie, and S. Mari. New insights into Fe localization in plant tissues. *Front. Plant Sci.*, 4:350, 2013.

HF. Rosene. Quantitative measurement of the velocity of water absorption in individual root hairs by a microtechnique. *Plant Physiol.*, 18:588–607, 1943.

H. Rutschow, T. Baskin, and E. M. Kramer. Regulation of solute flux through plasmodesmata in the root meristem. *Plant Physiol.*, 155:1817–1826, 2011.

B. Sattelmacher. The apoplast and its significance for plant mineral nutrition. *New Phytol.*, 149:167–192, 2001.

G. Schaaf, A. Schikora, J. Häberle, G. Vert, U. Ludewig, J.-F. Briat, C. Curie, and N. von Wirén. A putative function for the *Arabidopsis* Fe-phytosiderophore transporter homolog AtYSL2 in Fe and Zn homeostasis. *Plant Cell Physiol.*, 46:762–774, 2005.

K. Schütze, K. Harter, and C. Chaban. Post-translational regulation of plant bZIP factors. *Trends Plant Sci.*, 13:247–255, 2008.

S. Shabala and T.A. Cuin. Potassium transport and plant salt tolerance. *Physiol. Plantarum*, 133:651–669, 2007.

C. Simm, B. Lahner, D. Salt, A. LeFurgey, P. Ingram, B. Yandell, and D.J. Eide. *Saccharomyces cerevisiae* vacuole in zinc storage and intracellular zinc distribution. *Eukaryotic Cell*, 6:1166–1177, 2007.

S.A. Sinclair, S.M. Sherson, R. Jarvis, J. Camakaris, and C.S. Cobbett. The use of the zinc-fluorophore, Zinpyr-1, in the study of zinc homeostasis in *Arabidopsis* roots. *New Phytol.*, 174:39–45, 2007.

J. Smoller. *Shock Waves and Reaction-Diffusion Equations.* Springer-Verlag New York, 1994.

A.L. Sommer and C.B. Lipman. Evidence on the indispensable nature of zinc and boron for higher green plants. *Plant Physiol.*, 1:231–249, 1926.

E. Steudle. Water transport across roots. *Plant Soil*, 167:79–90, 1994.

E. Steudle. Water uptake by plant roots: an integration of views. *Plant Soil*, 226:45–56, 2000.

E. Steudle and J. Frensch. Water transport in plants: Role of the apoplast. *Plant Soil*, 187:67–79, 1996.

E. Steudle and C.A. Peterson. How does water get through roots? *J. Exp. Bot.*, 49:775–788, 1998.

I.N. Talke, M. Hanikenne, and U. Krämer. Zinc-dependent global transcriptional control, transcriptional deregulation, and higher gene copy number for genes in metal homeostasis of the hyperaccumulator *Arabidopsis halleri*. *Plant Physiol.*, 142:148–167, 2006.

T. Taura, Y. Iwaikawa, M. Furumoto, and K. Katou. A model for radial water transport across plant roots. *Protoplasma*, 144:170–179, 1988.

J. L. Vinkenborg, T. J. Nicolson, E. A. Bellomo, M. S. Koay, G. A. Rutter, and M. Merkx. Genetically encoded FRET sensors to monitor intracellular Zn2+ homeostasis. *Nat. Methods*, 6:737–40, 2009.

P.J. White, S.N. Whiting, A.J.M. Baker, and M.R. Broadley. Does zinc move apoplastically to the xylem in roots of *Thlaspi caerulescens*? *New Phytol.*, 153:199–211, 2002.

S. Yamasaki, K. Sakata-Sogawa, A. Hasegawa, T. Suzuki, K. Kabu, E. Sato, T. Kurosaki, S. Yamashita, M. Tokunaga, K. Nishida, and T. Hirano. Zinc is a novel intracellular second messenger. *J. Cell Biol.*, 177:637–645, 2007.

H. Q. Yang and Y. L. Jie. Uptake and transport of calcium in plants. *J. Plant Physiol. Mol. Biol.*, 31:227–234, 2005.

M. Zarebanadkouki, Y.X. Kim, A.B. Moradi, H. J. Vogel, A. Kaestner, and A. Carminati. Quantification and modeling of local root water uptake using neutron radiography and deuterated water. *Vadose Zone J.*, 11:3, 2012.

F.J. Zhao, E. Lombi, T. Breedon, and S.P. McGrath. Zinc hyperaccumulation and cellular distribution in *Arabidopsis halleri*. *Plant Cell Environ.*, 23: 507–514, 2000.

H. Zhao and D.J. Eide. The yeast ZRT1 gene encodes the zinc transporter protein of a high-affinity uptake system induced by zinc limitation. *Proc. Natl. Acad. Sci. U.S.A.*, 93:2454–2458, 1996a.

H. Zhao and D.J. Eide. The ZRT2 gene encodes the low affinity zinc transporter in *Saccharomyces cerevisiae*. *J. Biol. Chem.*, 271:23203–23210, 1996b.

H. Zhao, E. Butler, J. Rodgers, T. Spizzo, S. Duesterhoeft, and D.J. Eide. Regulation of zinc homeostasis in yeast by binding of the ZAP1 transcriptional activator to zinc-responsive promoter elements. *J. Biol. Chem.*, 273: 28713–28720, 1998.

K.C. Zygalakis, G.J.D. Kirk, D.L. Jones, M. Wissuwa, and T. Roose. A dual porosity model of nutrient uptake by root hairs. *New Phytol.*, 192:676–688, 2011.

List of own publications

Refereed

J. Claus and A. Chavarría-Krauser. Modeling regulation of zinc uptake via ZIP transporters in yeast and plant roots. *PLoS One*, 7:e37193, 2012.

J. Claus and A. Chavarría-Krauser. Implications of a zinc uptake and transport model. *Plant Signal. Behav.*, 8:e24167, 2013.

J. Claus, A. Bohmann, and A. Chavarría-Krauser. Zinc uptake and radial transport in roots of *Arabidopsis thaliana*: a modelling apporach to understand accumulation. *Ann. Bot.*, 112:369–380, 2013.

Submitted

J. Claus, M. Ptashnyk, A. Bohmann, and A. Chavarría-Krauser. Global Hopf bifurcation in the ZIP regulatory system. *submitted to J. Math. Biol.*, 2014. arXiv Preprint: 1401.5597.

Conference contributions

J. Claus and A. Chavarría-Krauser. Modeling zinc uptake via ZIP transporters. Talk at *ISRR Meeting, Dundee, Scotland*, 2012.

J. Claus, A. Bohmann and A. Chavarría-Krauser. Modeling of zinc uptake in plant roots. Talk and Poster at *HeKKSaGOn Summer School, Heidelberg*, 2012.

J. Claus and A. Chavarría-Krauser. Modeling zinc uptake and radial transport in roots. Poster at *FSPM, Saariselkä, Finland*, 2013.

J. Claus and A. Chavarría-Krauser Modeling of Zinc Uptake and Transport in Plant Roots. Invited talk at *ECMTB, Gothenburg, Sweden*, 2014